11-14-2019

Offset Electrodes for Enhanced Neural Recording in Microchannels

iian Black
Florida International University, iblac004@fiu.edu

FLORIDA INTERNATIONAL UNIVERSITY

Miami, Florida

OFFSET ELECTRODES FOR ENHANCED NEURAL RECORDING IN

MICROCHANNELS

A dissertation submitted in partial fulfillment of the

requirements for the degree of

DOCTOR OF PHILOSOPHY

in

BIOMEDICAL ENGINEERING

by

iian Black

2019

To: Dean John Volakis
        College of Engineering and Computing

This dissertation, written by iian Black, and entitled Offset Electrodes for Enhanced Neural Recording in Microchannels, having been approved in respect to style and intellectual content, is referred to you for judgment.

We have read this dissertation and recommend that it be approved.

_____
James J. Abbas

_____
Jorge Riera Diaz

_____
Wei-Chiang Lin

_____
Jacob McPherson

_____
Wensong Wu

_____
Ranu Jung, Major Professor

Date of Defense: November 14, 2019

The dissertation of iian Black is approved.

_____
Dean John Volakis
College of Engineering and Computing

_____
Andrés G. Gil
Vice President for Research and Economic Development
and Dean of the University Graduate School

Florida International University, 2019

DEDICATION

I dedicate this thesis to my wife Melissa Mueller Black, an amazing and beautiful human being, who supported me from the very beginning of this journey, nurtured our children, Liam and Susannah, and held steady through many lonely nights while I wrestled desperately with Nature in hopes that the unobserved would show its face and bring a small benefit to humankind.   I also dedicate this work to Jefferson Gomes whose kindness and generosity is difficult to measure because it flowed so freely (and I took so much) that I lost count of how many times his heart was in the room with me and his hands touched the lab bench alongside mine.

ACKNOWLEDGMENTS

have defined our world view. Without their shoulders to stand on, I would likely have

overlooked what I otherwise was able to see.

ABSTRACT OF THE DISSERTATION

OFFSET ELECTRODES FOR ENHANCED NEURAL RECORDING IN

MICROCHANNELS

by

iian Black

Florida International University, 2019

Miami, Florida

Professor Ranu Jung, Major Professor

Microchannel electrodes have emerged in recent years as promising interfaces for recording signals in peripheral nerves. Unlike many technologies, microchannels maintain stable long-term connections and can record activity in individual or small groups of axons. Unfortunately, a traditional symmetrical mid-channel electrode configuration, designed to reduce noise artifacts, prevents microchannels from being used to distinguish between signals traveling in opposite directions. This is a profound limitation given that most nerves contain a mix of efferent and afferent axons and microchannels were initially conceived and later used as the basic building block in arrays designed to record bi-directional neural traffic in regenerated nerve fibers.

Off-center, or "offset", recording sites have been predicted to record larger signals than mid-channel locations. Unlike the mid-channel configuration, offset electrode asymmetry

suggests it has the capacity to differentiate between efferent and afferent neural activity. Despite these apparent advantages, a theoretical basis for signal enhancement at offset locations has not been identified and, to our knowledge, no efforts to leverage offset electrodes for signal enhancement or discrimination in microchannels have been undertaken.

This work provides a theoretical basis to explain signal enhancement at offset electrodes. The theory is used to explore offset electrode configurations that maximize signal amplitudes and enhance differences between signals traveling in opposite directions. Neural recordings are used to validate theoretical predictions and to explore novel reference configurations that seek to minimize noise artifacts. Key shape differences between signals recorded for action potentials traveling in opposite directions are characterized and exploited to further enhance signal discrimination at offset electrodes, as well as to reduce the rate of overlapping spikes in more complex neural recording scenarios, including compound action potentials. Overall, this work introduces the offset electrode configuration as a new paradigm for recording signals in peripheral nerves and provides a foundation for the development of future devices with enhanced performance and signal discrimination capabilities.

TABLE OF CONTENTS

LIST OF TABLES

LIST OF FIGURES

LIST OF ABBREVIATIONS AND ACRONYMS

AP	action potential
SUAP	single unit action potential
CAP	compound action potential
ENG	electroneurogram
EMG	electromyogram
SNR	signal-to-noise ratio
PDMS	polydimethylsiloxane
RE	regenerative electrode
REA	regenerative electrode array
ZEVC	zero-end-voltage condition
FE	finite element
S&Pm	Stein and Pearson model
FES	functional electrical stimulation
TTL	transistor-transistor logic

CHAPTER 1

INTRODUCTION

1.1 Overview

Peripheral nerves play a central role in creating our human experience. In addition to supporting the many organ functions that sustain life, distributed networks of peripheral nerves anchor our awareness in our bodies and the environment around us. One could argue that without them, there would be no periphery, at least none that could be experienced - we would exist as insensate bodies cutoff from ourselves and a world that we could not feel or physically explore. Throughout her life, Hellen Keller relied almost exclusively on her sense of touch to gain knowledge about the world, learn to talk, read and write - skills that most individuals acquire mainly through sight and hearing, which might be considered more dominant sense modalities (Lash and Byers, 1980).

Given the power to influence human perceptions and movements, it is no wonder that many efforts have been made over the past 50 years to develop devices for interfacing with peripheral nerves. Recording devices enable one to learn the neural correlates of perception and movement and to ascertain the state or intended state of different body structures. For example, neural recordings have been used to provide an indication of bladder fullness (Chew et al., 2013) and ankle position (Haugland and Sinkjaer, 1995) and enable amputees to intuitively control motorized hand prostheses (Micera et al., 2010). Devices that stimulate peripheral nerves can elicit long-lost sensations in missing limbs to enable

amputees to feel objects using motorized upper-limb prostheses (Horch et al., 2011, Tan et al., 2014).

Ideally, devices for neural recording would be able to relay the activity of every axon in a peripheral nerve over an individual's lifespan, as this would provide a complete picture of the moment-to-moment functional state of the structures innervated by the nerve. However, most devices able to record from individual or small groups of axons do not typically remain functionally viable for more than a few months. Those that do, such as cuff electrodes, typically record aggregate neural activity and do not provide specific information about the firing state of individual or small populations of axons (Navarro et al., 2005).

Another significant design challenge for neural recording devices lies in their ability to reject unwanted non-neural signals. Muscles generate much larger electrical currents than nerves, and since nerves lie in close proximity to muscles, electromyographic signals (EMG) from muscles can overwhelm and obscure recorded neural signals. Most cuffs electrodes employ a mid-channel electrode which is referenced to a terminal created by shorting a pair of electrodes located near each end of the cuff. Known as the pseudo tripole configuration, this arrangement aims to preserve neural signals in the presence of much larger EMG artifacts (Stein et al., 1977).

Over the past decade, microchannel electrodes have emerged as promising devices for recording signals in peripheral nerves. These devices enclose small groups of axons inside narrow channels and combine chronic capability with enhanced selectivity. Like cuff electrodes, microchannel electrodes have the potential to be viable chronic neural

interfaces – the ability to maintain stable long-term connections with small populations of axons (FitzGerald et al., 2012, Chew et al., 2013, Musick et al., 2015, Srinivasan et al., 2015). Like many of the penetrating non-chronic neural interfaces, they are highly selective – able to record signals from individual axons (Dworak and Wheeler, 2009, FitzGerald et al., 2009, Delivopoulos et al., 2012, Minev et al., 2012).

Perhaps because of a shared architecture that surrounds nerve fibers, most microchannel technologies have inherited the pseudo tripole electrode configuration characteristic of their larger cuff precursors (Minev et al., 2012, Delivopoulos et al., 2012, FitzGerald et al., 2012, Musick et al., 2015, Chew et al., 2013). Unfortunately, the pseudo tripole cannot be used to distinguish between action potentials traveling in opposite directions (Sabetian et al., 2017). The mid-channel configuration severely limits the full potential of microchannel electrode technologies given their innate ability to record activity in individual axons.

Off-center, or "offset", recording sites represent an attractive alternative to the mid-channel electrode configuration for two reasons. Offset locations have been predicted to record larger signals than those at mid-channel (FitzGerald et al., 2008) and recent experimental work appears to validate this (Gribi et al., 2018). Perhaps more importantly, their asymmetry in the channel implies offset electrodes could be inherently sensitive to signal directionality and potentially be used to differentiate between signals traveling in opposite directions - permitting afferent sensory events to be distinguished separately from efferent motor commands.

1.2 Rationale

Despite these apparent advantages, to our knowledge, no efforts have been made to characterize, explore or leverage offset electrode capabilities to enhance neural signals or to differentiate between signals traveling in opposite directions. A theoretical basis to understand and predict signal enhancements at offset electrodes remains to be identified and explored. The pseudo tripole reference terminal, which is suitable for rejecting external noise artifacts at mid-channel locations, is not optimal for offset recording sites. Therefore, alternative reference configurations suitable for minimizing noise at offset electrodes remains to be explored.

1.3 Design goals

The overarching goal of this research was to design microchannels with offset electrodes and demonstrate their capacity to enhance recorded neural signals as well as discriminate between signals traveling in opposite directions. An additional goal was to explore suitable reference configurations able to reject non-neural signals at offset electrodes. To address the design goals three specific aims were identified. A theoretical framework was developed and used as a basis for the design of microchannels with offset electrodes. Microchannels with offset electrodes were fabricated and *in vitro* experimental studies were conducted on rodent nerves to validate the designs.

1.4 Specific aims

1.4.1 Specific aim 1

Specific aim 1 is to design and build microchannels with offset electrodes. This aim can be divided into the following sub-aims:

  A. Design a microchannel device capable of demonstrating signal enhancement at offset electrodes

  B. Fabricate and validate the microchannel device

1.4.2 Specific aim 2

Specific aim 2 is to develop a theoretical model to understand and predict signals at offset electrode locations and to experimentally validate this model. This aim can be divided into the following sub aims:

  A. Develop a model to predict:

      a. Neural signals at offset electrode locations

      b. Noise artifacts from:

          i. External sources

          ii. Ambient (i.e. thermal) sources

  B. Use the model to identify optimal offset locations that:

      a. Maximize amplitudes for action potentials traveling in a given direction

      b. Maximize amplitude differences between action potentials traveling in opposite directions

  C. Experimentally validate the model's ability to predict signals at offset electrodes

D. Experimentally demonstrate reference electrode configurations that reduce external noise artifacts at offset electrodes

1.4.3 Specific aim 3

Specific aim 3 is to demonstrate the extent to which offset electrodes can be used to differentiate between signals traveling in opposite directions. This aim can be divided into the following sub aims:

A. Develop a theoretical criteria to characterize recording scenarios that involve:
   a. Mostly discrete, non-overlapping single unit action potentials (SUAPs)
   b. Overlapping action potentials whose recorded signals superimpose on one another
B. Use the theoretical framework and the experimental recordings obtained in SA 2 to:
   a. Explore and validate methods that enhance signal differences at offset electrodes for discrete SUAPs traveling in opposite directions
   b. Explore the extent to which offset electrodes provide a recording advantage over mid-channel locations when recording more complex, non-discrete neural activity such as:
      i. The electroneurogram (ENG) characterized by tens or hundreds of axons asynchronously conducting signals in similar and opposite directions

ii. Compound action potentials (CAPs) characterized by all axons in

the nerve conducting signals in one direction at different speeds

1.5 Organization of the dissertation

This dissertation is divided into six chapters. Chapter 1 discusses the goals and challenges associated with neural recording, the potential benefits and rationale for using offset electrodes, the overall goals of this research and the specific aims used to achieve them. Chapter 2 describes prior efforts and technologies developed for neural recording and the intended use of microchannels. Chapter 3 describes the rationale for offset electrode placements and methods used to fabricate microchannels containing offset electrodes. Chapter 4 presents a theoretical framework for predicting signals at offset electrodes and provides experimental evidence to validate these predictions. Chapter 5 discusses methods to utilize offset electrodes to preferentially detect signals traveling in preferred directions and to discriminate between neural signals having different levels of complexity traveling in the same or opposite directions. A summary of the work, it's significance and limitations as well as future directions are presented in Chapter 6.

CHAPTER 2

LITERATURE REVIEW

2.1 Historical basis for microchannel electrodes

Neural recording devices can be divided into two categories based on the kinds of neural activity they are designed to record. Cuff and book electrodes populate the first camp. These devices are designed to fit around whole nerves and record an aggregate of all the neural activity occurring inside the nerve at any given moment. These devices proved to be chronically viable and were useful for observing non-specific neural activity in behaving animals (Stein et al., 1977, Stein et al., 1980a). In humans, they were useful in providing limited sensory feedback in closed-loop functional electrical stimulation (FES) systems (Haugland and Sinkjaer, 1995, Hoffer et al., 1996, Sinkjaer, 2000, Stein et al., 1977, Popovic et al., 1993).

The other class of neural recording devices, penetrating electrodes, are more invasive than cuffs, but also more selective. These aimed to record neural activity in individual or small populations of axons since individual action potentials are surrogate markers of function. At the most basic level, an AP's direction of travel can be used to distinguish between motor and sensory events. However, maintaining viable connections to specific axons over long periods of time proved to be a formidable challenge and many of the approaches explored over the past 50 years have yet to demonstrate chronic viability .

One of the earliest approaches involved recording from regenerated axons (Mannard et al., 1974, Edell, 1986), and sieve electrodes were developed for this purpose. Sieves were thin

8

planar disks perforated by many holes, some of which were instrumented with ring electrodes (Rosen et al., 1990, Kovacs et al., 1992, Bradley et al., 1992, Lago et al., 2007). These were designed to occupy the space between the ends of a severed nerve and interface with axons that eventually regenerated through the holes. The neural activity recorded by the fraction of holes containing electrodes was envisioned to be sufficient to provide some indication of the functional state of the targets innervated by the nerve. However, recorded neural signals could not discriminate between sensory and motor events during behavior in animal studies (Mannard et al., 1974). Also, while some recording sites successfully transduced neural activity, many sites failed to record signals even in cases where axonal regeneration had occurred and electrodes were functional (Lago et al., 2005). Lack of signals was speculated to be due to misalignment between electrodes and the nodes of Ranvier in captured myelinated axons, where action currents are concentrated and extracellular signals are largest.

Microchannel arrays were conceived to address this limitation with sieves (Loeb et al., 1977). Originally termed "tubular" electrodes, these were essentially extruded sieves, with the holes having been transformed into an array of many channels, through which axons would regenerate. Confining the space around axons increases the extracellular resistance and therefore the extracellular potential produced by action currents. Extracellular potentials inside the channel were mathematically shown to be largely independent of nodal position relative to an electrode situated at mid-channel (Marks and Loeb, 1976). As long as channel lengths exceeded internodal distances, the action currents of at least one node were guaranteed to lie somewhere within the channel and a misaligned electrode

would still be able to record a neural signal. While tubular electrode arrays were fabricated, axons failed to regenerate through the tubes and the microchannel concept was not experimentally validated (Loeb et al., 1977). The popularity of cuff electrodes and the emphasis on sieve development dominated research efforts and the microchannel concept remained unexplored and dormant for about 30 years.

In 2008, a group out of Cambridge, England revisited the tubular electrode concept, redubbing them "microchannels" (FitzGerald et al., 2008) As before, microchannels were envisioned as the basic building block for constructing RE arrays. Their ability to enhance neural signals despite misalignment between recording sites and nodes of Ranvier of active fibers in the channel were again identified as their hallmark features. The Cambridge group theoretically and experimentally explored signal enhancement in microchannels (FitzGerald et al., 2008, FitzGerald et al., 2009), characterized the ability of axons to regenerate through channels of different dimensions and lengths (Lacour et al., 2009), and developed planar arrays of microchannels and incorporated them into a closed-loop FES system for improved bladder control (Chew et al., 2013). The group also developed microchannel-based RE arrays that successfully recorded neural activity in regenerated motor and sensory sciatic nerve axons in rats (FitzGerald et al., 2012). This laid the groundwork for other researchers to develop chronically viable microchannel-based RE arrays (Srinivasan et al., 2015) capable of recording activity in many axons innervating the hindlimb structures of rats during treadmill locomotion (Musick et al., 2015).

2.2 Microchannel capabilities not fully realized

Despite these successes, microchannel technology is impaired by a symmetric electrode configuration that prevents them from discriminating between motor and sensory traffic. This is a profound limitation given that many peripheral nerves contain a mix of motor and sensory fibers and an inability to distinguish between them dramatically increases the computational burden for spike sorting algorithms used to classify recorded neural signals (Lewicki, 1998).

The basis for this limitation, however, is understandable. Although RE arrays and cuffs fall on opposite ends of the invasiveness spectrum (Navarro et al., 2005), they nevertheless share a common architecture that is probably responsible for their success as chronic implants, namely, they both surround bundles of nerve fibers. Cuff recordings were susceptible to large electromyographic (EMG) voltage artifacts arising from muscles contracting in the vicinity of their host nerve. Because these often obscured the much smaller neural signals, an electrode configuration known as the pseudo tripole was developed to reduce these comparatively large EMG artifacts (Stein et al., 1975). The pseudo tripole configuration is characterized by a recording electrode located at mid-channel and two reference electrodes close to the ends of the channel that are shorted together to create a single reference terminal. Neural signals are recorded as the difference between the mid-channel electrode and the shorted pseudo tripole reference, which averages external artifacts occurring near the ends of the channel (Struijk et al., 1999). Since differences in voltage at the ends of the channel are presumably distributed linearly inside the channel, the mid-channel location also records an average of the external artifacts

seen at the channel ends. Thus, both the mid-channel electrode and the reference terminal record equivalent external noise artifact signals that ideally cancel each other out in the difference. Neural signals are much more prominent at mid-channel compared to the locations near the ends and, therefore, do not cancel out.

While the configuration does help to reduce external artifacts, because of its bilateral symmetry, an action potential traveling to the right produces an identical signal as one having a similar speed traveling to the left (Sabetian et al., 2017). Thus, the pseudo tripole enhances noise rejection at the expense of signal discrimination, a tradeoff that is warranted for cuffs that, by design, are typically unable to resolve signals at the level of individual axons. For microchannels, this tradeoff represents a devastating compromise, which severely limits their capabilities and prevents their full potential from being realized. Nevertheless, nearly all microchannel technologies employ pseudo tripole electrode configurations. This includes all the RE arrays developed to date (Musick et al., 2015, FitzGerald et al., 2012, Srinivasan et al., 2015) as well as microchannels containing multiple electrodes (Minev et al., 2012) and planar arrays consisting of multiple channels (Chew et al., 2013).

2.3 Offset electrodes potentially enhance microchannel capabilities

A finite element model developed by FitzGerald and colleagues to explore extracellular potentials inside microchannels noted that signals were maximized near one end of the channel rather than at mid-channel (FitzGerald et al., 2008). Figure 2.1 replicates Figure 9a in their study with red text and markings added for illustration. For a right-bound action potential traveling in the myelinated fiber, maximum signals (i.e. negative peak

12

amplitudes) are expected to occur about 2.3 mm to the right of mid-channel. Mid-channel amplitudes are about 80% of the maximum and to the left of mid-channel, signals are progressively attenuated. Signal amplitudes rapidly decline for recording sites approaching the channel exit.

Figure 2.1 Peak signal amplitudes at different longitudinal positions (from FitzGerald et al 2008). The maximum signal amplitudes for right-bound action potentials traveling in a small unmyelinated and much larger myelinated fiber. For the 10 µm myelinated fiber, the maximum signal occurs at a location to the right of mid-channel. Mid-channel (vertical dashed line) and the location where signals are maximum are highlighted in red. Bold vertical lines on the left and right side of the figure indicate the channel entrance and exit, respectively.

In general, the analysis suggests that recording sites offset from mid-channel in the direction of AP propagation are expected to record the largest signals. Furthermore, a similar action potential traveling to the left would be expected to produce the largest signals at a location 2.3 mm to the left of mid-channel. Therefore, compared to mid-channel locations, offset electrodes appear to be superior in two key respects: 1) they record larger signals and 2) they can be used to preferentially detect APs traveling in a specific direction.

2.4 Reference configurations for offset electrodes

Given the potential for offset electrodes to enhance signal detection and discrimination in microchannels, alternative reference configurations are required, since the pseudo tripole reference terminal is suitable only for canceling artifacts at mid-channel electrodes. Interestingly, alternative references have been explored for mid-channel electrodes in cuffs. One approach demonstrated that a single external electrode aligned to the same axial position as the one in the channel was shown to reject stimulus artifacts and external EMG as well as the traditional pseudo tripole configuration (Thomsen et al., 1996). Figure 2.2 A shows longitudinal and transverse views of their approach (with additional notation provided). Here a pseudo-tripolar reference, created by the contacts at "a" is compared to a single external electrode at "c" that is aligned with but resides outside the tube containing the recording electrode at "b". The cross section shows that electrode "c" rests in its own channel parallel to the inner one while also being isolated from the body environment.

A similar approach could be employed to achieve noise cancellation at offset electrodes. For example, Figure 2.2 B shows a two-channel configuration, where a channel containing the nerve lies parallel to an empty reference channel. Since both electrodes have the same axial alignment inside their respective channels, the signals recorded due to external noise are expected to be nearly equivalent.

A

B

recording electrode

nerve

empty channel

reference electrode

recording electrode "b"

empty compartment

reference electrode "c"

+   -

Figure 2.2 One strategy to reject noise at offset electrodes. In A), a single external reference electrode "c" situated in its own compartment and axially aligned with the recording electrode "b" had equivalent noise-rejection capabilities as traditional pseudo-tripolar configurations ("b" and the two "a" electrodes connected). B) Approach to reject noise in an offset configuration.

CHAPTER 3

DESIGN AND HAND FABRICATION OF MICROCHANNELS WITH OFFSET

ELECTRODES

3.1 Introduction

Microchannels have emerged as promising technologies for neural recording in recent decades because of their ability to record activity in individual axons and potential for use as implantable neural interface devices. They were originally conceived as key building blocks for regeneration electrode arrays (REAs) (Loeb et al., 1977), an extension of sieve electrodes, where severed axons were encouraged to regenerate through an array of small holes penetrating a thin plate (i.e. the "sieve"). Electrodes surrounding a few of the holes recorded neural activity at different locations over the nerve's cross section (Rosen et al., 1990, Kovacs et al., 1992), with the activity of individual axons being recognizable. Unfortunately, many axons failed to grow through the sieve and those that did were often surrounded by connective tissue layers that walled them off from the electrodes and prevented their activity from being recorded. In addition, because sieve thicknesses ranged between 100-250 µm, they were typically thinner than the intranodal distances of regenerating axons (~ 300 µm) and neural activity would only be recorded from axons whose nodes of Ranvier lined up with the electrode. This was speculated to be the reason for why many sites failed to record neural activity in holes where axonal regeneration had been successful (Lago et al., 2007, Ramachandran et al., 2006).

REAs were essentially extruded sieves, so that the wafer-thin holes in sieves were transformed into long thin microchannels. These were able to record neural activity even when nodes of Ranvier of active neurons did not line up with electrodes inside each channel. REAs were envisioned as transformative technologies that could enable chronic recording from many sensory and motor axons in the nerve's cross section. It is somewhat ironic, therefore, that REAs employed mid-channel electrode configurations incapable of differentiating motor signals from sensory ones, a profound limitation given their intended use.

Neural recording theory predicts non-central, or "offset", electrodes would enhance signals and enable action potentials traveling in one direction to be detected separately from those traveling in the opposite direction. Offset electrodes can also be used to stimulate and elicit action potentials that travel in a desired direction (FitzGerald et al., 2009). Therefore, offset electrodes have the potential to significantly improve the usefulness of future REA devices for selective bidirectional interfacing with nerves.

A finite element model predicted signal enhancements at an offset electrode (FitzGerald et al., 2008) and recent experimental work appears to support this (Gribi et al., 2018). However, these studies do not provide any rational basis to explain this phenomenon nor has any work been done, to our knowledge, to harness offset electrodes to enhance signals and signal discrimination in microchannels.

This work describes the design and fabrication of microchannels containing offset electrodes. A theory previously developed (Stein and Pearson, 1971, Marks and Loeb, 1976) for neural recording in channels is used to intuit optimal recording sites and provide

17

a rational basis for why signals are expected to be largest at locations offset from mid-channel. Action potential waveform shapes reported in the literature are combined with theoretical predictions to justify electrode placements in fabricated microchannels. Preliminary efforts to record neural activity in microchannels is used to guide channel diameters. We provide details for making microchannels, characterize their electrical properties and demonstrate their capacity to record neural signals.

3.2 Methods

3.2.1 Intuiting optimal offset locations using neural recording theory

The transmembrane currents that characterize action potentials spread out along the axon over finite distances equal to the product of the time it takes them to dissipate (i.e. duration) and the speed at which they propagate (i.e. velocity). These generate equal and opposite intra- and extracellular currents that flow mainly parallel to the axon and produce intra- and extracellular voltages proportional to the resistance they encounter in- and outside the axon (Meier et al., 1998a). Because resistance is proportional to cross-sectional area, extracellular voltages are typically many orders of magnitude smaller than intraaxonal ones due to the large size differential between an axon's cross sectional area and the area of the surrounding extracellular environment (Hodgkin and Rushton, 1946) Microchannels confine the space around axons which increases the extracellular resistance and voltages that can be recorded. Any action currents lying outside the channel, such as beyond its ends, are shunted by the large extracellular volume and therefore cannot contribute to the extracellular signal. Mathematically, signal loss at the channel ends is characterized by what Stein and Pearson referred to in their theory as the "2nd Difference" term (Stein and

<u>Pearson, 1971</u>) and which we call simply the "difference" term. Extracellular voltages inside the channel are proportional to the difference term, given below as:

$$\text{"difference"} = \frac{v_m(L) - v_m(0)}{L}x + v_m(0) - v_m(x)$$

where "x" is the distance of an electrode from the left end of the channel (at x=0), "L" is the channel length, $v_m(x)$ is the amplitude of the transmembrane voltage at the electrode, and $v_m(0)$ and $v_m(L)$ are the transmembrane amplitudes at the left and right ends of the channel, respectively. The difference term is expressed in words as: "*the magnitude of the signal at any longitudinal location inside the channel is equal to the transmembrane voltage at that location minus a linear interpolation of the transmembrane voltages at the ends of the channel.*" When transmembrane voltages at the ends of the channel are zero, a scenario that we call the "zero-end-voltage condition", or ZEVC, the above statement simplifies to: "*the magnitude of the signal at any location inside the channel is equal to the transmembrane voltage at that location.*" The ZEVC is satisfied whenever channels are at least as long as the AP wavelength and peak extracellular signals then coincide with the location of the AP peak inside the channel.

For illustrating relationships between AP spatial profiles, channel length and optimal electrode placements, it is useful to represent APs using triangular waveforms, as shown in Figure 3.1. These are characterized by a steep rising phase and a shallower falling phase that converge to pointed peaks where the AP is maximum. Triangular approximations have been used before to accurately reconstruct experimentally recorded compound action

potentials (<u>Gasser and Erlanger, 1927</u>) and to model extracellular fields generated by individual action potentials (<u>Plonsey and Barr, 2007</u>).

3.2.1.1 Offset electrodes are always optimal when AP wavelength and channel length are equal

The minimum channel length that satisfies the ZEVC is when it equals the AP wavelength. In this case, there will be one instant when the spatial profile of the AP completely fits inside the channel. Because APs are skewed waveforms with their peaks closer to their leading edges, the peak extracellular signal will always occur at offset locations to the right or left of mid-channel, depending on the APs direction of travel. Their rising phase length determines the distance from the end of the channel where the largest signal is expected to occur (Figure 3.1 A, ii).
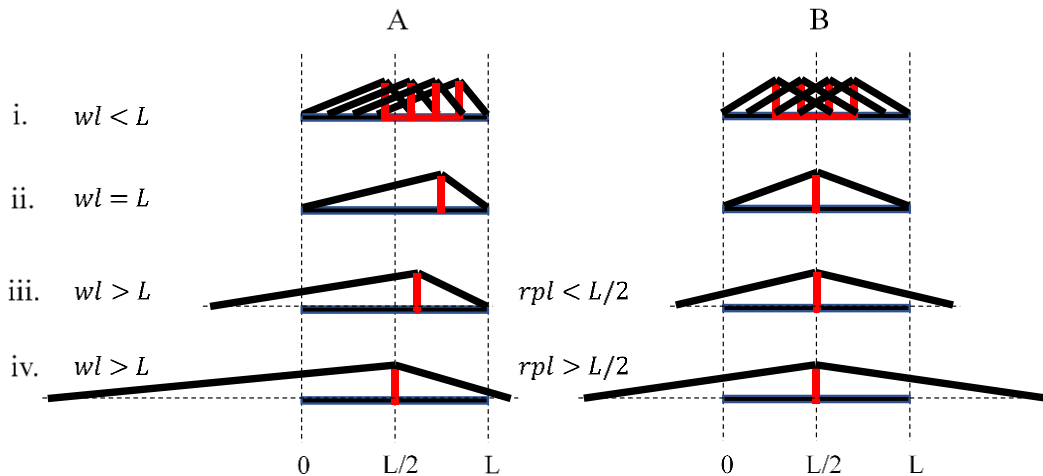
Figure 3.1 Predicted optimal electrode placements. Optimal locations for A) asymmetrical and B) symmetrical triangular AP waveforms. Four scenarios are considered: i) wavelength is less than channel length, ii) wavelength and channel length are equal, iii) wavelength is greater than channel length with rising phase length less than half the channel length and iv) wavelength is greater than channel length with rising phase length greater than half the channel length. Red vertical lines denote optimal electrode

locations where signal amplitudes are predicted to be greatest. Symbols are: *wl* = wavelength, *rpl* = rising phase length, *L* = channel length.

3.2.1.2 Multiple locations are optimal when AP wavelengths are shorter than the channel

When AP wavelengths are shorter than the channel, the ZEVC is satisfied over a range of positions starting at one rising phase length from the end of the channel, as above, and extending inwards towards mid-channel a distance equal to the difference between the channel length and AP wavelength. If wavelengths are much shorter than the channel (i.e. falling phase lengths are less than or equal to half the channel length) the range of positions where maximum signal occurs will include the mid-channel position. In (i) of Figure 3.1, the falling phase length of the AP is less than half the channel length and the range of channel positions where signals are maximum includes mid-channel. Nevertheless, the range is not symmetrical about center. Rather it is skewed to the right, in the AP's direction of travel.

3.2.1.3 Offset electrodes are optimal when AP wavelengths are longer than the channel except when rising phase lengths exceed half the channel length

When AP wavelengths are longer than the channel the ZEVC will never be satisfied. In this case, signals are maximized when voltages at the rising phase end of the channel (i.e. at x=L) are kept as small as possible since the leading edge of the AP increases at a faster rate than the trailing edge and contributes more substantially to the interpolated value between the channel ends. Up to a distance of half the channel length, the optimal electrode position is then still equal to a distance of one rising phase length from the end of the channel, since its end-voltage will remain zero and the end voltage of the trailing edge will be as small as possible (Figure 3.1 A, iii). When rising phase lengths of triangular APs

exceed half the channel length, it can be shown mathematically that maximum signals always occur at mid-channel (Figure 3.1 A, iv). However, offset locations may still be optimal for realistic APs with curvilinear, instead of triangular, profiles.

3.2.1.4 Action potential asymmetry underscores signal enhancement at offset electrodes

If APs were symmetrical about their midpoints then their rising and falling phases would have equal lengths. In this case, scenarios (ii-iv) in Figure 3.1 A would place the optimal electrode position at mid-channel and, for scenario (i), a range of channel positions centered about mid-channel would be expected to have the largest signal. Thus, if APs were symmetrical waveforms, the optimal electrode position would always occur at mid-channel or in a region centered about mid-channel. It is only because APs are asymmetrical waveforms that offset electrode positions are ever optimal.

3.2.1.5 Recording scenarios where offset electrodes are projected to provide signal enhancement

The above analysis using triangular waveforms suggests that electrodes offset from the mid-channel are expected to record the largest signals when half the channel length is greater than the length of the rising phase and shorter than the falling phase. A distance of a rising phase length from the channel end nearest the leading edge of the action potential is expected to record the largest signal for a range of APs satisfying these conditions.

Figure 3.2 shows the range of conduction velocities and channel lengths for which offset electrodes are expected to record the largest signals. Channel lengths reflect those typically found in the literature for microchannels (6 - 10 mm) and cuff electrodes (16 - 30 mm). As

shown, offset electrodes would apply over a wide range of channel lengths and conduction velocities. For channels longer than 20 mm, offset electrodes are expected to record the largest signals for action potentials having speeds equal to (and beyond) the upper physiological limit of 120 m/s (vertical dotted line).
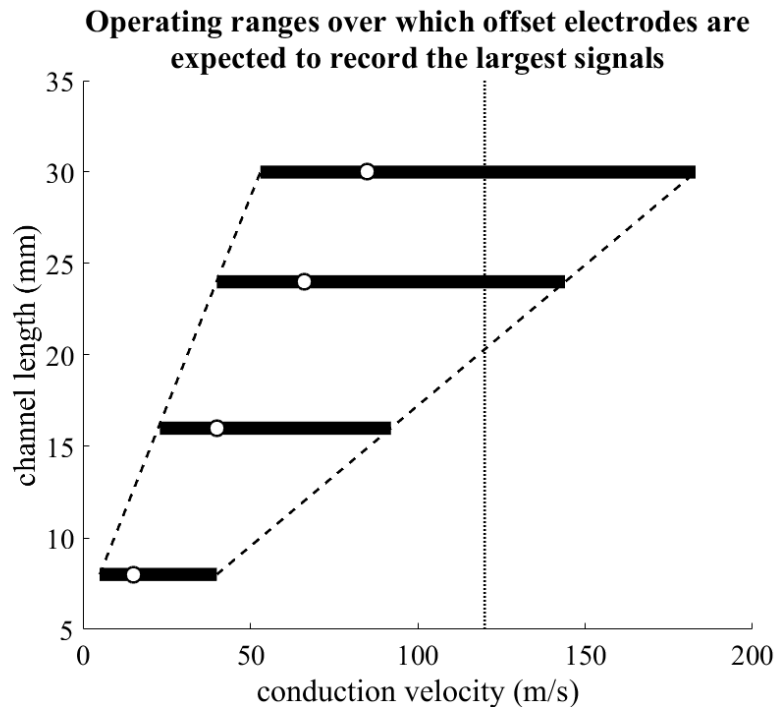
Figure 3.2 Channel lengths and conduction velocities over which offset electrodes are expected to record the largest signals. Channel lengths are 8, 16, 24, and 30 mm. White circles (O) at 15, 40, 66 and 85 m/s denote APs with a wavelength equal to channel length. Dashed lines (---) enclose a region of operation for offset electrodes and the vertical dotted line (…) at 120 m/s represents the upper limit of physiological conduction velocity.

3.2.2 Design specifications

3.2.2.1 Channel length

As mentioned previously, AP wavelengths must fit entirely within the channel for signal amplitudes to be maximized (Stein and Pearson, 1971). The relationship between AP durations and their speeds have been carefully documented (Paintal, 1966) and one can

23

estimate their wavelengths by taking their product. Typically, the faster these currents travel, the more space they occupy along the axons, however, for action potentials having speeds of between 6-12 m/s, wavelengths remain nearly constant at about 8 mm (Paintal, 1967). Preliminary neural recordings we obtained in rat dorsal rootlets showed many action potentials to have speeds within or close to this range. Therefore, a channel length of 8 mm was selected as this was the minimum channel length expected to accommodate the wavelengths of the majority of recorded action potentials. Longer channels would have sufficed except signals were expected to peak over a range of channel positions that would include sites closer to mid-channel, as discussed previously.

3.2.2.2 Electrode positions

Action potentials are inherently asymmetric waveforms and peak at a distance of about ¼ of their wavelength from the leading edge, also known as the rising phase length. Neural recording theory predicts that peak signals coincide with action potential peaks (Stein and Pearson, 1971, Marks and Loeb, 1976). When action potentials fit exactly inside the channel, which occurs when their wavelengths and channel lengths are equal, their peaks are located at offset locations, equal to a distance of one rising phase from the end of the channel closest to the peak, where theory predicts the largest signals. In general, if action potentials are assumed to be triangular waveforms, their rising phase lengths determine optimal electrode locations. It can be shown that peak signals will always occur a distance of one rising phase length from the channel end closest to the action potential peak (up until rising phase lengths equal or exceed half the channel length at which point the largest signals are expected to occur at mid-channel). A finite element model by FitzGerald and

24

colleagues supports this prediction without providing any rationale as to its underlying cause. Their model predicted the largest signals in a 10 mm long microchannel to occur at a location 2.7 mm from the right end of the channel, a distance equal to the rising phase length of their simulated right-bound action potential (FitzGerald et al., 2008).

For speeds of between 6-12 m/s, Paintal showed action potentials peak at approximately 2 mm from their leading edge. Electrodes situated 2 mm from the ends of an 8 mm channel were, therefore, expected to record the largest signals for APs traveling in either direction. Thus, we designed channels with optimal offset electrodes situated 2 mm in from both ends of the channel. An electrode at 4 mm was selected to enable signals at mid-channel to be compared to those recorded at optimal offset locations. Electrodes situated 1 mm in from both ends of the channel were included as well. These served as an additional pair of offset electrodes and provided the option to create pseudo or true tripole references for the inner electrodes, if desired. Thus, channels contained 5 electrodes located at 1, 2, 4, 6 and 7 mm (measured from either end) with those located at 4 and 2 mm expected to record the largest signals for right- and left-bound action potentials, respectively.

3.2.2.3 Electrode material

In preliminary experiments, we used stainless steel electrodes (50 µm O.D. bare, A-M Systems, WA) to successfully record neural signals in microchannels having inner diameters of 310 µm. However, we found it difficult to control their exposure lengths inside the channel, which made it difficult to standardize and control their impedance values since these electrodes extended straight across the lower portion of the channel's cross-section. FitzGerald and colleagues described a technique in which gold wire was

25

repeatedly wrapped around an inner core, that was removed once the PDMS substrate around it had cured (FitzGerald et al., 2009). We employed a similar, but modified approach using silver, which could easily be bent and formed and which we found had lower impedance than stainless steel after the silver was soaked in bleach to create an Ag/AgCl chlorinated surface. Therefore, silver wire (75 µm O.D. bare, A-M Systems, WA) was selected for making electrodes as this material had good impedance and workability characteristics that afforded opportunities to standardize exposure areas and, therefore, electrode impedance values.

3.2.2.4 Channel diameter

The selection of channel diameter was based on prior work. Previously, we recorded signals in teased rat dorsal rootlets using microchannels having inner diameters of 310 µm. For action potentials traveling between 7-20 m/s, peak signal amplitudes ranged between 7-25 µV with a background noise band of about +/- 5 µV peak-to-peak and a minimum signal-to-noise ratio (SNR) of about 1.4. FitzGerald and colleagues recorded from teased rat L5 ventral rootlets using microchannels having diameters of 130 µm and obtained peak signal amplitudes of between 10-60 µV with a similar noise band for action potentials traveling between 6-22 m/s (FitzGerald et al., 2009). Minimum SNR for their data was about 2. Minimum SNR of between 1.4-2 were considered acceptable. Therefore, channels were designed with an inner diameter of 200 µm, slightly less than midway between 130 and 310 µm.

3.2.3 Fabrication

3.2.3.1 Microchannels

Polydimethylsiloxane (PDSM) microchannels were made by mixing 5 g of PDMS (Sylgard 184, Dow-Corning, MI) using a 10:1 (Part A : Part B) mixture that had been degassed for about an hour in a desiccator (Scienceware, NJ) to remove air bubbles. Approximately 1 g of PDMS was poured around a 200 μm diameter silver wire (A-M Systems) suspended ~500 μm above the surface of a glass slide held taught by a pair of copper alligator clips glued to the slide (Figure 3.3 A). The assembly was placed on a hot plate with a surface temperature of about 250 °C which produced a cured pool of PDMS in about 1-2 minutes with dimensions of approximately 1 mm in height and 10 mm x 15-20 mm in width and length (Figure 3.3 B). A pair of pliers was used to gently extract the wire and a razor was used to trim the ends of the PDMS block to produce a 200 μm I.D. x 8 mm hollow long channel (Figure 3.3 C, D). The block was also trimmed parallel to the channel about 1 mm to one side of it.

3.2.3.2 Electrodes

Ag/AgCl electrodes were prepared by using a pair of fine forceps to remove about 4-5 mm of insulation from the end of a coated silver wire having a bare silver core diameter of 50 μm and an outer diameter of 100 μm (Figure 3.3 F). The bare wire tips were left in chlorine bleach (Clorox) for about half an hour until their color had turned from shiny silver to a dull gray, indicating that chlorination had occurred.
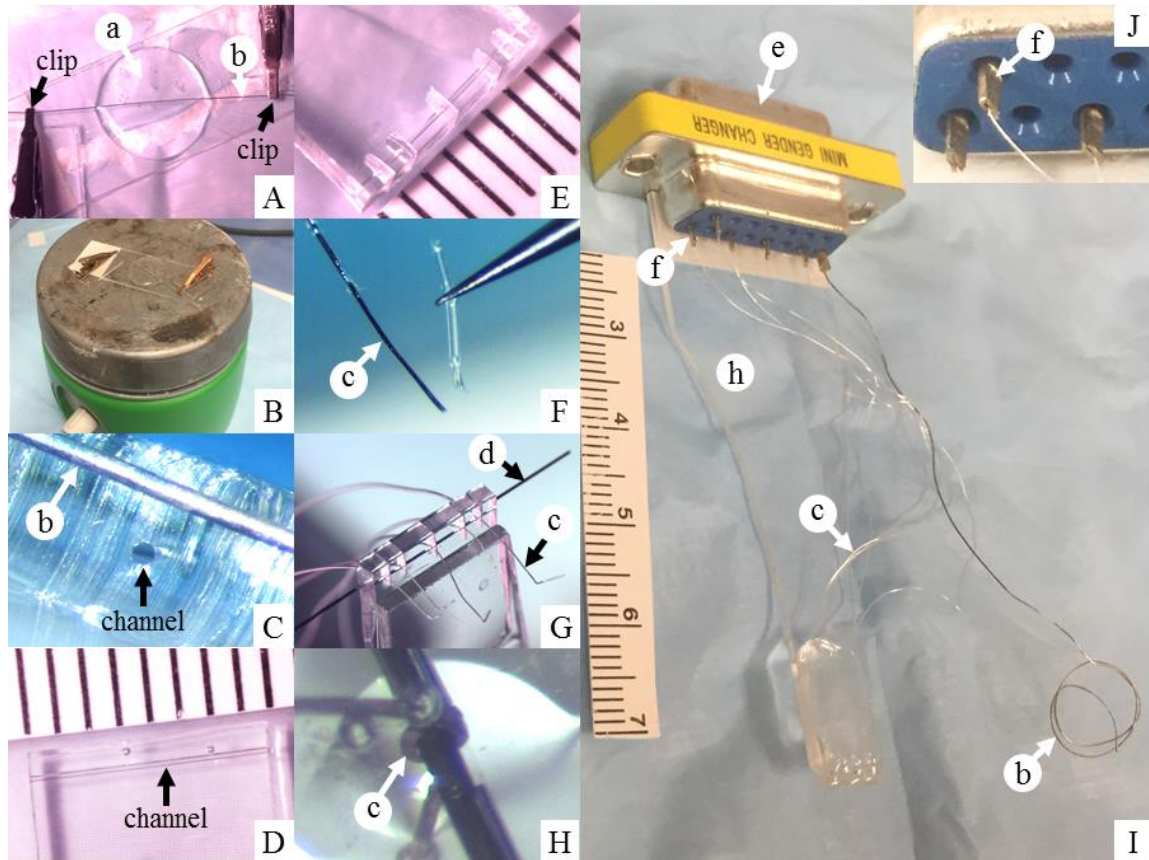
Figure 3.3 Microchannel fabrication. Lower-case letters refer to items listed in Table 3.1. A) PDMS is poured around a 200 μm Ag wire suspended above the surface of a glass slide by alligator clips and B) cured on a hot plate for about a minute. C) Removal of the wire produced a hollow circular channel with an inner diameter equal to the wire and D) a length of 8 mm after trimming the edges with a razor. E) Electrode sites were prepared by cutting slits perpendicular to the channel and F) electrode wires were prepared by removing 8-10 mm of insulation from both ends and soaking one end (the recording site) in bleach for about ½ hour to chlorinate their surfaces. G) Electrode wires were eased (using a flossing motion) into the bottom of each slit and H) wrapped around a smaller steel guide wire that had been inserted into the channel. I) The slits were sealed with PDMS, cured over the hotplate and the channel/electrode assembly was attached to the end of a glass slide that had been glued to a DB-15 female/female adapter. J) Gold-plated DB pins were crimped to the de-insulated ends of each electrode lead and inserted into appropriate ports in the DB-15 adapter. A coil of bare 200 μm Ag wire was also fitted with a DB pin and plugged into the adapter to serve as a reference terminal for all the electrodes (labeled "b" in I).

Electrode sites were prepared by making five short slits in the PDMS block perpendicular

to the channel's long axis and at longitudinal positions of 1, 2, 4, 6 and 7 mm (Figure 3.3

28

E). The slits were about 1.2 mm long and cut completely through the depth of the block and the edge 1 mm from the channel. The PDMS block was lifted and repositioned on the slide so that the channel and slits protruded about 2 mm beyond the short edge of the slide. Using a flossing motion, the bare Ag/AgCl tips made earlier were slid into each of the slits until the wire touched the inner edge of the slit as far as possible from the 1 mm cut edge and out of the path of the channel. A 150 μm OD steel guide wire was temporarily inserted through the channel and the bare portion of each silver electrode was wrapped tightly around the inner guide wire using a single turn. The electrode wires were trimmed even with the PDMS surface and then coated with PDMS and cured on the hot plate as before, a process that was repeated until no part of any electrode wire was exposed (Figure 3.3 G, H). The slits maintained the axial position of each electrode and enable them to be placed with high precision. Also, the inner walls of each slit pressing against the wrapped wires created a seal that prevented any PDMS from entering the channel or coating the inner surfaces of the electrode wires facing towards the center of the channel.   The steel guide wire was gently removed and the PDMS block was glued to the glass slide using a thin layer of PDMS which was then cured. Completed channels were 200 μm I.D. x 8 mm long and contained five Ag/AgCl circular electrodes with inner diameters of 150 μm precisely positioned at 1, 2, 4, 6, and 7 mm.

3.2.3.3 External connections and reference

Gold-coated DB-9 pins were crimped to the other end of each electrode wire that had had about 10-15 mm of insulation removed (Figure 3.3 J). These were inserted into a DB-15

female/female adapter which had been glued with super glue to the end of the glass slide

opposite to the microchannel (Figure 3.3 I).
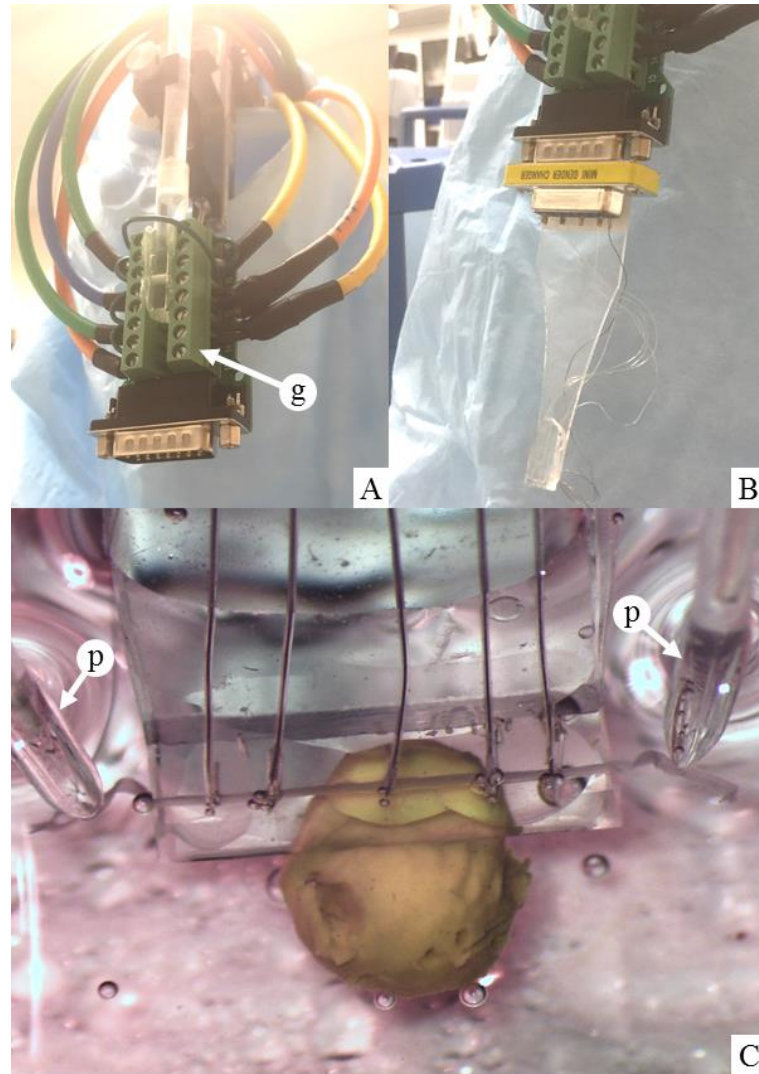
Figure 3.4 Assembled devices and external connections. A) Colored amplifier cables are shown secured to the screw terminals of a 15-pin breakout board connected to a DB-15 male connector (see item "g" in Table 3.1). A plastic rod glued to the breakout board connected it to a micromanipulator. B) Microchannel module connected to the amplifier and ready for a recording session. C) Finished microchannel recording from a teased rootlet. Glass pipette tips of the suction electrodes used to stimulate the rootlet are labeled "p".

A circular coil of bare Ag/AgCl wire placed in the bath behind the microchannel served as a reference terminal for all electrodes. This was made in a similar fashion to the electrode wires and had a DB-9 pin crimped to the non-coiled end that was plugged into one of the pin receptacles on the DB-25 adapter in the electrode assembly (labeled "b" in Figure 3.3 I). The screw terminals associated with the negative inputs of the amplifiers were shorted using jumper wires and connected to the screw terminal associated with the reference coil (green jumper wires visible in Figure 3.4 A).

3.2.3.4 Modular devices

Assembled devices could be conveniently handled as individual self-contained units and safely stored when not in use. Prior to a recording session, the unit was plugged into a 15-pin DB female connector attached to a breakout board where the cables going to the amplifier inputs were attached (Figure 3.4 B). A plastic rod glued to the breakout board connected microchannel assemblies to a micromanipulator (Figure 3.4 A). This produced a modular system that enabled different microchannels to be easily and reproducibly connected to their respective amplifier channels while permitting channels to be secured and precisely positioned, an important feature when recording from dorsal rootlets in anesthetized rats. Figure 3.4 C shows a competed microchannel containing a teased rootlet.

3.2.3.5 Materials and costs

Table 3.1 lists the items used to fabricate microchannels and their associated costs. Lower-case letters in the left column identify items in the previous figures. Material costs were $15.04 per device and this included the breakout board (item "g") which only needs to be purchased once and is not a "per device" item. Bulk material costs were $376.38. These

31

did not include additional supplies such as a glass cutter for trimming microscope slides ($3.47 Husky, 5 in., Home Depot), super glue ($8 for six 0.1 oz tubes, Walgreens), razor blades ($3.97 for a 25 pack, Home Depot) and bleach ($4.49, 3.84 qt, Target) which we estimated totaled $19.93. Including these items would bring the bulk cost to $396.31. PDSM can be cured using many different heat sources and the cost of our hot plate was not included nor were the costs of typical laboratory equipment such as surgical tools, microscope, amplifiers, cables, etc.

Table 3.1 Microchannel materials and costs

Table 3.1 Materials and costs

	Item	Company	Purpose	Specs	Bulk cost	Qty	Unit	$/ Unit	Units/ device	$/ device
a	PDMS (Sylgard 184)	Ellsworth Adhesives	channel	2 part (A/B mixture)	$110.00	500	g	$0.22	5	$1.10
b	bare silver wire	A-M Systems (# 782000)	channel (guide), ref. terminal	0.008"	$51.00	300	in.	$0.17	5	$0.85
c	PFA-coated silver wire	A-M Systems (# 785500)	electrodes	0.003" bare, 0.0055" coated	$84.00	300	in.	$0.28	15	$4.20
d	1080 spring steel wire	McMaster-Carr (# 8907K88)	electrodes (guide)	0.006"	$10.67	1200	in.	$0.01	1	$0.01
e	DB15 mini f/f gender changer	CablesOnline	connector	15 pin	$18.48	10	pcs	$1.85	1	$1.85
f	D-sub male pins	B & R Electronics Supply	connector	gold-plated	$10.12	100	pcs	$0.10	6	$0.61
g	DB-15 male breakout board	JoJa-US	connector	15 pin	$10.59	2	pcs	$5.30	1	$5.30
h	microscope slide	VWR International (# 48311-703)	base	25 x 75 x 1 mm	$81.52	72	pcs	$1.13	1	$1.13
					bulk cost $376.38				cost per device	$15.04

3.2.4 Bench tests

3.2.4.1 Electrical

To check for signs of exposed electrode wires, the bubble test was performed in a saline bath with the ends of the channel plugged by short lengths of 200 µm OD nylon fishing line. Any exterior locations which produced bubbles were dried, coated and cured with

PDMS, and re-checked until all bubbles tests were negative. Electrode continuity was checked in a similar fashion except with the ends unplugged and the channel filled with saline in the bath.

3.2.4.2 Impedance

The resistance of each electrode wire to a 1000 Hz sinusoidal signal was measured prior to each recording session using an impedance meter (Model IMP-2AMC, MicroProbes for Life Sciences, MD). The bubble test was always performed on the electrodes and reference terminal prior to taking any impedance measures.

Two methods were employed – one to measure an electrode's total impedance in the channel and another to measure only the impedance of the metal/electrolyte interface. The first method measured the impedance between the electrode lead wire and the ground wire in the saline bath. This impedance is the sum of the resistance associated with the metal/electrolyte interface and the "tube resistance" (Loeb et al., 1977), equal to the resistance of the portion of saline to the left of the electrode in parallel with that on the right.

The second method aimed to characterize only the impedance of the metal/electrolyte interface at each electrode independent of tube resistance. This was done by connecting the reference terminal of the meter to a 100 μm diameter bare tungsten wire and inserting it into the channel until its tip came within a few hundred microns of the desired electrode, thus effectively shorting the tube resistances.

3.2.5 *In vitro* assessment

Chapter 4 provides a detailed description of the experimental setup and methods used to record neural signals using the device described here. Briefly, dorsal roots were explanted from anesthetized adult Sprague-Dawley rats which had been perfused with cold (1-4 °C) Hanks balanced salt solution (HBSS). Roots were placed in a warm HBSS bath (37 °C) and surgically divided into smaller strands, or "teased rootlets", thin enough to be drawn through the microchannel using a short piece of suture (8-0) tied to one end of the teased rootlet. Suction electrodes (A-M Systems, WA) connected to the rootlet on either side of the channel (Figure 3.4 C, label "p") were used to elicit action potentials traveling to the right or left through the channel. Recorded signals were amplified (x 10,000), bandpass filtered (10-20,000 Hz), notch filtered (60 Hz), sampled (100,000 Hz) and stored on a computer for offline analysis. Recorded signals were bandpass filtered (100-10,000 Hz) in Matlab (Mathworks, CA) prior to analysis.

3.3 Results

3.3.1 Total impedance

Table 3.2 shows total impedance values measured in physiological saline at room and other temperatures at different time points. As expected, impedance values were consistently lowest at the channel ends (electrodes 1 and 5) and highest at mid-channel (electrode 3). This was expected since tube resistance is largest at mid-channel and falls off towards the channel ends. Impedance values were slightly different at different time points, but those measured on Day 1 and 42 were nearly identical, suggesting the electrical properties of the electrodes remained stable over time. Electrodes had similar impedance values at different

temperatures (Days 1 and 42) and different impedance values at similar temperatures (Days 1 and 22) suggesting impedance was unaffected by temperature.

Table 3.2 Total impedance

Table 3.2 Total impedance (kΩ)[1]

Day	Electrode #					T (℃)
	1	2	3	4	5	
1	19	31	38	30	19	22
8	20	36	40	34	20	31.6
12	15	27	36	27	17	35.4
22	22	37	50	37	24	20
36	22	35	46	37	24	21.5
42	20	32	38	28	20	31
mean	19.7	33.0	41.3	32.2	20.7	-
std	2.6	3.7	5.5	4.4	2.8	

[1]tests conducted in physiological saline using a 1000 Hz sinusoidal signal

3.3.2 Metal/electrolyte interface impedance

Using the second method previously described, we measured the metal/electrolyte interface impedance to be 10 kΩ at each electrode on Day 1, when the device was initially fabricated. Metal/electrolyte impedance values were slightly elevated a month later (Day 36) ranging between 11-17 kΩ with an average impedance of 15 kΩ. A bubble test revealed electrode 2 had a slight metal exposure. This did not appear to have impacted the electrical properties of electrode 2 since electrode 4, its fully sealed counterpart on the right side of the channel, had nearly identical impedances at all prior time points (Table 3.2). Nevertheless, the site was sealed with PDMS until bubble tests were negative (i.e. produced no bubbles).

3.3.3 Neural signals

Examples of recorded signals are shown in Figure 3.5. Stimulus currents ranging between 0-3 µA were applied to the left side of the rootlet eliciting action potentials that traveled to the right. No signals were elicited when stimulating in the 0-0.5 µA range. All-or-none bursts of activity characteristic of action potentials occurred on all electrodes when current levels were increased to 1 µA. As predicted by theory, the responses at electrode 4, offset 2 mm to the right of mid-channel, had negative peaks that were at least as large as those at mid-channel with the mean response (white lines) at 4 being larger than 3. Signals increased when stimulus current was increased to 2 µA, corresponding to activity in more than one axon being elicited.
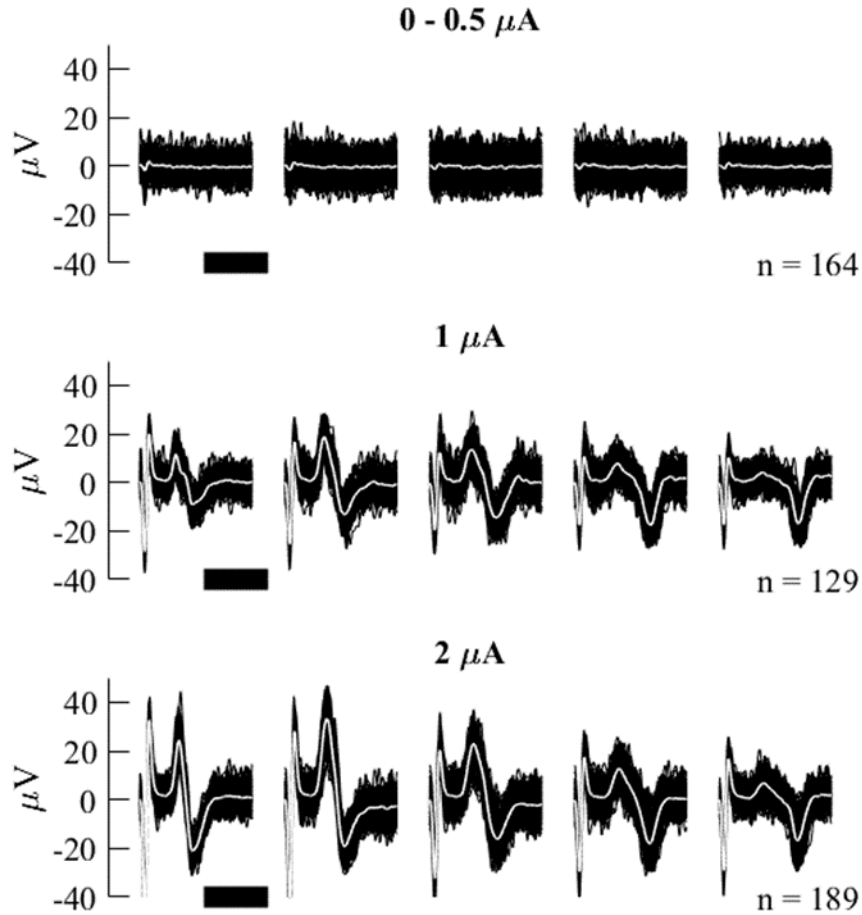
Figure 3.5 Example of recorded signals. Recorded neural signals when a teased dorsal rootlet was stimulated on the left side eliciting action potentials traveling to the right. Responses are taken from Rat 59 (see Chapter 4) in a single 70 second trial where stimulus amplitudes were increased in increments of 0.5 µA every 10 seconds. Signals for electrodes 1-5 appear left to right in each row with "n" spikes aligned to their stimulus pulses and superimposed on each other. White lines represent mean responses. Horizontal scale bar represents 0.1 ms.

3.4 Discussion

Based on methods described by FitzGerald and colleagues (FitzGerald et al., 2009), we developed a hand-based approach to fabricate microchannel devices using low-cost off-the-shelf components. FitzGerald described having to discard devices where PDMS had compromised the inner-facing surfaces of the electrodes. We sought to avoid this potential issue by making the PDMS substrate first and then using it (via the slits) to form a seal that

prevented additional PDMS from contaminating the inner-facing surfaces of the electrode wires. This approach also enabled electrodes to be precisely positioned and prevented them from shifting to the left or right at any time during the fabrication process once they had been threaded into the slits. We feel these techniques can be readily adapted for making channels having inner diameters smaller or larger than 200 µm simply by choosing different diameters for the Ag wire used to construct the channel and the temporary steel guide wire, which determined the inner diameter of the electrodes (items "b" and "d" in Table 3.1). Devices were designed to be modular so that microchannels having different dimensions or electrode configurations could easily be swapped out in a "plug-and-play" fashion during recording sessions, if desired.

Compared to the standard approach of curing PDMS in an oven for many hours (i.e. 4 hours) (FitzGerald et al., 2009), our technique of flash-curing the PDMS on a hot plate significantly decreased fabrication times and permitted rapid prototyping of microchannel devices. Our devices could be made in approximately 4-6 hours and cost about $15 each in materials. This compares favorably with clean room equipment costs and the time necessary for learning to use this equipment and to implement the many steps associated with making devices using photolithography. We obtained an estimate of $2500 to produce similar devices in batches of 80 using photolithographic techniques in a clean room environment (Motorola Nanofabrication Research Facility, Florida International University, Miami, FL).

We never encountered problems with electrodes demonstrating a lack of continuity. Impedance values were slightly elevated on Days 22 and 36, particularly at electrode 3.

This suggested tube resistance was higher during this period since the mid-channel resistance was impacted more than the other electrodes, as one would expect (Figure 3.5). The reason for this was not clear but it is possible that channels were more constricted due to less use and, therefore, drying out over this period. Although microchannels were thoroughly flushed with water and saline following recording sessions, it is also possible that tissue remnants could have coated portions of the electrodes. This could partly account for the increase in the metal/electrolyte impedance observed on Day 36. Nevertheless, on any given day, impedance values for electrodes on the left side were nearly equivalent to their counterparts on the right. This suggested our methods for situating electrodes inside the channel had a high degree of reproducibility and produced recording sites with nearly equivalent electrical properties.

Despite its wide-spread use as an experimental platform for microchannel investigations, there is evidence that the teasing process damages axons. A study in which rat dorsal roots were teased apart and inserted into a chronically implantable microchannel array for up to 3 months in rats (Chew et al., 2013) found the proportion of intact axons to be 75% and 60% one and four weeks, respectively, following the initial surgery. We observed the teasing process significantly elongated rootlets, which can sustain strains of between 15-25% before axons are irrevocably ruptured (Sunderland and Bradley, 1961). Frequently, neural responses were only observed at the one or two electrodes near the ends of the channel closest to the site of stimulation. This suggests the presence of axonal fragments and a lack of axonal continuity through the channel. A close examination of the negative peak amplitudes for the 2 μA scenario in the 3rd row of Figure 3.5 shows electrode 1,

nearest the site of stimulation, had the largest signals. This is not consistent with theory, which predicts that signals are expected to increase as they approach mid-channel. We believe this reflects activity in axonal fragments that extend no further than 1 or 2 mm into the channel. Similar signal patterns can be observed in microchannel recordings using rootlets prepared using the same teasing process described here (Gribi et al., 2018), although this was not highlighted or mentioned.

Due to their small size and the need to precisely control electrode and channel geometries, most microchannel technologies have been fabricated using advanced photolithographic techniques (Delivopoulos et al., 2012, Minev et al., 2012, FitzGerald et al., 2012, Dworak and Wheeler, 2009). While these have excellent recording capabilities, their development is limited to a handful of investigators possessing the expertise and resources (financial, facilities, collaborators) necessary to construct these devices using photolithography. The approach described here can serve as a vehicle for a broader group of researchers, particularly students, to develop, explore and innovate microchannel-based neural interfaces.

CHAPTER 4

THEORETICAL FRAMEWORK AND EXPERIMENTAL EVIDENCE FOR SIGNAL

ENHANCEMENT AT OFFSET ELECTRODES

4.1 Introduction

Over the past decade, microchannel electrodes have emerged as promising devices for recording signals in peripheral nerves. This is because they combine chronic capability with enhanced selectivity. Like cuff electrodes, microchannel electrodes have the potential to be chronically viable nerve interfaces – i.e. the ability to maintain stable long-term connections with small populations of axons (FitzGerald et al., 2012, Chew et al., 2013). Like many of the penetrating non-chronic neural interfaces, they are highly selective – i.e. able to record signals from individual axons (Dworak and Wheeler, 2009, FitzGerald et al., 2009, Delivopoulos et al., 2012, Minev et al., 2012).

Perhaps because of a shared architecture that surrounds nerve fibers, most microchannel electrodes have inherited electrode configurations from their larger cuff-electrode precursors where a mid-channel electrode records neural signals relative to a reference terminal created by shorting together electrodes located near the ends of the channel. This pseudo tripole arrangement was appropriate for cuffs for two reasons. First, cuffs enclose many thousands of axons and are typically unable to distinguish signals from individual axons and, second, because of their size and proximity to muscles, cuffs record large EMG artifacts which the pseudo tripole helps to minimize (Stein et al., 1975, Stein et al., 1977). However, the pseudo tripole arrangement cannot effectively be used to distinguish between

action potentials traveling in opposite directions and significantly limits microchannel capabilities, as discussed previously.

Off-center, or "offset", recording sites have been theorized to record larger signals than those at mid-channel although no mechanism to explain this prediction has been proposed (FitzGerald et al., 2008). Recent experimental work appears to validate these predictions without speculation as to their underlying cause (Gribi et al., 2018). Also, due to their inherent asymmetry, offset electrodes are expected to record different neural signatures for action potentials traveling in opposite directions. Unlike the symmetric pseudo tripole configuration, this feature could enable afferent neural signals to be differentiated from efferent ones.

Despite these apparent advantages, no efforts have been made to our knowledge to explain the basis for signal enhancement at offset electrodes. A theoretical understanding of this phenomenon is needed to explore the extent to which offset electrodes could be used to enhance signals or differentiate between action potentials traveling in opposite directions. The ubiquitous pseudo tripole reference is unsuitable for rejecting unwanted EMG and other external noise artifacts at offset electrode locations. Therefore, alternative reference configurations need to be explored and identified.

Previously, in Chapter 3, we provided a rational basis to explain signal enhancement at offset electrodes. The "difference" term in a former theory of neural recording was used to justify the design of a microchannel containing offset electrodes, particularly their optimal locations, and the analysis assumed simplified APs with triangular spatial profiles.

In reality, the "difference" term only characterizes spatial relationship in the longitudinal direction which served to justify optimal electrode placements. However, it ignores cross-sectional relationships, such as the axon's diameter relative to the channel's and differences in conductivity between axoplasm and the environment surrounding the axon, factors which play a significant role in determining recorded signal amplitudes. Also, realistic action potentials travel over a greater range of speeds than what we assumed and have curvilinear waveforms that may produce different signals than those predicted when APs are assumed to be triangular. Furthermore, non-neural signals, such as external noise artifacts outside the channel and ambient background noise arising from sources inside the channel, significantly impact recorded signals. These factors cannot be ignored if a complete picture of offset electrode performance is to emerge.

The main goals in this chapter are to present a comprehensive theoretical framework to predict signals at offset electrodes in microchannels and experimentally validate these predictions. We hypothesize offset electrodes to record larger signals than the one positioned at mid-channel and that signal differences could be used as a basis for differentiating between efferent and afferent neural activity.

To date, a comprehensive theoretical model for neural recording in microchannels is lacking in the literature. Neural recording theory was originally developed primarily for recording using cuff electrodes (Stein and Pearson, 1971) although its applicability to smaller channel cross-sections was recognized early on (Loeb et al., 1977). This theory predicts neural signals and external noise artifacts, but does not account for signal losses due to current shunting by the layer of low-resistance saline which fills the space between

the nerve and inner wall of the channel (Stein and Pearson, 1971). Theoretical models which incorporate a saline layer typically do not characterize noise artifacts (Struijk, 1997, Meier et al., 1998a). A finite element (FE) model which included both a saline layer and external and ambient noise artifacts did not explore signals at offset recording sites (Sabetian et al., 2017), and one that predicted larger signals at an offset location did not include a saline layer or noise artifacts of any kind (FitzGerald et al., 2008). Recent experimental work suggests that offset electrodes have improved SNR over mid-channel placements (Gribi et al., 2018) in microchannels. Another study demonstrated improved 50 Hz power line noise rejection at mid-channel in a microchannel configured with a pseudo tripole reference (FitzGerald et al., 2009). However, to our knowledge, no efforts have been made to provide a theoretical basis for improved SNR at offset electrodes.

The Stein and Pearson model (S&Pm) upon which our model is largely predicated has been referred to as the "1D model" since signals are assumed to vary only in the longitudinal direction. While transverse currents would cause signals to decline in the radial direction, FE models show these currents are negligible (Meier et al., 1998a, FitzGerald et al., 2008) inside microchannels and even in cuffs with radii less than 2 mm (Struijk, 1997). The S&Pm also assumes extracellular voltages at the channel ends to be zero, which cannot be entirely true since this would imply an absence of action currents, and, therefore, a cessation of the action potential. However, the assumption is valid to the extent that signals predicted by the S&Pm were in close agreement to those predicted by a FE model that imposed no restrictions on the signals at the channel ends (Struijk, 1997, Taylor et al., 2004). Compared to FE models, the S&Pm has the advantage of being readily employed

45

to solve the inverse problem, namely, of predicting action potential waveforms shapes using recorded neural signals as inputs to the model. We demonstrate the potential use of this by formulating the "difference" term as a matrix that transforms spatial relationships that change over time into a temporal signal at a single location in space (i.e. an electrode).

Since the S&Pm relies on AP spatial profiles, we felt the model's predictive capability would be enhanced if AP profiles were based on empirical observations of their durations, rise times and speeds. Therefore, we developed a model of the temporal characteristics previously documented by Paintal for APs having different speeds and used it to construct crude triangular waveforms which were then transformed into more realistic AP profiles using a smoothing function.

Here, we extend the S&Pm to include a saline shunt around the nerve which we anticipated would improve the model's capacity to accurately predict signal amplitudes. Additionally, a noise term is added to model ambient background noise since this impacts the SNR at different recording sites inside the channel. Triangular and realistic AP waveforms were incrementally advanced to the right and left through a microchannel and the expected neural signal was computed at all relevant longitudinal positions inside the channel using the model. Neural recordings obtained using a microchannel containing offset electrodes, previously developed in our lab, were compared to theoretical predictions potential and the potential to use offset electrodes to preferentially sense AP directionality is explored and discussed. External and background noise signals recorded at offset electrodes are compared to model predictions and used to justify improved SNR and demonstrate different reference configurations for canceling external noise artifacts at offset electrodes.

46

4.2 Methods

4.2.1 Model

4.2.1.1 Action potential waveforms

Triangular AP spatial profiles were constructed from duration and rise time data collected by Paintal who documented temporal characteristics for APs traveling at different speeds in nerve filaments dissected predominantly from the vagus and saphenous nerves in adult cats (Paintal, 1966). The product of duration and conduction velocity were used to determine an AP's wavelength (wl) which we found varied linearly with conduction velocity. A best-fit line through this data permitted wavelengths to be estimated for APs traveling at any speed. Similarly, the product of rise-time and conduction velocity produced rising phase lengths (rpl) that were also observed to correlate linearly with conduction velocity. A best-fit line through this data permitted rising phase lengths to be estimated for APs traveling at any speed, v. Figure 4.1A shows the linear relationships between conduction velocity and wavelengths and rising phase lengths that we obtained from durations and rise-times observed by Paintal for APs at 37.1 °C. Mathematically, these relationships are:

$$(1) \qquad wl_{37.1°C} \quad = \quad 0.305 \cdot v + 3.56$$

$$(2) \qquad rpl_{37.1°C} \quad = \quad 0.0765 \cdot v + 0.849$$

Paintal showed that temperature impacts the temporal dynamics of action potentials and provided Q_{10} factors to permit rise-times and durations observed at one temperature to be adjusted to match those observed at another temperature. The Q_{10} factors of 3.4 and 2.5

computed by Paintal were used to adjust AP wavelengths and rising phase lengths, respectively, for temperatures different from a reference temperature of 37.1 °C. These expressions are given below:

$$(3) \qquad wl_T \;\; = \;\; \frac{wl_{37.1°C}}{3.4^{(T-37.1°C)/10}}$$

$$(4) \qquad rpl_T \;\; = \;\; \frac{rpl_{37.1°C}}{2.5^{(T-37.1°C)/10}}$$

Rise times and durations are shorter at temperatures higher than 37 °C and result in shorter, more spatially compact, action potentials whereas lower temperatures have the opposite effect and correspond to longer APs that are more spread out on the axon. Figure 4.1C shows the spatial profiles of a 20 m/s AP at three different temperatures. The effect on wavelength is significant. A difference of 1 °C above and below 37 °C results in wavelengths that are shorter and longer, respectively, by approximately 1 mm which is 10% of the 10 mm wavelength depicted for the AP at 37 °C. Therefore, it was important to document temperature during recording experiments since the spatial profile of an AP's transmembrane voltage determines the neural responses predicted by Eq. 7.

Finally, Paintal computed AP fall-time by subtracting rise-time from duration. Similarly, falling phase lengths (fpl) were computed by subtracting the rising phase length obtained using in Eq. 4 from the wavelength obtained using Eq. 3 as shown below:

$$(5) \qquad fpl_T \;\; = \;\; wl_T - rpl_T$$

Rising and falling phase lengths were used to construct triangular action potentials with pointed peaks and sharp transitions between the resting membrane potential at 0 mV and their rising and falling phases.

Naturally occurring action potentials have rounded peaks with rising and falling phases that transition smoothly from and to the resting membrane potential. Plonsey and Barr suggested that AP waveforms could be modeled parametrically by a pair of hyperbolic tangent functions, one to represent the rising phase and the other to represent the falling phase (Plonsey and Barr, 2007). A similar approach was taken here and the following function was used to simulate realistic AP waveforms:

$$(6) \qquad y \;=\; \frac{1}{2}\,tanh\left(\frac{x - a_1}{w_1}\right) - tanh\left(\frac{x - a_2}{w_2}\right)$$

The "fit" function in Matlab was used to compute the constants a_1, w_1, a_2 and w_2 to obtain a set of "y" points that represented a best-fit curve through triangular AP profiles represented by the set of "x" points. Figure 4.1B shows triangular and their corresponding realistic waveforms for slow, medium and fast action potentials having speeds of 2, 20, and 50 m/s, respectively. Faster APs are seen to be more spatially spread out along the axon – i.e. have longer wavelengths - as specified by Eq. 1. In all simulations, we chose 120 mV as the peak of the transmembrane potential (Figure 4.1B). Realistic waveform peaks slightly lag those of their triangular counterparts and their overall wavelengths are slightly longer to permit smooth transitions to the resting membrane potential, here, at 0 volts. These slight differences are necessary to preserve the rise times and durations that Paintal documented using the methods he described (Paintal, 1966).
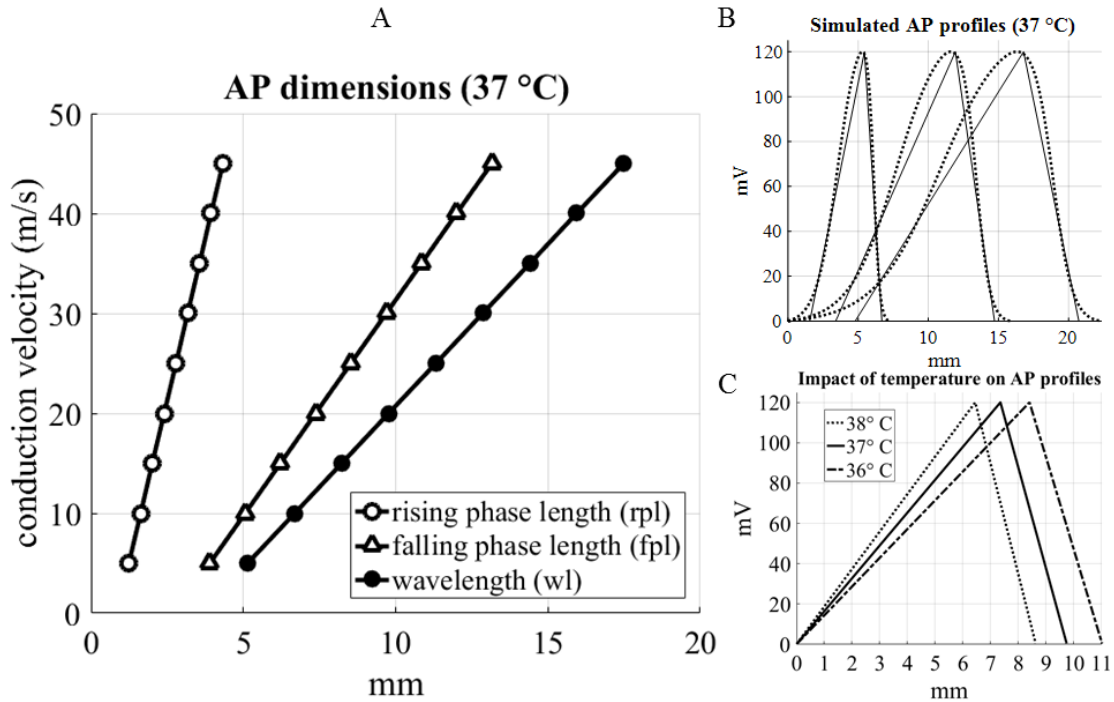
Figure 4.1. Simulated action potential waveforms. A) Wavelengths (wl) and rising phase lengths (rpl) are modeled versus conduction velocity using measurements from Paintal (Paintal, 1966) with falling phase lengths (fpl) computed as their difference (wl-rpl). B) Transmembrane potential spatial profiles for triangular (solid) and realistic (dotted) APs traveling to the right at 2 m/s (far left), 20 m/s (middle), and 50 m/s (far right). C) One degree above and below 37 °C shortens and lengthens, respectively, the wavelength of a 20 m/s right-bound AP by about 1 mm.

4.2.1.2 Governing equation

For predicting extracellular voltages inside microchannels, we used a model that we felt

could provide a rationale as to why offset electrodes might be expected to record the largest

signals in microchannels. As mentioned previously, the finite element model developed

by FitzGerald predicted this phenomenon without exploring its possible cause (FitzGerald

et al., 2008). The model we used predicts neural signals in time as a function of their

position in relation to the microchannel. It was first developed by Stein and Pearson for

single action potentials traveling in unmyelinated axons (Stein and Pearson, 1971) and later

shown to apply equally well for predicting signals originating in myelinated axons (Marks

and Loeb, 1976). Compared to the Marks and Loeb model, the Stein and Pearson model included a term that could be used to model the effects of external noise sources on signals inside the channel. We felt it was important to model external noise artifacts since implantable devices for recording neural signals will also record signals from non-neural sources such as EMG from nearby muscles and, from a signal-to-noise standpoint, the ability to suppress undesired signals equates to enhancing the desired one. Equation 7 below reproduces the Stein and Pearson model. We added an addition term, n(x), to model internal noise sources originating from inside the channel:

$$
\overset{\displaystyle 1.}{\overbrace{\qquad\qquad\qquad}} \quad \overset{\displaystyle 2.}{} \quad \overset{\displaystyle 3.}{}
$$

$$
(7) \qquad v_e(x) \;=\; \alpha \cdot \underbrace{[e_m(x) - v_m(x)]}_{\text{``difference''}} \;+\; e_e(x) \;+\; n(x)
$$

Equation 7 states that the extracellular voltage inside the channel at any longitudinal position "x" is a combination of neural and noise sources. It predicts that differences in voltage between the channel's ends have a linear distribution inside the channel. In this way, the channel acts as a variable resistor where voltage drops are proportional to the distance from the ends. The $e_m(x)$ and $e_e(x)$ terms in Eq. 7 are associated with these linear voltage profiles and shown as dashed diagonal lines in the neural and external noise terms in Figure 4.2, respectively. The $e_m(x)$ term plays an important role in shaping neural signals while the $e_e(x)$ predicts noise amplitudes from external sources such as EMG or other artifacts originating outside the channel.

Figure 4.2 Physical representation of terms in the governing equation for predicting signals in microchannels. Neural signals are the product of two spatial terms. 1) a "difference" term and 2) a factor "α". The "difference" term characterizes attenuation of signals due to geometrical constraints along the channel's axis and the factor "α" embodies spatial relationships orthogonal to this axis, parallel to the channel's cross-section. Alpha characterizes the significant size difference between axonal cross sections and the surrounding environment which contributes significantly towards reducing the proportion of the transmembrane voltages that can be recorded extracellularly. External and internal noise artifacts add to the neural signals. In term 1, the transmembrane potential's spatial profile, $v_m(x)$ is depicted with triangular waveform.

4.2.1.3 Neural signals

Neural signals originate from transmembrane currents which, in turn, produce extracellular currents that generate small voltages that can be recorded outside the active axon. This is

represented in the first term of Eq. 7 as the product of a scaling coefficient "α" and a "difference" term, in brackets. Alpha is the fraction of the transmembrane voltage that exists outside the axon (Hodgkin and Rushton, 1946). It essentially equals the ratio of the axonal to extracellular conductance since the axonal conductance is many times smaller than that of the extracellular environment. Alpha is partly influenced by differences in conductivity between the axoplasm, σ_a, and the extracellular environment but mainly by the ratio of the axon's cross-sectional area, A_a, to the cross-sectional area of the extracellular environment surrounding the axon inside the channel. Extracellular conductance is exponentially smaller for smaller channel cross-sections and this underscores the basis for signal enhancement in microchannels compared to cuff electrodes (Marks Loeb and Beatty 1976; FitzGerald 2008). Since axonal cross sections are typically many orders of magnitude smaller than the space surrounding them, "α" is usually 1000-10,000 times smaller than unity. Neural signals in microchannels are therefore in the range of 10-100 µV, assuming a peak transmembrane voltage of around 100 mV.

In our experiments (see below), there was often space between the rootlet and the channel's inner surface. This space was filled with Hanks balanced salt solution (HBSS) which, being more conductive than neural tissue, shunts extracellular currents to ground and reduces recorded signal amplitudes. Shunting through highly-conductive media has been demonstrated in models (Stein and Pearson, 1971, Struijk, 1997, Meier et al., 1998b). Therefore, we modeled the external environment surrounding the active axon as a pair of cylinders having different axial conductivities. The inner cylinder represents the nerve rootlet with a cross-sectional area, A_n, and conductivity σ_n. The outer cylinder represents

the saline shunt with a cross-sectional area, A_s, equal to the difference between the channel and rootlet cross-sections. It is filled with HBSS having a conductivity σ_s. These cylinders each conduct portions of the overall extracellular current in proportion to the resistance each poses to extracellular currents making their way towards the channel ends. This equates to a pair of resistors in parallel and therefore, their net conductance, g_e, equals the sum of their individual conductances, g_n and g_s. The expressions we used to compute α are given below.

$$(8) \qquad \alpha \;=\; \frac{g_a}{g_a + g_e} \;\approx\; \frac{g_a}{g_e} \quad (\text{since } g_a \ll g_e)$$

where,

$$(9) \qquad g_e \;=\; g_n + g_s$$

and,

$$(10) \qquad g_a \;=\; \sigma_a A_a \;, \qquad A_a = \tfrac{1}{4}\pi a^2$$
$$(11) \qquad g_n \;=\; \sigma_n A_n \;, \qquad A_n = \tfrac{1}{4}\pi d^2$$
$$(12) \qquad g_s \;=\; \sigma_s A_s \;, \qquad A_s = \tfrac{1}{4}\pi(b^2 - d^2)$$

Neural signals are also attenuated when channels are shorter than AP wavelengths. In these cases, non-zero transmembrane voltages are always present at the ends of the channel and their linear distribution, represented by $e_m(x)$ in Eq. 7, subtracts from the amplitude of the transmembrane voltage. The "difference" portion of the neural signal term represents this attenuation with $e_m(x)$ represented mathematically as:

$$(13) \qquad e_m(x) \;=\; \frac{v_m(L) - v_m(0)}{L}x + v_m(0)$$

4.2.1.4 Axonal diameters

Myelin sheath (i.e. "fiber") diameters, a', have been shown to correlate linearly with conduction velocity (Hursh, 1939, Boyd and Kalu, 1979, Ritchie, 1982) and a best fit-line through data pooled from Hursh, Boyd & Kalu, and Ritchie (see Figure 4.3) was constructed and used to estimate fiber diameter from conduction velocity:

$$(14) \qquad a' \quad = \quad \frac{v + 4}{5.6}$$
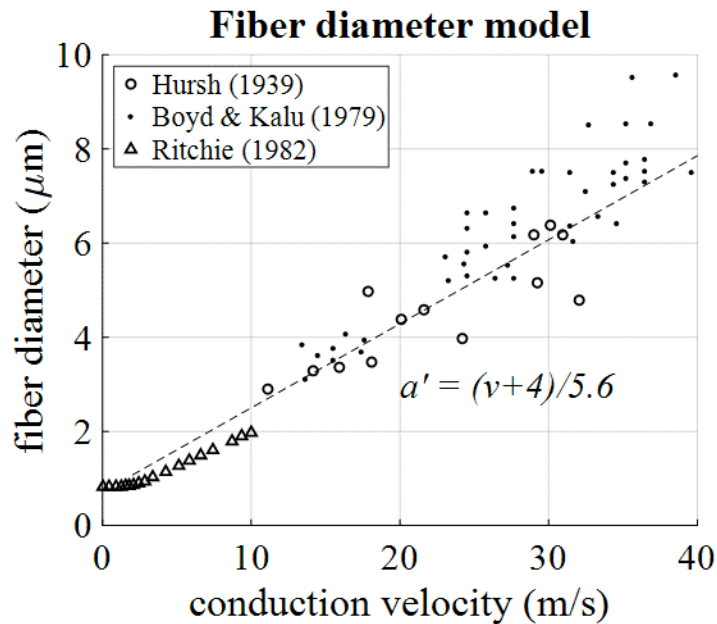
Figure 4.3 Fiber diameter model. Linear model (dashed line) used to estimate fiber diameter from conduction velocity. Points reproduce datasets from earlier studies (see plot legend).

Axonal diameters were determined by multiplying fiber diameter by the g-ratio, the ratio of axonal diameter to their myelin sheath diameter. This relationship is given by:

$$(15) \qquad a \quad = \quad g \cdot a'$$

4.2.1.5 Rootlet diameters

Rootlet diameters were varied in simulations. A diameter of 0 µm was used to establish a lower limit for expected signal amplitudes since this assumption produced a maximally conductive channel filled only with saline and no neural tissue to prevent extracellular currents from being maximally shunted to ground. A rootlet diameter equal to the channel diameter of 200 µm was used to establish an upper limit for expected signal amplitudes since this represents a minimally conductive channel filled only with neural tissue and no saline shunt. Experimentally, rootlet diameters ranged between approximately 100 µm to slightly less than 200 µm. Simulated neural recordings used rootlet diameters in this range.

4.2.1.6 External artifact noise

The second term in Equation 7, $e_e(x)$, predicts that external voltage differences occurring between the ends of the channel are linearly distributed over its length. The linearization of external voltage artifacts is represented mathematically as:

$$(16) \qquad e_e(x) \quad = \quad \frac{v_e(L) - v_e(0)}{L} x + v_e(0)$$

Unlike the values of the transmembrane voltage at each end of the channel, $v_e(L)$ and $v_e(0)$ were not simulated. Instead, we quantified the degree to which external artifact voltages generated by the stimulator used to elicit APs in rootlets were linearly distributed inside the channel.

4.2.1.7 Background noise

Ambient background noise was assumed to arise predominantly from ions moving randomly about inside the channel. The root-mean-square amplitude of the thermal, or Johnson, noise increases as the square root of the total resistance from each electrode to ground (R'(x)), temperature of the media (T) and bandwidth (B) of the recording apparatus as described by:

$$(17) \qquad n(x) \;\; = \;\; \sqrt{4k_B T B \cdot R'(x)}$$

where k_B is the Boltzmann's constant equal to $1.38e^{-23}$ J/°K. Temperatures in °K were readily obtained by adding 273° to the temperatures we noted in °C for each neural recording. Neural recordings were obtained with the A-M System 1700's upper and lower cutoff frequencies set to 10 and 20000 Hz, respectively. According to the user manual, these are 2nd order Butterworth filters. For analysis purposes and to remove any lingering baseline (i.e. DC) and high-frequency components, all neural signals were filtered offline using a 2nd order Butterworth filter with a passband range of 100-10000 Hz. Therefore, a bandwidth of 10,000 Hz was used for Johnson noise calculations.

As described by Loeb, Marks and Beatty in (Loeb et al., 1977), the total resistance at each electrode, R'(x), may be estimated as the metal/electrolyte interface impedance, R_0, at each electrode in series with the "tube" resistance, $R_t(x)$, at each electrode. While these authors provide a theoretical approach for calculating the metal/electrolyte interface impedance, we chose to measure it directly. This was done by inserting a ground wire into the middle of the channel until its end nearly touched the electrode of interest. In this way, the tube

resistance was negligible and the measured impedance was predominantly due to the metal/electrolyte interface. This resistance was found to be nearly constant for each electrode and consistently measured about 10,000 Ω over the time frame that experiments were done. Thus, the total resistance, R' was computed using the expression:

$$(18) \qquad R'(x) \;=\; R_0 + R_t(x) \quad, \quad R_0 = \text{electrode/HBSS impedance}$$

Tube resistance, R_t, is the resistance of fluid to the left of a given electrode in parallel with the resistance to the right. Therefore, we expected the mid-channel electrode to have the highest tube impedance with offset electrodes having smaller impedance values. Tube resistance as a function of longitudinal position in the channel was calculated using the expression below with, g_e, the total conductance of the channel's cross section the same as previously described:

$$(19) \qquad R_t(x) \;=\; \frac{x(L-x)}{L} \cdot \frac{1}{g_e}$$

Eq. 19 suggests that tube resistance is parabolic with channel position, peaking at mid-channel (i.e. x = L/2) and falling to zero at the ends. Since Eq. 17 includes this term in the square root, we expected Johnson noise profiles in the channel to have similar characteristics. The dome-shaped dashed line in Figure 4.2 is representative of the types of profiles we expected to record for noise generated inside the channel. Finally, recorded signals were measured relative to a reference terminal as expressed by:

$$(20) \qquad v_r(x) \;=\; v_e(x) - V_{ref}$$

In experiments, a coil of chlorinated silver wire placed in the HBSS bath surrounding the rootlets and the recording setup served as a common reference terminal for all electrodes in all experiments.

4.2.1.8 "Difference" term

The "difference" term in Eq. 7 at any channel position changes in time as an action potential moves through the channel. This was computed by constructing a square, N x N sparse matrix, **A**, with columns representing the channel's position relative to the action potential's spatial profile and rows representing increments in time. The product of matrix **A** and a space-valued column vector X, containing $v_m(x)$, produces a time-valued column vector Y representing the "difference" at each instant. Thus, matrix **A** transforms spatial relationships into a temporal domain and is described by:

$$(21) \qquad Y \ = \ \boldsymbol{A} \cdot X$$

with **A** given by:

$$
\begin{array}{c}
\overbrace{\hspace{20em}}^{N} \\
\overbrace{\hspace{9em}}^{L/\Delta x}\;\overbrace{\hspace{8em}}^{wl/\Delta x} \\
\overbrace{\hspace{6em}}^{x/\Delta x}\qquad\overbrace{\hspace{2.5em}}^{\Delta x}
\end{array}
$$

$$
(22)\qquad A \;=\; \left.\begin{bmatrix}
w_L & 0 & \cdots & w_x & \cdots & 0 & w_0 & 0 & 0 & 0 & 0 \\
0 & w_L & 0 & \cdots & w_x & \cdots & 0 & w_0 & 0 & 0 & 0 \\
0 & 0 & w_L & 0 & \cdots & w_x & \cdots & 0 & w_0 & 0 & 0 \\
 & & & \ddots & & & \ddots & & & \ddots & \\
0 & 0 & 0 & 0 & w_L & 0 & \cdots & w_x & \cdots & 0 & w_0 \\
 & & & & & \ddots & & & \ddots & & \\
0 & 0 & 0 & 0 & 0 & 0 & w_L & 0 & 0 & w_x & 0 \\
 & & & & & & & \ddots & & & \\
0 & 0 & 0 & 0 & 0 & 0 & 0 & 0 & w_L & 0 & 0 \\
 & & & & & & & & & \ddots & \\
0 & 0 & 0 & 0 & 0 & 0 & 0 & 0 & 0 & 0 & w_L
\end{bmatrix}\right\} N
$$

(where Δt labels the top three rows)

and X given by:

$$
(23)\qquad X \;=\; \begin{bmatrix}
0 \\ 0 \\ 0 \\ \vdots \\ 0 \\ v_m(0) \\ v_m(1) \\ v_m(2) \\ \vdots \\ v_m(n)
\end{bmatrix}
\begin{array}{l}
\left.\rule{0pt}{4.5em}\right\} L/\Delta x \\[0.3em]
\left.\rule{0pt}{4.5em}\right\} wl/\Delta x
\end{array}
$$

In **A**, x is the position of an electrode in the channel where one wishes to simulate the neural signal. As described previously, "L" and "wl" represent channel length and AP wavelength in millimeters, respectively. A minimum length interval, Δx, equal to 0.01 mm was used in all simulations and is the distance between adjacent columns in **A**. For each

AP waveform, this corresponded to a minimum time interval, Δt, equal to Δx divided by the AP's conduction velocity and is the time interval between adjacent rows in $\mathbf{A}$. Thus,

$$(24) \qquad \Delta x \quad = \quad 0.01 \text{ mm}$$

$$(25) \qquad \Delta t \quad = \quad \frac{\Delta x}{v}$$

In $\mathbf{A}$, w_0 and w_L are scaling constants that serve to weight the transmembrane voltages at the channel ends in accordance with Eq. 13. Their sum represents the linearization term, $e_m(x)$, at the x position of interest. The w_x weight is always -1 since the amplitude of the transmembrane potential, $v_m(x)$, always subtracts 100% of its value from the linearization term. The weighting terms at 0 and L are separated by $L/\Delta x$ columns in $\mathbf{A}$. For example, an 8 mm channel is represented in $\mathbf{A}$ with w_0 and w_L located 800 ($= 8$mm/0.01mm) columns apart. Similarly, for an electrode located at x=2 mm, w_x would be located 200 columns to the left of w_0. General expressions for computing weights corresponding to any position "x" are given by:

$$(26) \qquad w_0 \quad = \quad \frac{L - x}{L}$$

$$(27) \qquad w_L \quad = \quad \frac{x}{L}$$

$$(28) \qquad w_x \quad = \quad -1$$

The total number of columns in $\mathbf{A}$ equals the number of rows in X and is represented by N, the sum of the channel length and AP wavelength in simulation units. Thus,

$$(29) \qquad N = \frac{L + wl}{\Delta x}$$

In vector X, the AP's spatial profile is padded with a column of zeros equal in length to the channel length. This is to ensure that the first value in the "difference" reflects the instant just before the AP's rising phase enters the channel's left edge at x=0. For example, simulating the neural response for a 20 m/s AP with a wavelength of 10 mm (see Figure 4.1A) traveling through an 8 mm channel requires N = (1000+800)/0.01 = 1800, **A** to be an 1800 x 1800 square matrix and X to be an 1800 x 1 column vector. Their product yields an 1800 x 1 column Y vector with each element of Y reflecting the "difference" computed for an electrode located at "x" for instants in time 0.0005 ms (= 0.01mm/20 mm/ms) apart as the AP advances through the channel in 0.01 mm increments.

4.2.1.9 Model parameters

Table 4.1 provides a list of model parameters and their corresponding values and units. The conductivity of HBSS was assumed to equal that of physiological saline. Conductivities were assumed to remain constant over the range of temperatures observed during experimental recordings (36-39 °C).

Table 4.1 Model parameters

Table 4.1 Model parameters

conductivity of axoplasm[1]	σ_a	1/90	$(\Omega\text{cm})^{-1}$
conductivity of neural tissue[1]	σ_n	1/163	$(\Omega\text{cm})^{-1}$
conductivity of HBSS	σ_s	1/65	$(\Omega\text{cm})^{-1}$
fiber diameter (myelin sheath O.D.)	a'	Eq. 14	μm
axonal diameter	a	Eq. 15	μm
g-ratio (axon : fiber diameter)	g	0.7	–
rootlet diameter	d	variable	μm
channel I.D.	b	200	μm
channel length	L	8	mm
AP conduction velocity	v	variable	m/s
peak AP amplitude	V_p	120	mV
bandwidth of recorded signals	B	10,000	Hz
Boltzmann's constant	k_B	$1.38\text{x}10^{-23}$	J/°K
electrode/HBSS impedance[2]	R_0	10,000	Ω

[1]longitudinal direction; [2]measured using a 1000 Hz sinusoidal signal

4.2.2 Experimental design

4.2.2.1 Overview

Fine nerve filaments (i.e. "teased rootlets") were teased from dorsal lumbar roots in rats. These were drawn through a 200 μm x 8 mm microchannel containing 5 electrodes that rested in a bath of Hanks balanced salt solution (HBSS). Using pipette stimulators positioned on the portions of rootlet protruding from each end of the channel, right- and left-bound action potentials were elicited and recorded. Recorded neural signals were compared to signals predicted by term 1 in Eq. 7. Stimulus pulses served as a source of external noise artifacts and the distribution of these at each recording site was compared to the linear distribution predicted by term 2 in Eq. 7. We explored different reference configurations for canceling external noise artifacts at each electrode. Background noise

levels – i.e. signals recorded at each electrode in the absence of stimulus pulses and neural signals – were measured and compared to the Johnson noise model to determine the degree to which thermal agitation of conductive species in a microchannel could be used to explain and predict these noise levels.

4.2.2.2 Microchannel

Chapter 3 describes the microchannels used for recording neural signals. Briefly, they were made using PDMS and were 8 mm long with inner diameters of 200 µm. They contained 5 Ag/AgCl circular electrodes with inner diameters of 150 µm located 1, 2, 4, 6, and 7 mm from the channel's end. Electrodes at 2 and 6 mm represented optimal offset locations where the largest signals were expected and the one at 4 mm was located at mid-channel.

4.2.2.3 Surgical Preparation

Adult Sprague-Dawley rats weighing between 350-500 g were anesthetized with 5% isoflurane and gravity perfused with 300-400 mL of ice-cold (0 °C) HBSS (HyClone, UT) for approximately 15 minutes. A section of the spinal column from T12-C1 was removed and placed in a bath of ice-cold HBSS where the dorsal lamina was removed using a set of fine-tipped rongeurs (Fine Science Tools, CA) to expose the spinal cord and associated dorsal roots. This process took between 1 to 1½ hours during which time the temperature of the bath and tissue were permitted to reach a room temperature of between 21-22 °C. A rootlet was cut from its native environment only when needed; otherwise the saline bath containing the spinal cord and associated structures was stored in a refrigerator at 4 °C between rootlet extractions.

Table 4.2 summarizes all 10 *in vitro* experiments performed. The bold rectangle highlights the experiments (Rats 58 and 59) which provided the data presented in this Chapter. The first 6 experiments were done using a different protocol provided by Gribi as summarized in (Gribi et al., 2018). Two experiments (Rats 50 and 51) used microchannels having different lengths and electrode configurations than the 200 μm ID x 8 mm long channel eventually developed, as described in Chapter 3. Data from these experiments were, therefore, not included in the analysis presented here. Two rats (Rats 52 and 54) died before rootlets could be extracted for recording purposes.

Neural activity was recorded in the remaining six experiments (Rats 53 and 55-59). However, many trials did not reflect neural activity in a single continuous axon running through the channel. For example, only 9 trials out of 92 total recordings obtained for Rats 53 and 55-57 showed clear signs of being due to neural conduction occurring in a single continuous axon. Most of the time, as discussed in Chapter 3, we observed compound action potential activity in discontinuous axons likely torn during the teasing process and which produced artificially elevated signals at the electrode or two electrodes nearest one end of the channel, closest to the stimulus site. Over the course of many trials, we learned to distinguish this distorted compound activity from viable single-unit activity occurring in an intact continuous axon. The latter was characterized by an all-or-none response elicited at a precise stimulation current that produced a signal nearly instantaneously at all five electrodes. The final two experiments (Rats 58 and 59) contained the majority of trials where viable single-unit activity was observed (highlighted by the bold rectangle in Table 4.2). While all trials were analyzed, a representative set of 12 trials, six from Rat 58 and

six from Rat 59, characterizing single-units traveling in different directions at different speeds were selected and presented here. Table 4.3, in the Results section, provides details of the 12 recordings presented in this dissertation.

Table 4.2 Summary of all *in vitro* experiments

Table 4.2 Summary of all *in vitro* experiments

Protocol	Rat #	Description		
		# rootlets w/ viable axons	# trials	# trials with clear single-unit (SU) activity
rats anesthetized (0.5-1% isoflurane); rootlets teased in Hibernate A[1]	50	channel length > 8 mm; diff. electrode arrangement		
	51	"		
	52 (died)			
	53	4	36	mainly CAPs
	54 (died)			
	55	2	23	mainly CAPs
rats perfused with cold HBSS (1-4 °C); rootlets teased in HBSS[2]	56	4	10	3
	57	4	23	6
	58	11	40	19
	59	15	61	22

[1] from Gribi et al (2018), [2] from FitzGerald et al (2009)

4.2.2.4 Rootlets

Naturally-occurring rootlets isolated from left and right dorsal L4-L6 roots were used in recording experiments. Rootlets were extracted using small surgical scissors to cut a rootlet near its attachment point to the spinal cord, as close to the dorsal root entrance zone (DREZ) as possible, and at the other end as close as possible to where it merged with its dorsal root ganglia (DRG). Extracted rootlets were between 25-30 mm long and were immediately placed in the petri dish containing the microchannel and teased apart to obtain

nerve strands that could be pulled through the microchannel. Rootlets were teased apart

using two sets of fine forceps (Fine Science Tools, CA) to grab one end of the rootlet which

was then slowly bisecting by moving the forceps in opposite directions. During this

motion, the strands being tugged apart were perpendicular to the intact portion of the rootlet

which became progressively shorter as the splitting process was continued. It was

necessary to repeat the splitting process a number of times to produce teased strands

sufficiently small to fit inside the 200 µm I.D. channel. A short piece (15 mm) of 8-0 suture

was tied to one end of a teased rootlet and the free end was then threaded through the

channel which, in turn, caused the rootlet to be pulled through the channel as well.

4.2.2.5 Recording setup

Microchannels were lowered into a glass HBSS-filled petri dish (3" diameter) placed inside

of a larger petri dish (5" diameter) placed on top of an aluminum block (1"x12"x18") which

was heated using two thermo-resistive electric heating pads (i.e. back warmers) that were

thermostatically controlled (Inkbird, Shenzhen, China) to maintain bath temperatures

between 37-39 °C. A small pump was used to circulate water in the larger petri dish that

was heated a few degrees above 37 °C to help maintain HBSS bath temperatures near to

37 °C. A 5 ml syringe filled with warm HBSS and having a bent 30-gauge needle with its

sharp point ground smooth was used to flush any air bubbles and tissue remnants from the

channel prior to rootlet insertion. This was done periodically as needed. Electrode

impedances were checked periodically throughout the recording session and found to

remain constant at 10,000 Ω as described previously.

4.2.2.6 Reference terminal and grounding

A circular coil of bare Ag/AgCl wire placed in the bath behind the microchannel served as a reference terminal for all electrodes. This had been made in a similar fashion to the electrode wires and had a DB-9 pin crimped to the non-coiled end that was plugged into one of the pin receptacles on the DB-25 adapter in the electrode assembly. The negative inputs of the electrodes to their respective amplifiers were shorted together using jumper wires between their screw terminals and connected to the screw terminal associated with the reference coil.

The aluminum plate was grounded to a copper ground plate in the lab using a woven steel cable. An insulated wire with alligator clips at each end was used to connect exposed metal surfaces associated with the screw terminal breakout board and DB-25 connectors to the grounded aluminum plate.

4.2.2.7 Stimulation

Suction electrodes (A-M Systems, WA) attached to micromanipulators were positioned near the portions of the rootlet protruding from either ends of the channel and a slight negative pressure was used to draw the surface of the nerve to the tip of the glass pipette attached to the suction electrode. Pipette tips were approximately 80 μm in diameter. Cathodic first, bi-phasic square-wave 25 μs per phase current pulses were delivered to the rootlet's surface (Model 2100 Isolated Pulse Stimulator, A-M Systems, WA) and used to elicit action potentials on either side of the nerve. The timing of stimulation pulses was determined by the TTL output from a wave generator and caused stimulus pulses to be delivered at rates between 5-20 times per second. Signals at each electrode were monitored

in real-time on an oscilloscope (Tektronix, Inc., OR) while stimulus amplitudes, initially set to zero, were incrementally increased until a neural signal appeared nearly simultaneously on all electrodes. Stimulus amplitudes were then slightly lowered to find the minimum current required to elicit an all-or-none signal characteristic of action potentials. Stimulus amplitudes ranged between 0.7-3.1 µA with a mean of 1.6 µA.

4.2.2.8 Signal processing

Neural signals were amplified (x 10,000) and band-pass and notch filtered to remove low, high and any line frequencies using a pass-band of 10-20,000 Hz (2nd order Butterworth) and a notch frequency of 60 Hz. Analog signals were sampled at 100,000 Hz (National Instruments, TX) and recorded by a computer running a LabView-based real-time data acquisition module. Typical recordings were 10-15 seconds in duration. Signals were additionally filtered offline using a 2nd order Butterworth filter with cutoff frequencies of 100-10,000 Hz prior to analysis.

4.3 Results

4.3.1 Theoretical predictions

4.3.1.1 Signal enhancement at offset electrodes
Largest signals occur offset from mid-channel in the direction of AP propagation
Figure 4.4 shows the extraneural signals recorded at electrodes positioned at 2, 4 and 6 mm for 15 m/s triangular and realistic APs traveling to the right through an 8 mm long channel. Compared to peak amplitudes at mid-channel (marked "b" in C and D), signals are

enhanced at offset locations 2 mm to the right of center (marked "c"). The degree of signal

enhancement for triangular waveforms is seen to be larger than for realistic ones.
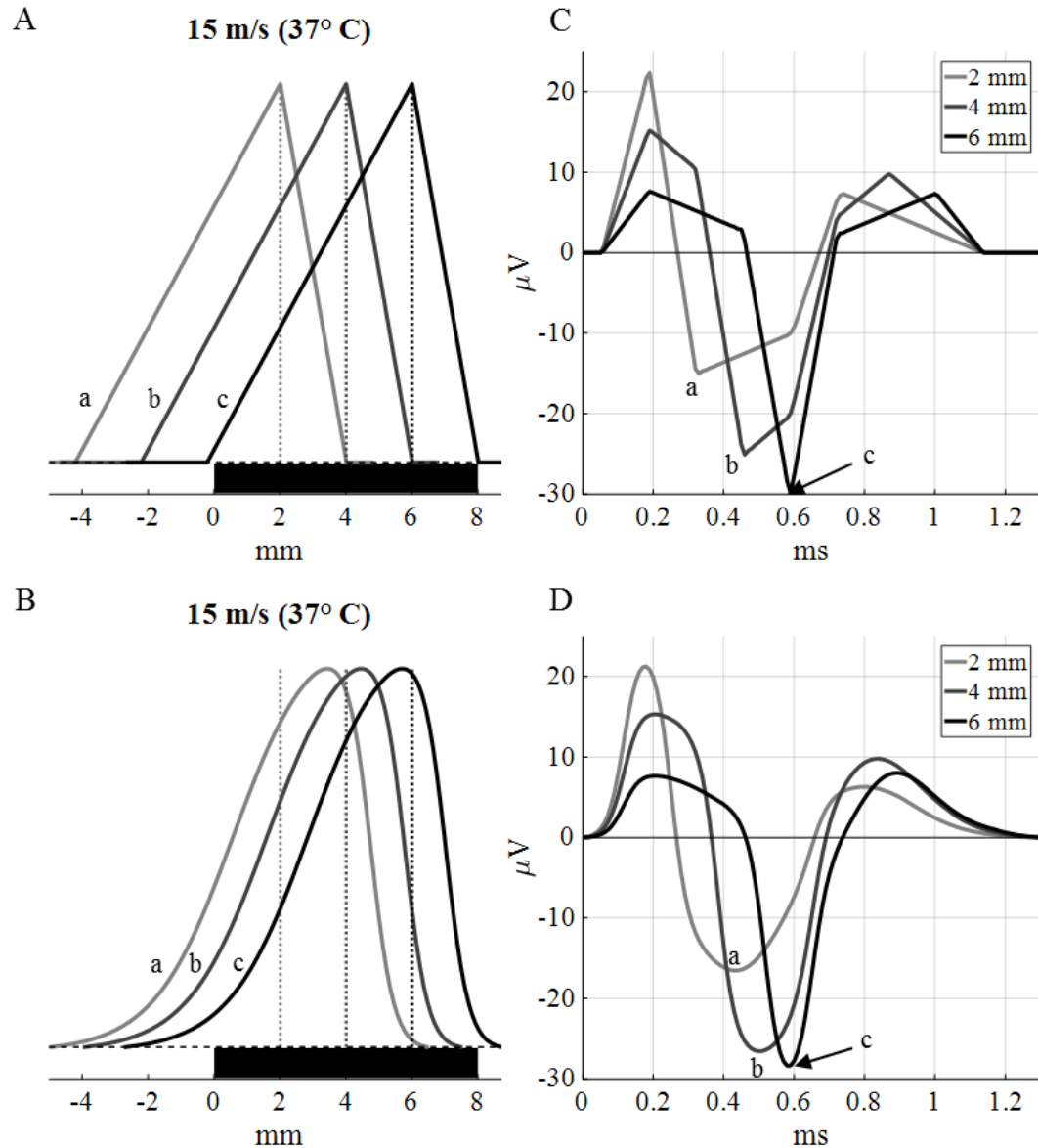
Figure 4.4 Simulated neural recordings. A) Triangular and B) realistic AP profiles traveling to the right at 15 m/s through a 200 µm ID x 8 mm long channel (thick black bars). Extraneural signals are shown in (C) and (D) and were computed at three electrode locations: mid-channel (4 mm) and two locations offset 2 mm to the left and right of mid-channel. Dotted vertical lines highlight electrode locations. AP profiles having different degrees of shading in (A) and (B) show their positions in the channel when signal amplitudes are greatest (i.e. have their most negative values) at each electrode. For

example, the darkest waveform, labeled "c" in (A) and (C), shows the position of the AP when the negative peak in (C) and (D) for the electrode at 6 mm is largest, also marked "c" in (C) and (D). AP waveforms and negative peaks labeled "a" and "b" show these relationships for electrodes at 2 mm and mid-channel, respectively.

APs are depicted at the moment they generate the largest signal at each of the three electrodes. For triangular APs, the largest negative peak in the recorded signal occurs at the moment the APs peak coincides with the electrode (Figure 4.4 A). This is not the case for the realistic waveform. The alignment of the realistic AP with each electrode when the largest signal is produced changes from electrode to electrode (Figure 4.4 B). If APs were triangular in shape, time delays between the occurrence of negative peaks in the neural recordings could be divided into the distance between electrodes to obtain a reasonable estimate of the AP's speed. In reality, peaks in the recorded neural signal do not necessarily correlate to the moment when the AP peak is passing an electrode. Therefore, time delays between negative peaks do not provide a reliable measure of the transit time between electrodes and any presumption that they do leads to erroneous conduction velocity estimates. For example, the negative peaks in D are more closely spaced in time than in C which may give the false impression that the transit time between electrodes is shorter and that the realistic AP is traveling faster than its actual speed of 15 m/s.

Offset electrodes provide signal enhancement over a wide range of conduction velocities
Figure 4.5 shows negative peak amplitude profiles for triangular and realistic action potentials traveling to the right through a 200µm ID x 8mm long microchannel. Circles and bold lines between circles highlight where signal amplitudes are maximum. This occurs to the right of mid-channel for triangular APs having speeds of between 5-40 m/s. For speeds less than or equal to about 5 m/s and greater than 40 m/s, the mid-channel

position would record the largest signal. Offset electrode locations are predicted to always record larger signals for realistic APs over the range of speeds depicted.
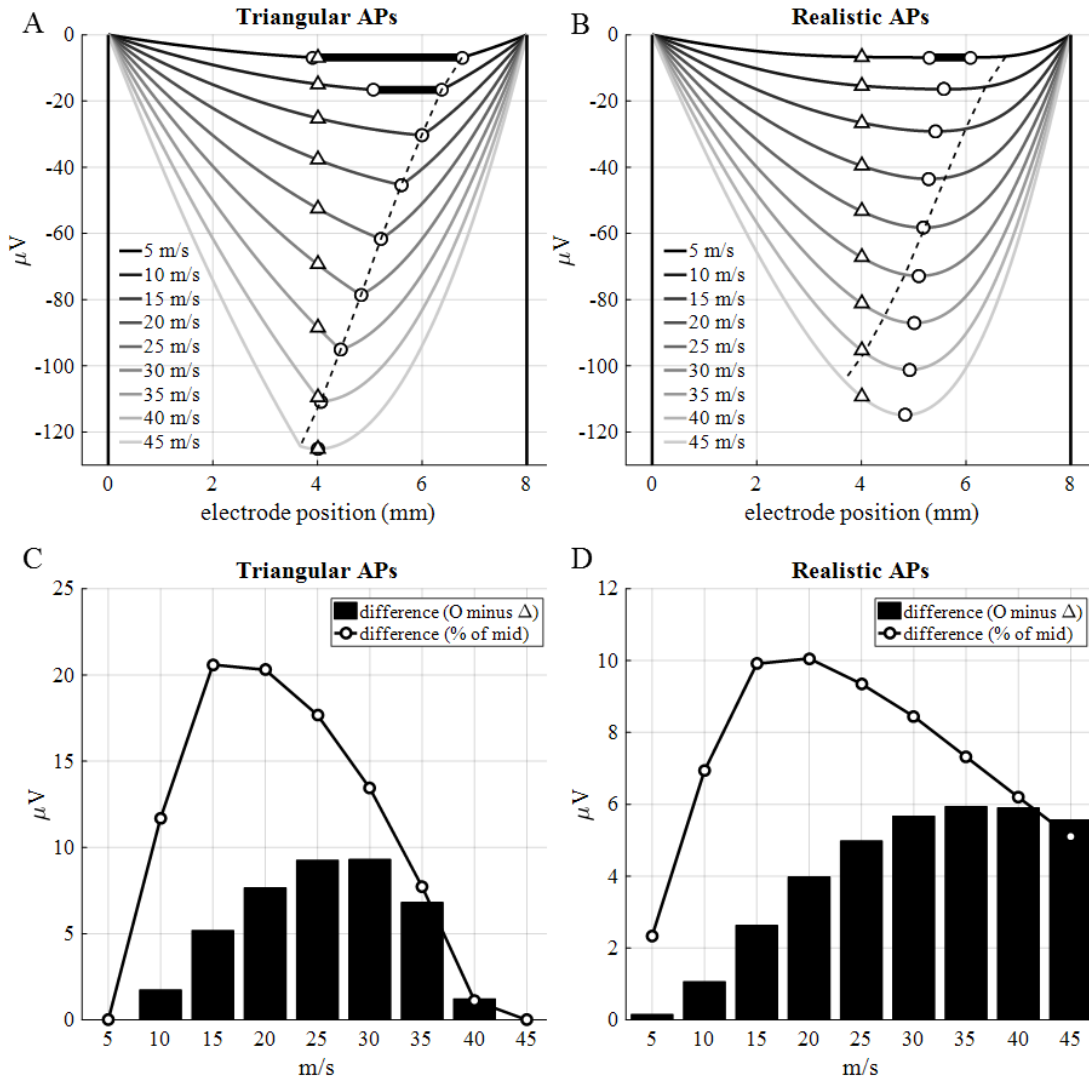
Figure 4.5 Peak amplitudes and optimal electrode locations for right-bound APs traveling at different speeds. APs travel to the right through a 200μm ID x 8mm L channel at 37 °C. Largest negative peak signal amplitudes are shown for (A) triangular and (C) realistic AP waveforms at all locations in the channel: circles (O) mark locations where signals are maximum in the channel and circles with solid bars between them (O—O) denote ranges of locations where signals are maximum (i.e. 5 and 10 m/s APs in A and 5 m/s AP in B). Triangles (Δ) highlight signal amplitudes at mid-channel, black vertical lines at 0 and 8 mm denote the channel edges, and the dashed line (---) indicates a distance of one rising phase length in from the right edge of the channel. Absolute amplitude differences (bars) between signals at optimal electrode locations and those at mid-channel

for (B) triangular and (D) realistic APs having the speeds shown in (A) and (C). Differences are also expressed as a percentage of the signal amplitudes at mid-channel (solid lines with O markers). Rootlets assumed to entirely fill the channel cross section (i.e. d = 200 µm).

The dashed lines in the figure represent a distance of one rising phase from the right end of the channel. As expected from Figure 3.1, this is the optimal electrode placement for all triangular waveforms except when this distance becomes greater than half the channel length (Figure 3.1 A). This is seen to be the case for the 45 m/s AP where the optimal position is at mid-channel and not at the location indicated by the dashed-line. The lack of overlap between the dashed line and circles in Figure 3.1 suggests rising phase distances from the channel end are not good predictors of optimal electrode positions for most realistic AP waveforms.

Channels shorter and longer than 8 mm exhibit similar trends (not shown), with offset electrodes predicted to record maximum signals albeit over different ranges of conduction velocities. A good rule of thumb is to design channels having lengths equal to the wavelength of a "target AP." Signal enhancements at an offset electrode will be more pronounced around the target speed, since this speed represents a transition from a situation where multiple locations inside the channel record the largest signals to those where only one location is optimal. The 8 mm channel depicted in Figure 4.5 targets AP speeds of around 15 m/s (14.26 m/s exactly), which have a wavelength of about 8 mm, and a single offset electrode at 6 mm is optimal for triangular APs (Figure 4.5 A). For slower APs (i.e. those having speeds of 5 and 10 m/s) an electrode positioned anywhere between 5-6.5 mm would be equally optimal.

Signals at optimal offset locations are between 10-20% larger than those at mid-channel

Offset electrodes are projected to record larger signals for both AP waveform shapes (Figure 4.5 C, D). Signal amplitudes at optimal offset locations are expected to be up to about 10 µV larger for triangular waveforms, a difference that is about 20% of the amplitude at mid-channel. Signal differences are less for realistic APs, with optimal offset locations expected to exceed mid-channel amplitudes by up to about 5 µV, an increase of about 10% of the signal at mid-channel. This theoretical analysis predicts a 10-20% increase in signal amplitudes at offset electrodes compared to those recorded at mid-channel with the degree of enhancement depending on how close in shape actual AP waveforms are to simulated triangular or realistic waveforms.

4.3.1.2 Signal discrimination at offset electrodes

Offset electrodes record dissimilar signals for APs traveling in opposite directions

An inherent property of offset electrodes is that they record different signals for APs traveling in opposite directions. At a given offset electrode, APs traveling in opposite directions produce signals having different shapes and different negative peak amplitudes, features which can be used to differentiate between them. This phenomenon is demonstrated over a range of conduction speeds (5-45 m/s) in Figure 4.6 A and B, where the peak signal profiles for right-bound APs are shown in black lines and those traveling to the left are shown in gray. Amplitude profiles intersect at mid-channel (triangles) whereas they are different at offset electrode locations, particularly at O and X locations. Os have the same meaning as in Figure 4.5 and highlight positions where signals are maximum and Xs highlight locations where the differences between signal amplitudes for

right- and left-bound APs are maximum.   Amplitude differences at these locations are

shown for a 35 m/s AP traveling in opposite directions (vertical bars in Figure 4.5 A and

B) with those at the X location clearly exceeding those at O for both triangular and realistic

waveforms.
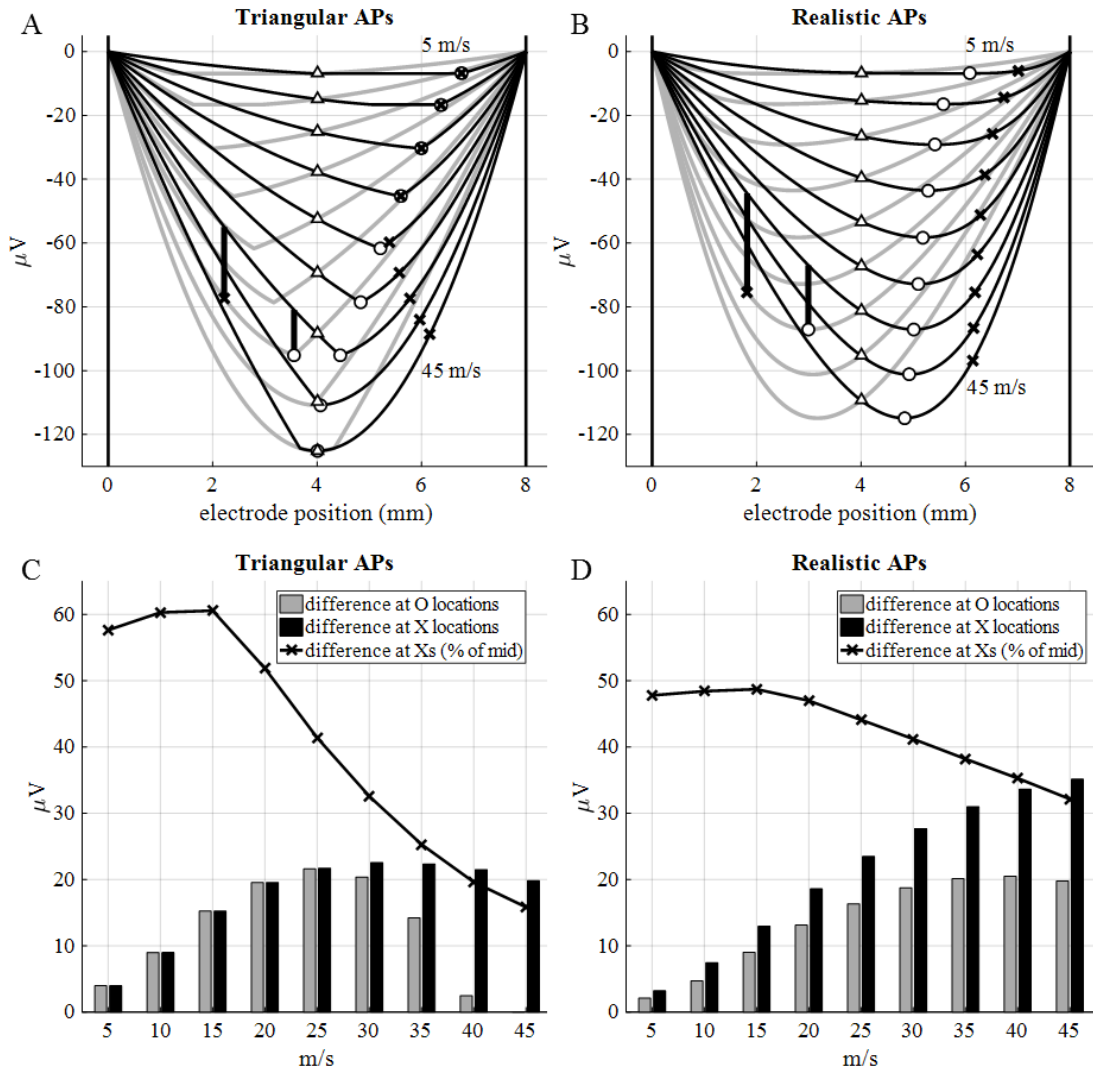
Figure 4.6 Optimal offset locations to maximize amplitude differences for APs traveling in opposite directions. A, C) Triangular are compared to B, D) realistic APs traveling in opposite directions. Dark lines, circles (O) and triangles (Δ) are the same as in Figure 4.5, while shaded lines indicate signal amplitudes for left-bound APs and exes (X) indicate locations where differences in signal amplitudes for right- and left-bound APs having identical speeds would be greatest. Vertical bars show signal differences between a left- and right-bound AP traveling at 35 m/s, with differences being greater at the X

location compared to the one at O. (C) and (D) compare amplitude differences between left- and right-bound APs at O and X locations, with lines expressing amplitude difference at X locations as a percentage of signal amplitudes at mid-channel. Conduction velocities range from 5-45 m/s in steps of 5 m/s. Channel dimensions are 200 µm ID x 8 mm long and T = 37 °C for these simulations. Rootlets assumed to entirely fill the channel cross section (i.e. d = 200 µm).

The magnitudes of these signal differences at these locations are substantial with differences of over 20 and 30 µV expected at X locations for triangular and realistic waveforms, respectively, over the range of velocities shown (Figure 3. C and D). These differences represent between 30-50% of the mid-channel amplitudes for realistic waveforms and as much as 60% for triangular waveforms. Amplitude differences at X locations are larger than O locations for all the realistic APs and for triangular APs with speeds over 20 m/s.

X locations provide enhanced discriminating ability compared to O locations for preferentially detecting APs traveling in a specific direction over the range of conduction velocities shown. For triangular APs with speeds exceeding about 25 m/s, amplitude differences at O locations are seen to steadily decline and vanish to zero while remaining relatively constant at around 20 µV at X locations. For realistic APs with speeds exceeding 25 m/s, amplitude differences at O remain between 15-18 µV, whereas they increase from about 20-30 µV at X locations over this same range of conduction speeds (25-45 m/s).

Except for a few triangular APs, in general, locations that maximize signal amplitudes (O) for APs traveling in a given direction are not those that maximize signal differences between APs traveling in opposite directions (X). Locations that are optimal for recording the largest signals (Os) tend to migrate towards mid-channel at higher conduction

velocities, while those that maximize signal differences between APs traveling in opposite directions (X) tend to remain closer to the channel ends. This trend is particularly apparent for triangular waveforms where Os and mid-channel positions (Δs) eventually overlap at 45 m/s whereas X locations, which overlap with O locations up to speeds of 20 m/s, shift away from mid-channel and migrate towards the right end of the channel at higher speeds. O and X locations never overlap for realistic waveforms and while there is a widening gap between O and X positions at higher velocities, the degree of divergence is less than for triangular waveforms. An offset electrode located at approximately 5 mm appears optimally situated for recording the largest signals for a majority of the realistic right-bound APs and a position of about 6 mm appears optimal for maximizing signal differences between right- and left-bound APs over a wide range of conduction velocities.

Offset electrode preferentially detect signals traveling in preferred directions

Amplitude differences in the signals recorded for APs traveling in opposite directions suggests a single offset electrode situated nearer one end of the channel is inherently well-suited for preferentially detecting APs traveling towards that end. For example, if a detection threshold -60 μV was used, an offset electrode positioned at 6 mm could be used to record APs traveling to the right at speeds of between 30-45 m/s without ever recording any of those to the left. At the same detection threshold, an offset electrode also positioned at 2 mm could be used to detect only left-bound APs in this speed range, since none of the right-bound AP amplitudes exceed -60 μV at this position. Thus, a pair of offset electrodes could presumably be used to discriminate between APs traveling in opposite directions in nerves containing both afferent and efferent fiber types.

77

4.3.2 Recorded signals

4.3.2.1 Overview

Figure 4.7 shows the experimental setup for recording neural signals *in vitro*. Suction electrode stimulators were labeled "left" and "right" (Figure 4.7 A) and are shown attached to the left and right ends of a rootlet protruding from the ends of the channel (labeled "P" in Figure 4.7 D). Teased rootlets shown (Figure 4.7 C) were obtained by repeatedly bisecting natural roots and rootlets (Figure 4.7 D).
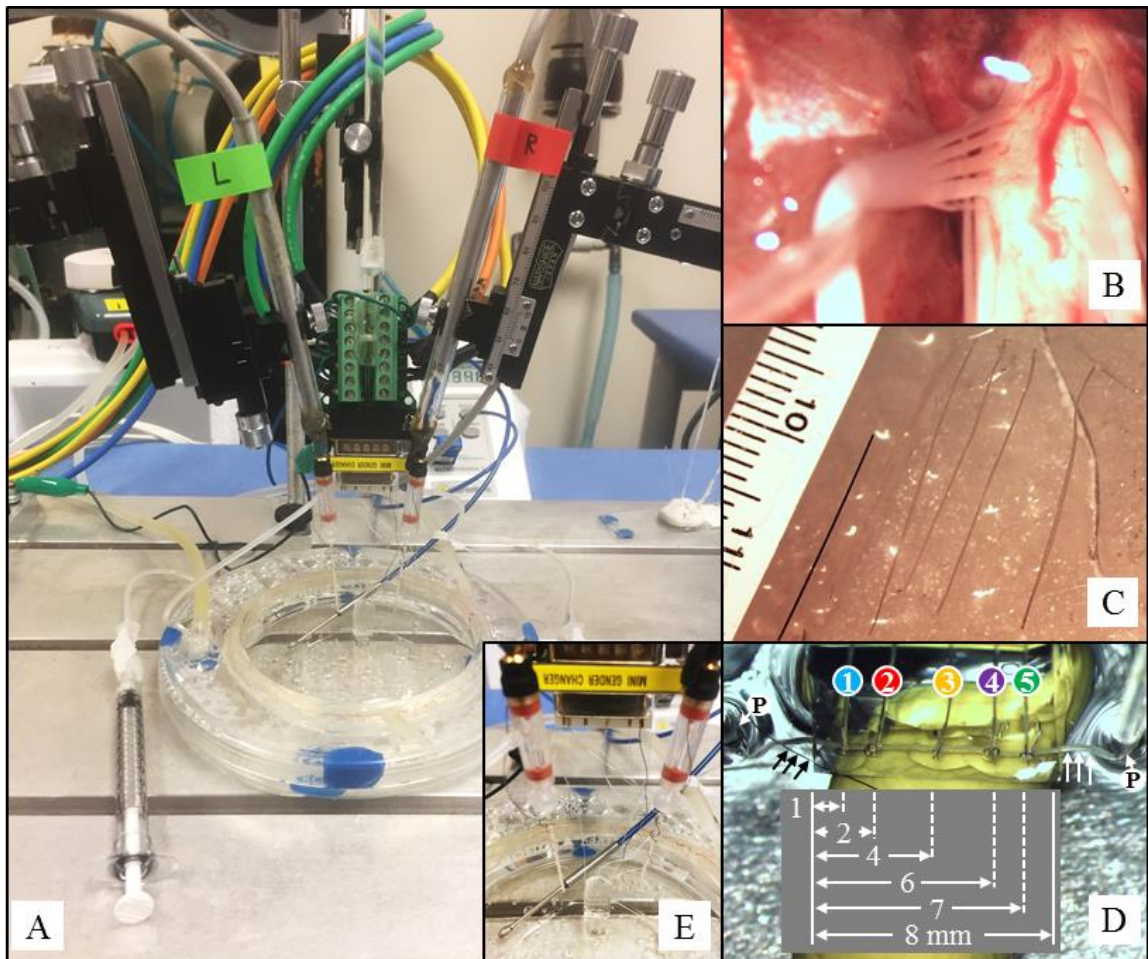
Figure 4.7 Experimental setup. A) Microchannel submerged in a temperature-controlled HBSS bath with left and right suction electrodes (labeled "L" and "R") for stimulating

rootlets. Colored cables plugged into the screw terminal of the breakout board routed signals to a bank of A-M Systems Model 1700 amplifiers (see text). Inset (E) shows the PDMS block containing the microchannel in greater detail. Pipette tips, electrode wires with crimped gold-plated pins plugged into the DB-25 adapter and a submerged temperature probe resting in the bath in the background are visible. B) Naturally-occurring rootlets were removed and C) repeatedly bisected to create progressively smaller nerve strands or "teased rootlets". D) A suture (3 black arrows) tied to one end was used to thread a rootlet (3 white arrows) through the channel which was 200 µm I.D. x 8 mm long containing electrodes 1-5 with spacings of 1, 2, 4, 6 and 7 mm from the left end of the channel. Suction electrodes were used to create a seal between pipette tips (labeled "P") and the surface of the rootlet to concentrate stimulus currents and cause action potentials to travel right or left through the channel.

Rootlets were dissected from different dorsal lumbar roots. Stimulus amplitudes and bath temperatures were carefully monitored and recorded. Table 4.3 provides details of the recording sessions presented here.`

Table 4.3 Recording details

Table 4.3 Recording details

Rat #	Rec #	Stim. side	Trial name	Dorsal root	Teased rootlet #	Stim. amplitude (µA)	Temp. (°C)
58	10	R	58.10.Rstim	left L5	6	1.2	37.6
	20	R	58.20.Rstim	left L5	8	3.1	36.5
	26	L	58.26.Lstim	left L5	9	1.1	38.6
	31	R	58.31.Rstim	right L5	1	1.5	38.9
	32	L	58.32.Lstim	right L5	1	3.0	38.9
	40	L	58.40.Lstim	right L5	5	0.9	37.4
59	9	L	59.9.Lstim	right L6	3b	1.2	37.4
	12	R	59.12.Rstim	right L6	3b	0.7	37.5
	15	L	59.15.Lstim	right L6	4a	2.2	37.1
	18	R	59.18.Rstim	right L6	4b	1.0	37.6
	32	R	59.32.Rstim	right L6	5	1.2	38.2
	44	L	59.44.Lstim	right L6	8a	1.6	37.6

Note: brackets ("[") indicate recordings obtained from the same teased rootlet

4.3.2.2 Offset electrodes record larger signals than those at mid-channel

Figure 4.8 shows the raw signals at different time scales typically recorded for rootlets stimulated on the left (A-E) and right (F-J). Signals on all channels are shown including the TTL square wave for triggering stimulus pulses (labeled "stim") and the neural signals at each electrode (labeled "1"-"5"). The middle-row of plots shows signals in (A) arriving first at electrode 1 and propagating to the right towards 5 while those in (F) arrive first at electrode 5 and travel to the left towards 1. The lower set of plots shows these signals superimposed on each other. Electrode 4, offset 2 mm to the right of mid-channel, records the largest signal for right-bound APs, as predicted. This pattern is reversed for left-bound APs, where the largest signals occur at electrode 2, offset 2 mm to the left of mid-channel. Note, the first negative phase, marked "s", is the signal from stimulus artifact. Neural signals, labeled 1-5 for right-bound and 5-1 for left-bound APs, follow afterwards.
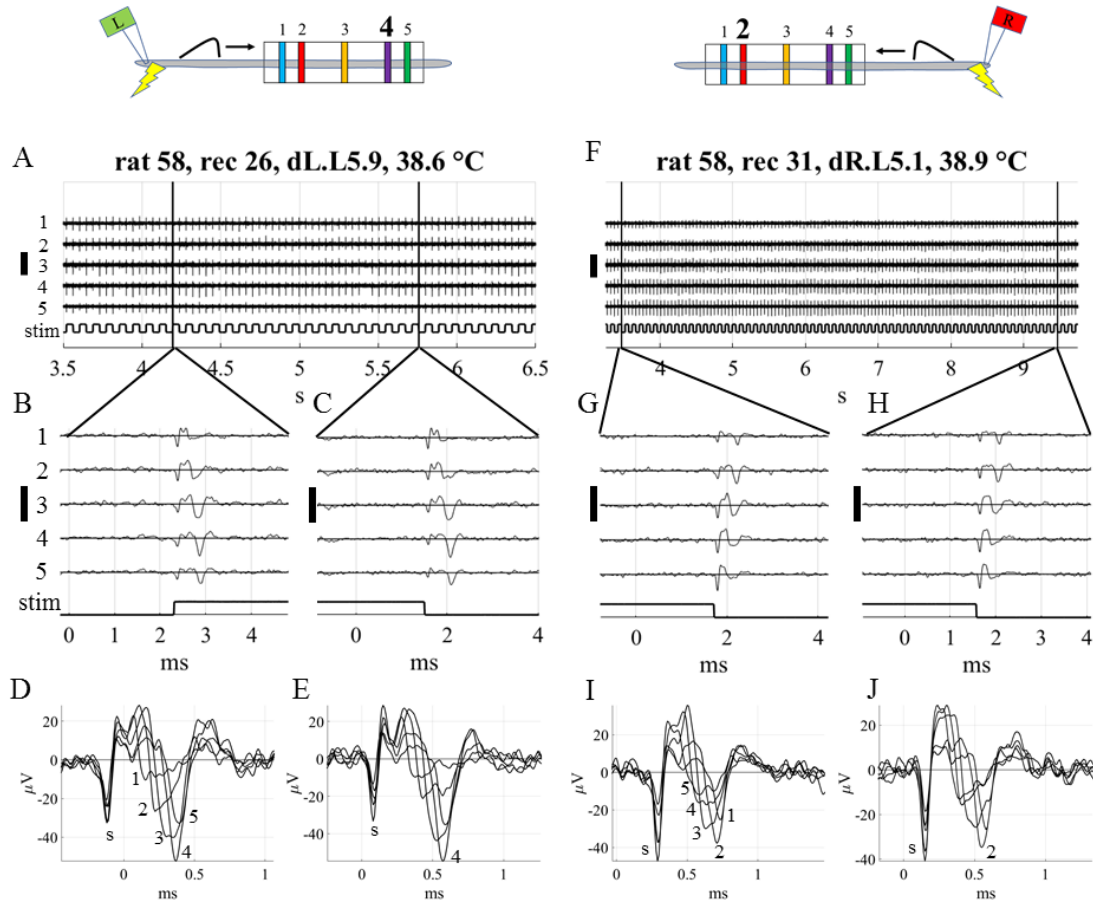
Figure 4.8 Optimal offset electrodes record the largest signals for right- and left-bound action potentials. (A) 3 seconds of raw signals recorded at each electrode when stimulating a teased left dorsal L5 rootlet on the left producing a SUAP traveling through the channel to the right. Signals at electrode 1 appear in the top-most trace with those at 2, 3, 4 and 5 shown labeled on separate lines below. Stimulation pulses were delivered at up- and down-strokes of the square wave trigger pulse, shown in the lower trace in the raw recordings and labeled "stim". Signals at each electrode are shown in greater detail at two different time points (B, C) over a 4 ms time window with recordings at each electrode labeled 1-5. Signals arrive at electrode 1 first and 5 last. (D, E) Signals at each time point are plotted overlapping each other with the peak responses at each electrode labeled 1-5 and stimulus artifacts labeled with an "s". (F) A right dorsal L5 rootlet from the same rat was stimulated on the right side of the channel producing a SUAP traveling to the left. (G, H) Signals arrive at electrode 5 first and 1 last. As predicted, electrode 2 at 2 mm is seen to have the largest signals at each of the time points shown (I, J). Vertical scale bars denote amplitudes of $100\,\mu V$. Signals in (A-E) were recorded at 38.6 °C and those in (F-J) at 38.9 °C. Schematics at the top of the figure show the experimental setup used to obtain the signals in the plots below.

Figure 4.9 shows all the neural responses recorded by each electrode for each trial. Signals were aligned to trigger pulses and superimposed on each other with those in (A) reflecting responses when rootlets were stimulated on the left and, in (B), when they were stimulated on the right. Overlapping white lines indicate the mean signal at each electrode. From the moment APs enter the channel at electrodes 1 or 5, depending on their direction, signal amplitudes rise steadily in the direction of AP propagation and, as above, peak at offset locations 2 mm to the right and left of mid-channel, after which they decline as they approach the channel exit. These patterns become more apparent with increasing AP velocities and can be appreciated by comparing the uppermost plots where APs were slowest to those lower down where APs have increasingly faster speeds (i.e. negative peaks become more closely spaced as one moves from top to bottom in the figure).

Statistically, negative peak amplitudes at offset electrodes 4 (at 6 mm) and 2 (at 2 mm) were, for the most part, slightly larger than those at mid-channel for action potentials that traveled to the right and left, respectively. Table 4.4 lists the p-values and 95% confidence intervals obtained when a paired t-test was used to compare differences between the mean negative peak amplitudes at mid-channel and those at optimal offset locations for the six left-stim and six right-stim trials. As in Figure 4.8, trials in each stimulation category are listed in order of increasing AP conduction velocity. For nearly all trails, the mean amplitudes were significantly different at the $\alpha=0.05$ level, with those associated with faster action potentials showing the greatest differences. There were two exceptions. One trial (59.15.Lstim) showed differences but not at a p-value that met the significance threshold (i.e. $p = 0.073$). Another trial (59.18.Rstim) showed the signals at mid-channel

to be slightly larger than those recorded at electrode 2. Offset electrodes had larger negative peak amplitudes than those at mid-channel for the remaining trials. The confidence intervals indicate the extent to which negative peak amplitudes at optimal electrode locations would be expected to be more negative than those at mid-channel.

Table 4.4 Optimal offset vs mid-channel negative peak amplitudes

Table 4.4 Optimal offset vs mid-channel negative peak amplitudes

Trial name	n	electrodes compared	p-value[1]	95% confidence interval (µV)	
				lower bound	upper bound
59.15.Lstim	148		7.30E-02	-0.82	0.04
58.32.Lstim	130		1.35E-11 *	-3.02	-1.75
59.44.Lstim	282	4 (opt) vs 3 (mid)	4.58E-02 *	-0.80	-0.01
58.40.Lstim	77		2.24E-14 *	-5.24	-3.41
59.9.Lstim	195		1.85E-07 *	-2.05	-0.96
58.26.Lstim	163		1.17E-14 *	-3.47	-2.16
58.20.Rstim	182		3.25E-02 *	-1.09	-0.05
59.18.Rstim[†]	188		3.65E-02 *	0.03	0.97
59.32.Rstim	356	2 (opt) vs 3 (mid)	9.63E-03 *	-0.97	-0.14
58.10.Rstim	59		1.25E-03 *	-3.36	-0.87
59.12.Rstim	164		9.36E-07 *	-2.16	-0.95
58.31.Rstim	147		6.99E-15 *	-3.48	-2.19

*sig. (α=0.05), [1]two-tailed paired t-test; [†]mid > opt
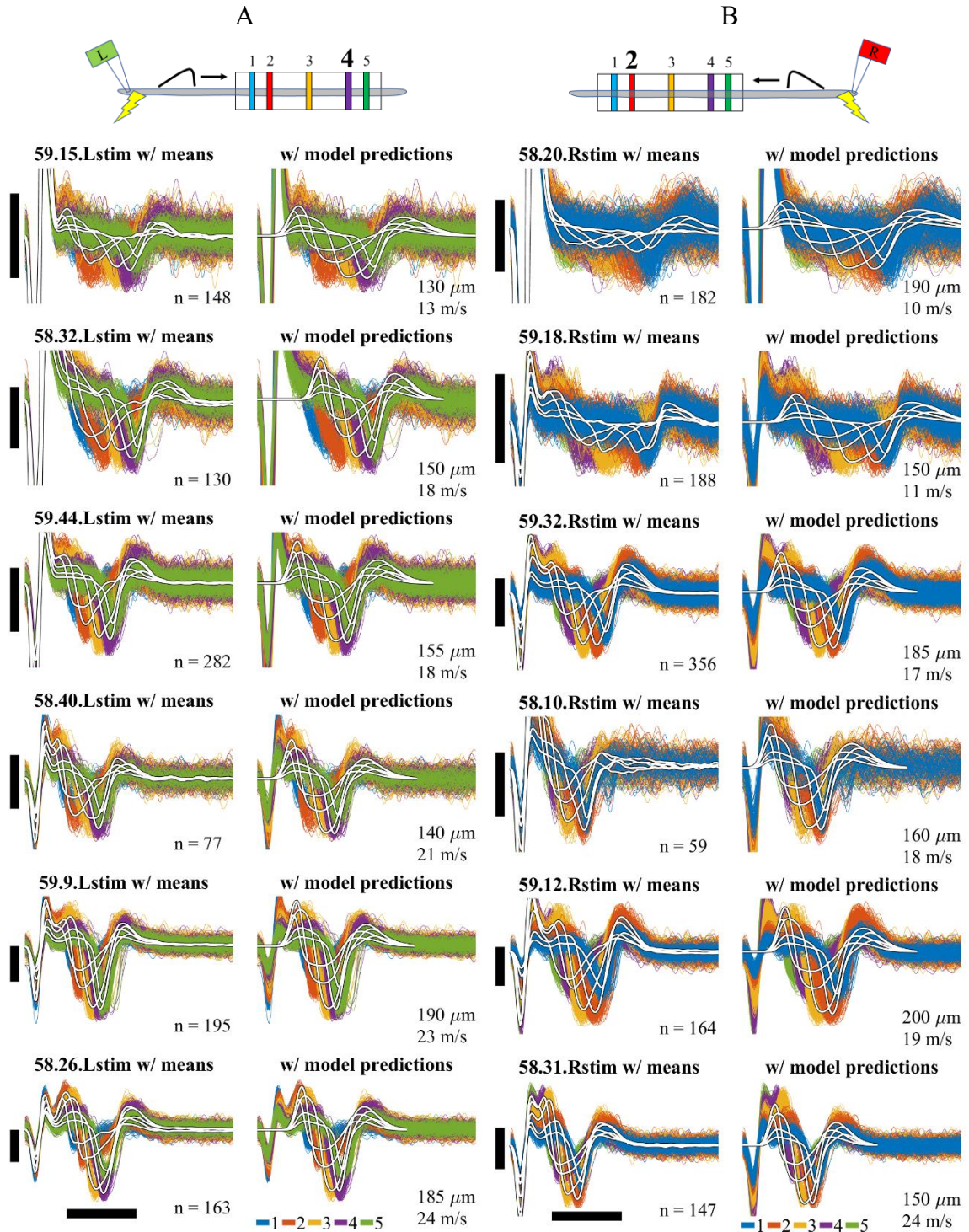
Figure 4.9 Mathematical model predicts recorded signals. Signal means and model predictions (white lines) are shown overlapping the raw signals that are temporally aligned to stimulus trigger pulses and superimposed on one another. Recordings at electrodes 1, 2, 3, 4, and 5 are shown in blue, red, yellow, purple, and green, respectively, also displayed schematically above the plots. As predicted, the largest signals occur at electrode 4

(purple) for right-bound APs (A) and electrode 2 (red) for left-bound APs, shown in bold and a larger font in the schematics. Rootlet diameters and the AP speeds used in constructing the predicted signals are shown and recordings are displayed from top to bottom in the order of increasing AP speed. Trial names are shown as "Rat#.Rec#.StimulusSide". Vertical scale bars are 25 µV and apply to each pair of plots showing signal means in one and model predictions in the other. Horizontal scale bars of 50 µs apply to all plots.

4.3.2.3 Theoretical model is highly predictive of recorded neural signals

The second column of plots in Figure 4.9 shows simulated neural signals (white lines) overlapping the raw signals at each electrode. Rootlet diameters and AP speeds used to generate these are shown in the bottom right corner of each plot. Visual comparison of the signal means to their simulated counterparts demonstrates the model's highly predictive capacity. In the majority of trials, it is difficult to distinguish mean signals from simulated ones. Figure 4.10 shows negative peak amplitudes and their means at each electrode location. For APs traveling to the right (upper two plots), electrode 4 at 6 mm records the largest signal peaks and, for APs traveling to the left (lower two plots), electrode 2 at 2 mm has the largest signal peaks. In Figure 4.10A, peaks were simulated using the same rootlet diameters and AP speeds as in Figure 4.9 for the trials shown. Simulated peaks (dashed lines) lie well within the range of peaks recorded at each electrode and, in most instances, intersects or nearly intersects the mean signal peak at each electrode location, further validating the model's ability to accurately predict signal amplitudes.

When rootlets are assumed to be absent (i.e. d=0 µm) or to completely fill the channel (i.e. d=b=200 µm), simulated peaks lie below and above those actually recorded (Figure 4.10B, C). The ability to accurately predict peak signal amplitudes between these extremes by changing only a single parameter (i.e. rootlet diameter, once an AP velocity has been

selected), suggests that other aspects of the model – such as axoplasmic, nerve and HBSS conductivities, V_p, g-ratios, the relationship between fiber diameter and conduction velocity, the relationship we modeled from Paintal's data, etc. – are probably close to their true values and relationships.
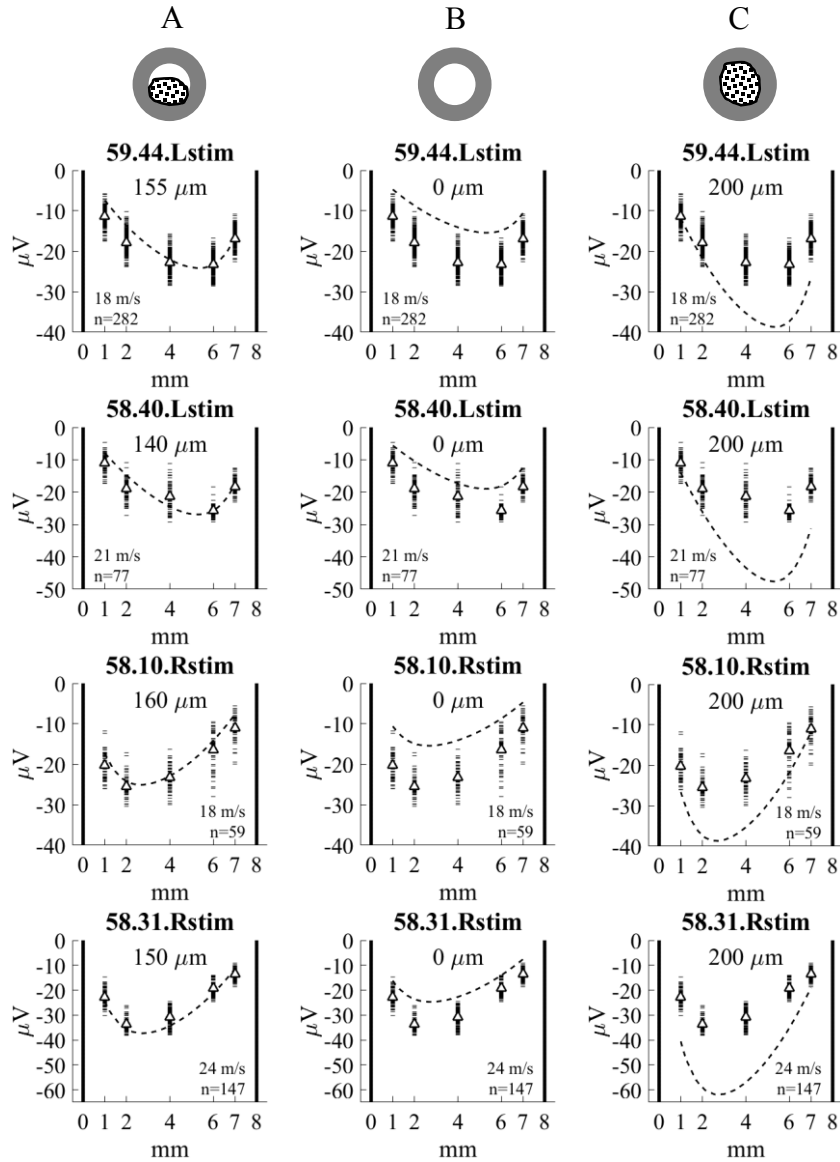
Figure 4.10 Recorded signal peaks are accurately predicted by the model. The model (dashed lines) predicts the peak signal at each electrode with optimal offset electrodes located at 2 and 6 mm, depending on AP direction, recording the largest signals. The model predicts mean peak signal amplitudes (Δ) with a high degree of accuracy, particularly when

rootlets are assumed to occupy a portion of the channel's cross section (A). It under- and over-estimates signal amplitudes when the channel is assumed to be empty (B) or completely occupied with neural tissue (C). Rootlet diameters and AP speeds used in constructing the models are shown in each plot. Schematics at the top illustrate relative channel and rootlet dimensions.

4.3.2.4 Offset electrodes preferentially detect signals traveling in preferred directions

Compared to mid-channel amplitudes, right-bound APs are enhanced and attenuated to the right and left of mid-channel, respectively (Figure 4.10). An opposite pattern emerges for left-bound APs. Negative peak amplitudes are consistently larger at optimal offset electrodes shifted in the direction of AP travel compared to a non-optimal location shifted the same distance but located on the other side of mid-channel. In other words, electrode 4 always records larger signals for right-bound APs than electrode 2. For left-bound APs, electrode 2 recordings were always larger than electrode 4. Again, this supports the theoretical predictions and our observations that offset electrodes can be used to preferentially detect APs traveling in a preferred direction.

Table 4.5 lists the *p*-values and 95% confidence intervals obtained when a paired t-test was used to compare differences in the mean negative peak amplitudes at optimal and non-optimal offset locations for the six left-stim and six right-stim trials. As in Figure 4.8, trials in each stimulation category are listed in order of increasing AP conduction velocity. The confidence intervals indicate the extent to which negative peak amplitudes at optimal electrode locations would be expected to be more negative than those at non-optimal electrode positions.

Table 4.5 Optimal vs non-optimal offset negative peak amplitudes

Table 4.5 Optimal vs non-optimal offset negative peak amplitudes

Trial name	n	electrodes compared	p-value[1]	95% confidence interval (µV)	
				lower bound	upper bound
59.15.Lstim	148		1.96E-06 *	-1.73	-0.74
58.32.Lstim	130		7.86E-17 *	-4.57	-3.01
59.44.Lstim	282	4 (opt) vs 2 (non)	8.02E-83 *	-5.79	-5.02
58.40.Lstim	77		3.41E-24 *	-7.54	-5.76
59.9.Lstim	195		1.45E-123 *	-15.47	-14.44
58.26.Lstim	163		4.35E-139 *	-26.20	-25.05
58.20.Rstim	182		1.05E-08 *	-2.38	-1.20
59.18.Rstim	188		7.14E-05 *	-1.49	-0.51
59.32.Rstim	356	2 (opt) vs 4 (non)	5.29E-121 *	-7.67	-6.88
58.10.Rstim	59		1.67E-19 *	-10.29	-7.63
59.12.Rstim	164		5.76E-96 *	-16.45	-15.11
58.31.Rstim	147		6.35E-100 *	-14.96	-13.93

*sig. (α=0.05), [1]two-tailed paired t-test

4.3.2.5 External noise artifacts distribute linearly inside channel

We observed that stimulus voltages appeared to be linearly distributed inside the channel.
Voltage spikes recorded by the electrode closest to the tip of the stimulating pipette had
the largest signals, the electrode furthest away had the smallest and those in between had
amplitudes apportioned linearly between these two extremes (Figure 4.11) Linearity of
artifact noise seems to be independent of their amplitudes. Stimulus pulses produced peak-
to-peak amplitudes ranging between 60-400 µV at electrodes nearest the stimulus pulse,
yet goodness-of-fit R^2 values are never less than 0.972. These data demonstrate a nearly
perfect linear distribution of external noise artifacts inside the channel in accordance with
the prediction of Term 2 in Equation 1.
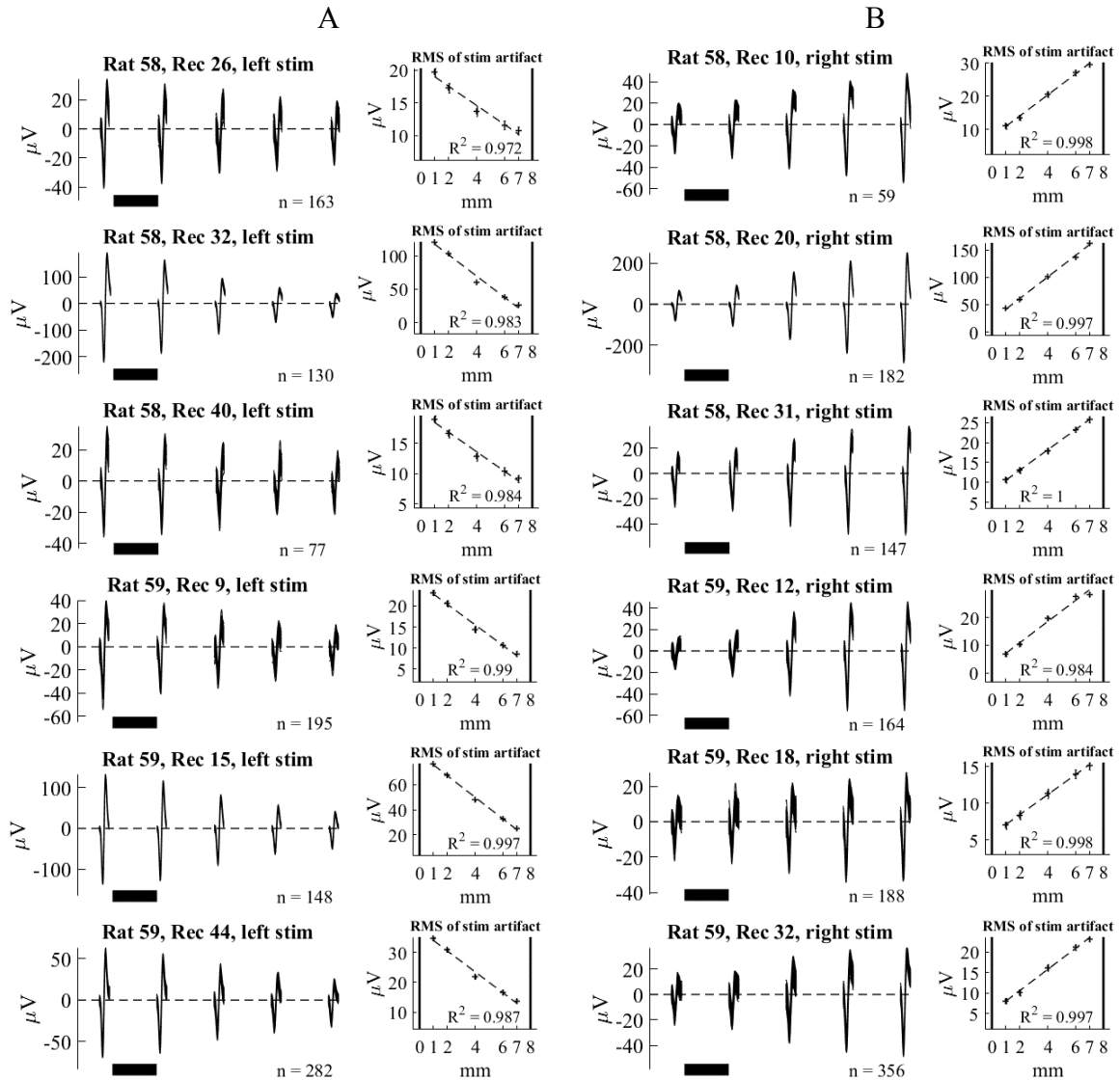
Figure 4.11 External stimulus artifacts distribute linearly inside the channel. Stimulation pulses are delivered on the left (A) and right (B) sides of the channel. For each recording, artifacts are aligned to the trigger pulse and shown overlapping each other at each electrode. The largest signals appear at the electrode nearest the stimulus pulse. RMS means and standard deviations of the artifact signals recorded at each electrode are plotted to the right of each recording with bold vertical lines indicating channel extents. Best-fit lines are shown along with their corresponding goodness-of-fit (R^2) values. Scale bars are 25 µs.

4.3.3 Reference configurations to reduce external noise artifacts at offset electrodes

4.3.3.1 Weighted references

Because external voltage artifacts distribute in a linear fashion inside the channel, the artifact noise anywhere in the channel can be estimated using the artifact noise measured at any two other locations. We used this concept to construct "weighted references" for the 3 inner electrodes at 2, 4 and 6 mm by scaling (i.e. "weighting") and then summing the voltages measured at electrodes at 1 and 7 mm, nearest the channel ends. For example, the weighted reference for the electrode at 2 mm was created by adding $5/6^{ths}$ of the voltage at 1 mm and $1/6^{th}$ of the voltage at 7 mm; the reference for the mid-channel electrode at 4 mm was created by adding $3/6^{ths}$ the voltage at 1 mm and $3/6^{ths}$ the voltage at 7 mm, the mathematical equivalent of the pseudo tripole reference where two end electrodes are shorted together; the reference for the electrode at 6 mm was created by adding $1/6^{th}$ the voltage at 1 mm and $5/6^{ths}$ the voltage at 7 mm. As Figure 4.12 A demonstrates, the weighted reference signals (blue) almost exactly match the actual noise artifacts (red) recorded at the 2, 4, and 6 mm positions and nearly cancel each other out when their difference is taken (Figure 4.12 B). When weighted references are used as the reference signal for the 3 inner electrodes, neural signals remain prominent while stimulus artifacts are almost completely eliminated (Figure 4.12 C) and external noise amplitudes are consistently smaller at offset electrodes compared to mid-channel (Figure 4.12 D). The mean RMS artifact noise at mid-channel (4 mm) is larger than at either offset position (2 and 6 mm) for the 4 trials shown and was a consistent finding for other trials (not shown).

The weighted reference approach produced improved artifact reduction at offset electrodes compared to mid-channel even when artifact amplitudes at offset locations were originally larger. For example, mean RMS artifact signals at 2 mm for the "left stim" recordings initially exceed those at mid-channel before the weighted reference is subtracted (red) and become smaller afterwards (blue). Similar trends are observed at the 4 mm location for the "right stim" recordings.
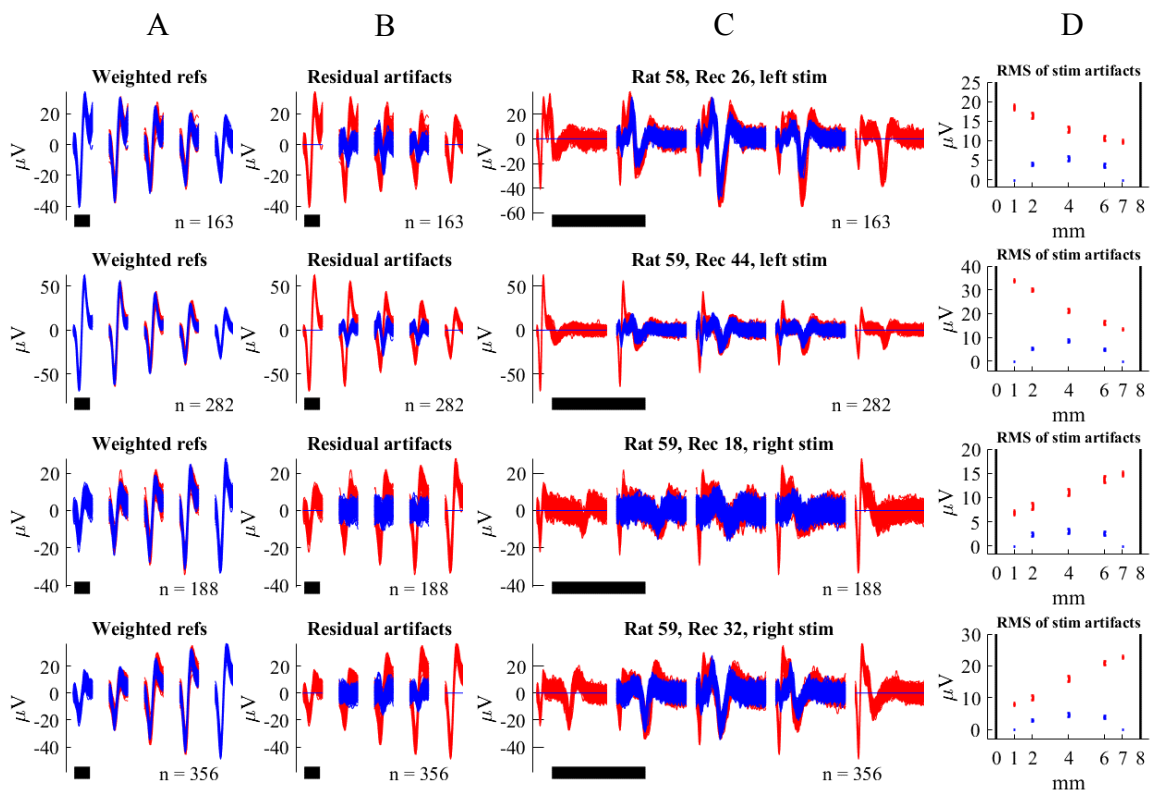
Figure 4.12 "Weighted references" for minimizing external noise artifacts at offset electrodes. The upper and lower two rows of plots are for trials where stimulus pulses were applied to the left and right side of the channel, respectively. In (A), weighted reference signals (blue) are overlaid on the original stimulus artifact noise (red) and their differences (blue) shown in (B) with the original artifacts (red) again shown in the background for comparison. (C) Signals at each electrode before (red) and after (blue) weighted reference signals were subtracted. Neural signals are preserved while artifacts are nearly eliminated. (D) Artifact RMS means and standard deviations before (red) and after (blue) weighted references are subtracted. Scale bars are 20 µs in (A) and (B) and 200 µs in (C).

4.3.3.2 Parallel references

An alternative to the pseudo tripole reference was demonstrated in cuffs where a single electrode positioned in the middle of an outer cuff was used as a reference for a mid-channel electrode situated in an inner cuff (Thomsen et al., 1996). We explored a similar approach for offset locations using a pair of parallel channels each containing an electrode having equivalent longitudinal non-central positions (Figure 4.13). Stimulation pulses were delivered to each of 12 locations arranged in a grid of points near the left side of the device. With the exception of two locations 1 mm to the right and left of the centerline between the two channels (e.g. grid points (1,1) and (1,-1)), recorded signals were nearly identical at all locations, with their differences resulting in nearly perfect noise cancellation (C). This suggests that a parallel reference electrode located in an empty channel parallel to the one containing the nerve could serve as a viable reference for reducing external noise artifacts at offset electrodes.
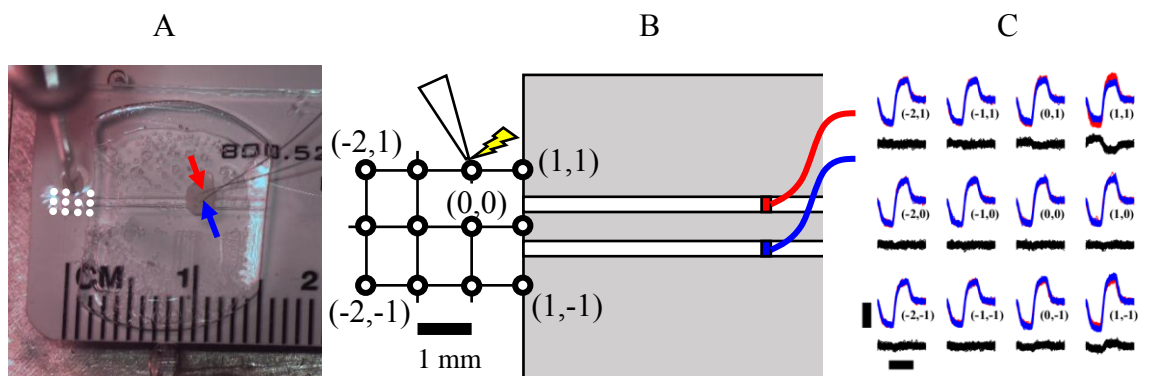
Figure 4.13 "Parallel references" for minimizing external noise artifacts at offset electrodes. Stimulating current was delivered through the end of a pipette having a tip aperture of about 80 μm to each of 12 locations arranged in a 3x4 grid, shown schematically in A (white dots) and B. Grid points are 1 mm apart with the origin at (0,0) located on an imaginary line midway between the 2 channels and 1 mm to the left of the left entrances. Stimulus pulses were bi-phasic current pulses with durations of 50 μs and amplitudes that

were adjusted slightly at each grid point to maintain recorded signal amplitudes to about 200 µV peak-to-peak. The device was made of PDMS having parallel channels 14 mm long x 200 µm in diameter. Electrodes are chlorinated silver wires with diameters of 100 µm inserted into the top of each channel about 9 mm from the left end (2 mm to the right of center). Red and blue arrows in A highlight the locations of the electrodes that are covered in petroleum jelly (Vaseline). The medium is HBSS at room temperature (22 °C). For each location, signals recorded by the blue and red electrodes are shown overlapping in corresponding blue and red traces in (C) with their differences displayed in black. Vertical and horizontal scale bars in (C) are 100 µV and 25 µs, respectively.

4.3.4 Background noise levels are reduced at offset electrodes

We found background noise levels at offset electrodes to be less than at mid-channel, where background noise levels were consistently greatest. Raw background noise signals at each electrode position are shown in Figure 4.14 with the amplitudes at 4 mm being visibly greatest in many of the trials and those at offset locations nearer the channel ends being the smallest. Plots of the RMS noise at each electrode location confirm this. The Johnson noise model shows similar trends even when assuming an empty channel containing no rootlet – i.e. the rootlet diameter was set to 0 when computing the cross-sectional area. In this case the model predicts smaller noise amplitudes than what we observed which is reasonable since our channels contained a rootlet in actuality. When the channel cross section is reduced by a rootlet's assumed cross-sectional area, shown in the RMS plots, the model matches the data well. This suggests that the background noise is predominantly of a thermal nature and that thermal noise will always be largest at mid-channel and less at offset electrodes.
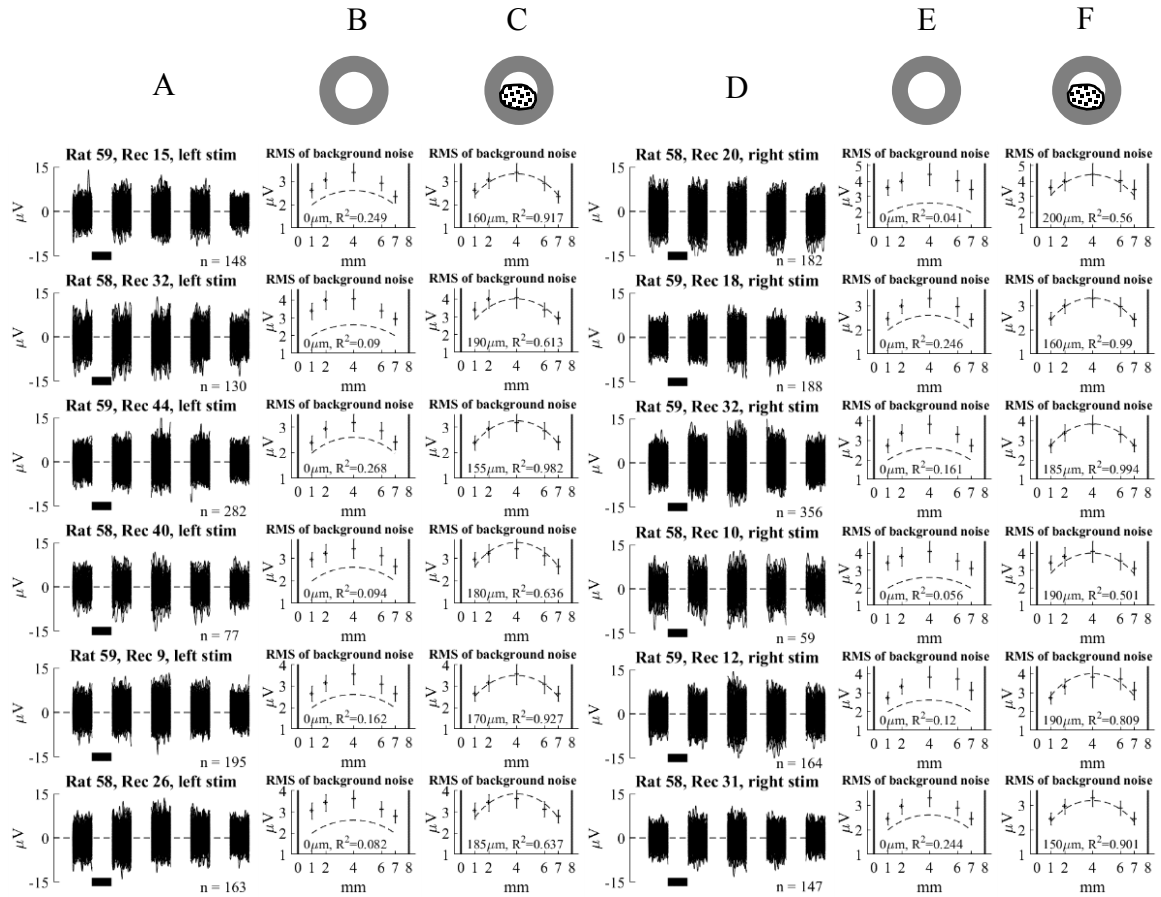
Figure 4.14 Background noise is less at offset compared to mid-channel locations.
Raw background noise signals are shown for left-stim (A) and right-stim (D) trials. For
left-stim trials, RMS means and standard deviations of the noise at each electrode are
shown in (B, C). Dashed lines represent the Johnson noise model when channels are
assumed to be empty (B) compared to when they contain a rootlet with the diameter shown
in the left corner of each plot (C). These two conditions are shown schematically at the
top of the figure. (E and F) show similar results for the right-stim trials. R2 values provide
goodness-of-fit between recorded noise levels and the model. Scale bars are 50 μs.

4.3.5 High pass filtering alters signal patterns at offset electrodes

High pass filters preferentially attenuate signal amplitudes at optimal offset electrodes with

signals for slower APs being particularly affected. This can be seen in Figure 4.15 A where

signals from APs traveling at 3 different speeds are bandpass filtered with the high pass

cutoff frequency varied from 10-700 Hz. The filter was a 2nd order Butterworth designed

in Matlab using the "Butter" function with the lowpass cutoff fixed at 20 kHz. The largest

signals are expected to occur at an optimal electrode position of about 5 mm (purple traces). As the high pass cutoff is increased from 10 to 700 Hz, the impact is most dramatic for the slowest APs having speeds of 5 and 10 m/s. The location of the largest signal shifts from the electrode at 5 mm, to the right of mid-channel, to positions to the left of center (i.e. electrodes at 2 and 3 mm for the 5 and 10 m/s AP, respectively). Signals for the 15 m/s AP are only affected at the 700 Hz cutoff frequency with the impact becoming progressively less at higher AP velocities (not shown). Signals remain mostly indifferent over a wide range of lowpass filter settings as shown in Figure 4.15 B with hardly any noticeable differences between signal amplitudes when the lowpass cutoff is changed from 20 to 10 or 5 kHz. All signals are attenuated when a low-pass cutoff of 1 kHz is used, with faster APs being preferentially impacted.
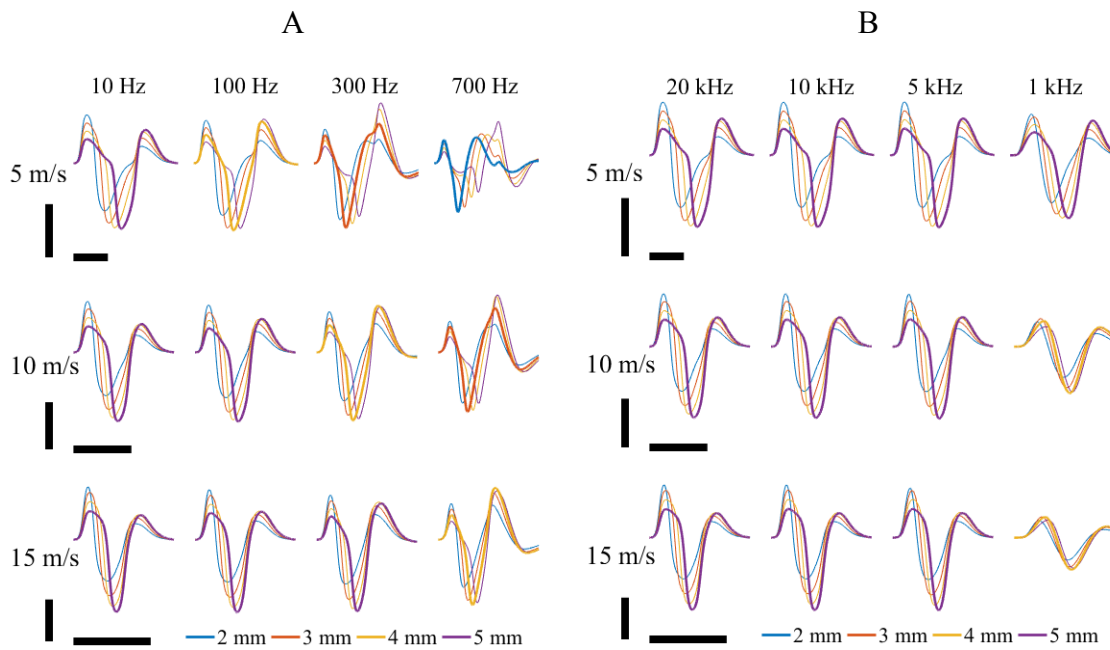
Figure 4.15 High-pass filtering can compromise signal enhancement at offset electrodes. Increasing high pass cutoff frequencies attenuates signals at the optimal offset location. With no filtering, the 5 mm position is optimal for maximizing signal amplitudes.

Neural signals are simulated at electrodes located at 2, 3, 4, and 5 mm (measured from the left side of the channel) for right-bound APs with speeds ranging between 5-15 m/s are filtered using different bandpass filter settings. In (A), the lowpass cutoff is fixed at 20,000 Hz and the high pass cutoff is increased from 10 to 700 Hz. In (B), the high pass cutoff is fixed at 10 Hz and the lowpass cutoff is decreased from 20,000 to 1,000 Hz. Signals with the largest negative peaks are shown in thicker lines. Vertical scale bars are 5, 10 and 15 µV for the 5, 10 and 15 m/s cases, respectively. Horizontal scale bars are 1 ms. Signals were simulated using an 8 mm x 200 µm I.D. channel and a temperature of 37 °C.

4.4 Discussion

4.4.1 Overview

Action potential directionality is characteristic of the information they transmit and their asymmetry is characteristic of their directionality. In microchannel recordings, AP asymmetry produces extracellular signals that peak at locations offset from mid-channel in their direction of travel. Offset electrodes, therefore, represent recording configurations that are sensitive to AP asymmetry and, by extension, to their directionality. A mid-channel electrode, on the other hand, represents a symmetric recording configuration that produces the same signal for an AP entering the left side of the channel as it does for an identical AP entering the right (Sabetian et al., 2017). This configuration, therefore, cannot be used to determine AP directionality. Mid-channel symmetry is also inherently misaligned to AP waveforms and are not optimal for maximizing recorded signals.

Microchannels were conceived explicitly for the purpose of detecting individual action potentials (Loeb et al., 1977). Although FitzGerald and colleagues noted the possibility of signal enhancements at offset electrodes (FitzGerald et al., 2008), most microchannels developed to date use a mid-channel electrode in a pseudo tripole configuration commonly found in cuffs which significantly limits their usefulness. This is unfortunate, since

microchannels were envisioned and later used as the basic building blocks for regenerative electrode array technologies designed to record from small nerve bundles containing hundreds of axons conducting signals in different directions (FitzGerald et al., 2008, FitzGerald et al., 2012, Minev et al., 2012).

4.4.2 Offset electrodes represent a new paradigm for neural recording

Determination of AP directionality usually requires a minimum of two recording sites. Offset electrode configurations represent a new paradigm in extraneural recording techniques, in that a single electrode inside the channel can be used to determine AP directionality. Any recording configuration using multiple electrodes, such as bipolar (Sabetian et al., 2017) or any of the many velocity selective recording (VSR) methods (Taylor et al., 2004, Yoshida et al., 2009, Schuettler et al., 2013), can simultaneously implement offset electrode techniques insofar as these electrodes use appropriate references that do not include each other. Unlike VSR techniques, offset electrodes may provide greater flexibility and less complexity in that they need not be equally-spaced apart, do not require multiple layers of differential amplifiers to produce their output signals, and require only a minimum of 3 electrodes compared to 4 in VSR methods for detecting spikes in a given direction.

4.4.3 Improved spike detection and classification

Thermal noise at optimal offset locations (i.e. at 2 and 6 mm) is about 0.85 of the noise at mid-channel and signal amplitudes at these offset locations are between 1.1-1.2 times the amplitude at mid-channel. Therefore, we estimate signal-to-noise ratios at offset electrodes to be between 1.3-1.4 times those at mid-channel. This would improve many spike

detection and spike classification algorithms, such as cross-correlation methods (Heetderks and Williams, 1975), template matching (Lewicki, 1998), and matched filters (Roberts and Hartline, 1975), where success rates (i.e. the proportion of spikes classified correctly) are correlated to SNR (Bankman et al., 1991, Gozani and Miller, 1994, Gribi et al., 2018).

4.4.4 Signal discrimination using offset electrode recordings

Not only are signal amplitudes different at offset electrodes for APs traveling in opposite direction, but the recorded signals also have very different shapes. Scaling signals by their negative peak widths or by their positive phase amplitudes serve to amplify differences between signals recorded for APs traveling in opposite directions. For example, if recorded signals were divided, perhaps repeatedly, by their width factors a left-bound AP would produce a negligible response at electrode 4 compared to a right-bound AP with similar speed. A linear or non-linear combination of width, height or other shape factors could be used to scale signals so that only those associated with the AP traveling in the direction of interest is preserved. These techniques remain to be explored.

4.4.5 Offset electrodes are readily incorporated into existing neural recording technologies

The offset electrode paradigm can readily be incorporated into current mono-channel microchannel technologies. The offset paradigm requires an additional reference terminal situated external to the channel, preferably in close proximity to it. As we describe and demonstrate, weighted references using the end electrodes would serve as a reference signal for the offset electrode, or electrodes, between them.

For planar or circular arrays of microchannels, channels containing left or right offset electrodes would preferentially detect afferent or efferent signals. Empty channels could serve as a parallel reference to those containing axons. Other geometries could lead to even more efficient reference channel configurations. For example, regenerative electrode arrays could be sparsely populated with empty channels, each containing two parallel references to match the left and right positions of those in the recording channels. In this way, one reference channel could serve as a parallel reference for multiple nearby recording channels so that the number of lead out wires would approach the number required for current and past regenerative electrode array designs.

4.4.6 Offset electrodes enhance the capability of existing devices

When used to stimulate axons, offset electrodes have been demonstrated to elicit neural activity in a direction opposite to the channel end closest to the electrode (FitzGerald et al., 2009). Thus, offset electrodes can be used to selectively record and elicit action potentials traveling in a desired direction. Arrays of microchannels containing offset electrodes at different positions in different channels would be capable of differentiating between neural traffic traveling in opposite directions as well selectively eliciting activity in sensory or motor axons or block signals traveling in specific channels. In this sense, offset electrodes would significantly improve the usefulness of these devices, all of which currently employ mid-channel electrode configurations (FitzGerald et al., 2012).

4.4.7 Theory can be used to derive action potential waveforms

The "difference" term in Eq. 7 represents a linear transformation of the transmembrane action potential from a spatial to a temporal domain. We approached this using a linear

algebra approach because it can readily be implemented in reverse – i.e. to predict action potential waveforms from the signals recorded at each electrode. This inverse transformation has the form:

$$(30) \qquad X \;=\; A^{-1} \cdot Y$$

One potential use for this inverse transform would be to check the assumption made here and by others that the AP waveforms are invariant and maintain a fixed shape as they traverse the channel. Predicted AP waveforms at each electrode could be estimated using Eq. 30. X vectors with identical shapes would suggest that AP profiles are invariant, while dissimilar X vectors would provide a sense of how waveform shapes might morph with position as they travel through the channel. These types of analyses would at the very minimum confirm a key model assumption or provide and raise new insights and questions concerning the nature of propagating neural signals in microchannels.

4.5 Conclusions

This work provides evidence that offset electrodes enhance neural recording capabilities in microchannels. We show that offset electrodes record larger signals, can be used to determine signal directionality, can be configured to better reject external noise artifacts and are less sensitive to thermal noise artifacts than mid-channel locations. We are optimistic that our *in vitro*-based findings are translatable to *in vivo* environments since the latter is a more complex extension of the same underlying phenomena and we do not expect internal and external currents to behave any differently in the body than what we observed in a controlled environment. The extent to which offset electrodes may provide recording

advantages in larger channels having dimensions approaching those of cuffs remains to be determined. Theoretical analyses suggest that the Stein and Pearson model is relevant to cuff-sized geometries (Struijk, 1997, Taylor et al., 2004). Unless ionic currents behave differently at these larger geometries to an extent not captured by these models, we expect offset electrodes to provide signal enhancement in cuffs as well. This would have broader clinical implications given the wide-spread use of cuffs in clinical settings (Haugland and Sinkjaer, 1995, Struijk et al., 1999, Stein et al., 1980b, Hoffer et al., 1996, Hoffer and Loeb, 1980).

CHAPTER 5

USING OFFSET ELECTRODES TO DISCRIMINATE NEURAL SIGNALS OF

INCREASING COMPLEXITY

5.1 Introduction

The ability to infer function from recorded nerve signals relies on the ability to determine

an action potential's direction, speed and firing rate, since these are surrogate markers for

function. Its directionality can be used to distinguish between events in the motor and

sensory domains, its speed can be used to infer the type of muscle fiber or sense receptor

being activated and their firing rates correlate to contractile force or the intensity of applied

cutaneous stimuli.

Chapter 4 showed recordings of single-unit action potentials (SUAPs) to be highly

stereotyped in microchannels as predicted by theory, and that offset electrodes can

potentially function as directionally-sensitive recording sites. This analysis was limited to

comparing only negative peak amplitudes of signals recorded for SUAPs and ignored

important shape differences that could improve the ability to distinguish between SUAPs

traveling in opposite directions. Also, real-world applications involve microchannels that

contain hundreds of axons that will produce an electroneurogram (ENG) characterized by

overlapping signals (FitzGerald et al., 2012) or, in the case of the compound action

potential (CAP), will generate signals characterized by maximum overlap (Gasser and

Erlanger, 1927).

While beyond the scope of this dissertation, spike detection algorithms are typically used identify and classify neural activity associated with specific axons (Chandra and Optican, 1997, Gazzoni et al., 2004). While these vary in complexity, as a general rule their performance is improved when signal-to-noise ratios are high and the frequency of overlapping spikes is low (Lewicki, 1998).

This chapter identifies two shape factors that can be used to amplify difference between signals recorded for SUAPs traveling in preferred and non-preferred directions. Using these to scale signals at offset electrodes would be expected to improve spike detection and classification rates for SUAPs traveling in the preferred direction. We investigate the types of overlaps expected to occur at mid-channel and offset electrode sites for signals traveling in the same and opposite directions as reductions in the rate of overlap would enhance detection and classification. Since CAPs have been used to document axonal regeneration after nerve transection, they could be used to characterize signals in microchannel-based regenerative electrode (RE) arrays over time. Therefore, a CAP model was developed from the SUAP model described in Chapter 4 and used to compare CAPs at mid-channel and offset electrodes. Also, CAPs recorded at offset electrodes are compared to CAPs simulated using the model developed in Chapter 4 to infer signs of axonal damage due to tearing of axons during the process of teasing rootlets.

5.2 Methods

5.2.1 Shape factors to enhance detection of SUAPs

Consider a channel containing a single offset electrode positioned near its right edge. For an action potential traveling to the right, the recorded signal is characterized by a large narrow negative phase flanked to the right and left by two much smaller positive phases (Figure 5.1 B). A similar AP traveling to the left produces a largely bi-phasic looking signal characterized by a large first positive phase, a wide and equally large negative phase, and a smaller second positive phase (Figure 5.1 A).

These differences are preserved over a range of conduction velocities and are characterized using two shape factors. The first represents the proportion of the negative phase that lies below baseline and the second characterizes the duration of the negative peak relative to the duration between the two positive peaks. These features can be combined or used independently to scale recorded signals to differentiate between APs traveling in opposite directions. Shape factors for simulated and recorded SUAPs were used to scale signals at offset electrodes.
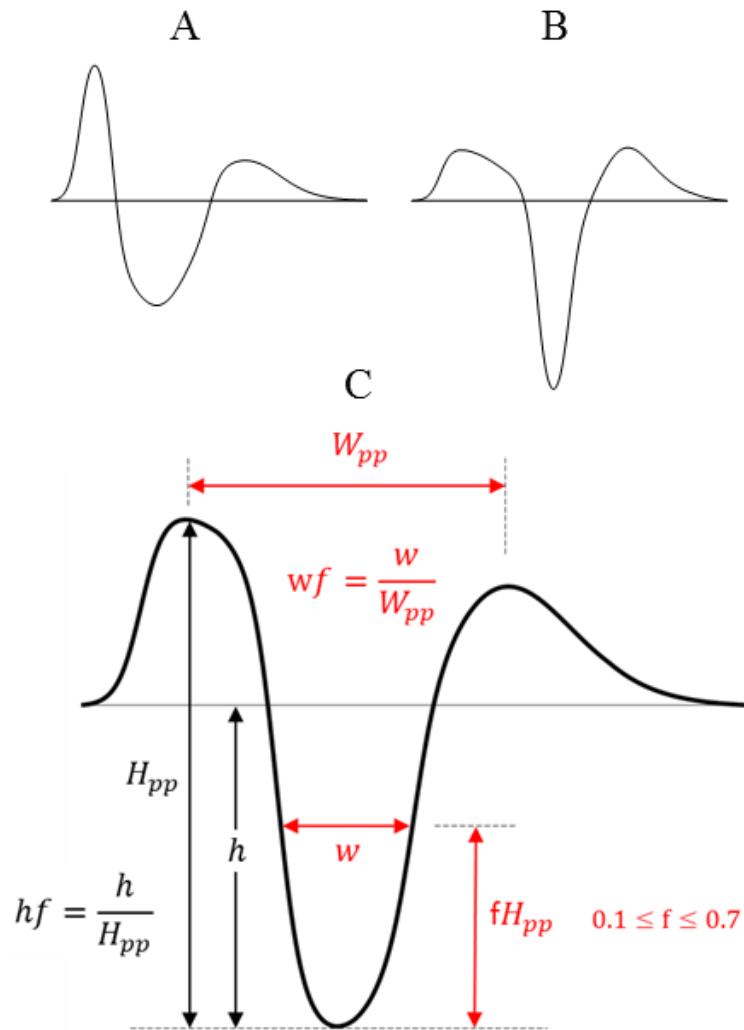
Figure 5.1 Action potentials traveling in opposite directions produce signals with different shapes at offset electrodes. For offset electrodes situated near the right end of the channel, right-bound APs produce signals characterized predominantly by a large narrow negative peak while B) left-bound APs produce signals having a large positive peak followed by a wide negative peak. C) These shape differences are characterized by two metrics derived from the amplitude (black arrows) and temporal (red arrows) domain. A height factor (hf) characterizes the portion of the peak-to-peak amplitude (H_{pp}) that lies below zero and a width factor (wf) characterizes the width of the negative peak in relation to a measure of the signal's overall duration (W_{pp}). These two metrics are seen to be quite different for the signals in A) and B).

5.2.2 Discrete spike detection in the ENG

For estimating the rate of occurrence of overlapping spikes in the ENG, the expression below was first proposed by Bankman:

$$(31) \qquad f_{overlap} = x(x-1)y^2\delta$$

where $f_{overlap}$ is the frequency of overlap events, x is the number of active fibers, y their mean firing rate and δ their mean duration (Bankman et al., 1991, Chandra and Optican, 1997). Thus, 10 active fibers with durations of 0.9 ms (δ=0.9e^{-3} s) firing at 25 Hz a piece would generate approximately 51 overlap events (out of 250 total spikes) per second. We find it more useful to characterize overlap events in terms of the number of discrete spikes that can be detected per second. Recognizing that "xy" represents the total number of spikes per second, N, the overlap frequency, $f_{overlap}$, can be approximated as:

$$(32) \qquad f_{overlap} \approx N^2\delta$$

The difference between N and $f_{overlap}$ gives the number of discrete spikes per second, $n_{Bankman}$, as:

$$(33) \qquad n_{Bankman} \approx N(1-N\delta)$$

However, the Bankman model has a major limitation. Eq. 5.3 is parabolic with zeros at N=0 and N=1/δ and when the total number of spikes exceeds the zero at 1/δ, the Bankman model predicts negative discrete spike rates, which is impossible.

Hence, a model to estimate discrete spike rates was created. Matlab (Mathworks, CA) was used to simulate different numbers of axons firing randomly at different frequencies with a specific spike duration. Axon numbers and firing rates were varied so that their product, the total number of spikes per second, ranged between 0 and between 6000-12000 spikes (i.e. $0 <= N <= 6000\text{-}120000$). For each value of N, the number of non-overlapping spikes in each simulated cohort of asynchronous neural activity was counted. This process was repeated 50 times and discrete spike counts were averaged to obtain a representative value for the number of discrete spike events expected at each N value. Figure 5.2 A, B each show simulations consisting of 20 axons each firing at 10 Hz and having mean spike durations of 0.5 and 1 ms in (A) and (B), respectively. The number of discrete spikes (blue) in (A) is greater than in (B), where spike durations are twice as long and the number of overlapping spikes (red) per the 100 ms time window shown is higher.

Figure 5.2 C, D show the average number of discrete spikes for N ranging between 0 and 6000 Hz. The Bankman model (dashed line) matches the data when the total number of spikes per second is relatively small and the occurrence of overlapping spikes is expected to be infrequent. However, it does not correctly predict overlap behavior when the total number of spikes per second is large since the number of discrete spikes per second can never be less than zero as the Bankman model predicts. On the other hand, our simulations show the number of discrete spikes asymptotically approaches zero as the total number of spikes per second becomes large, as would be expected.
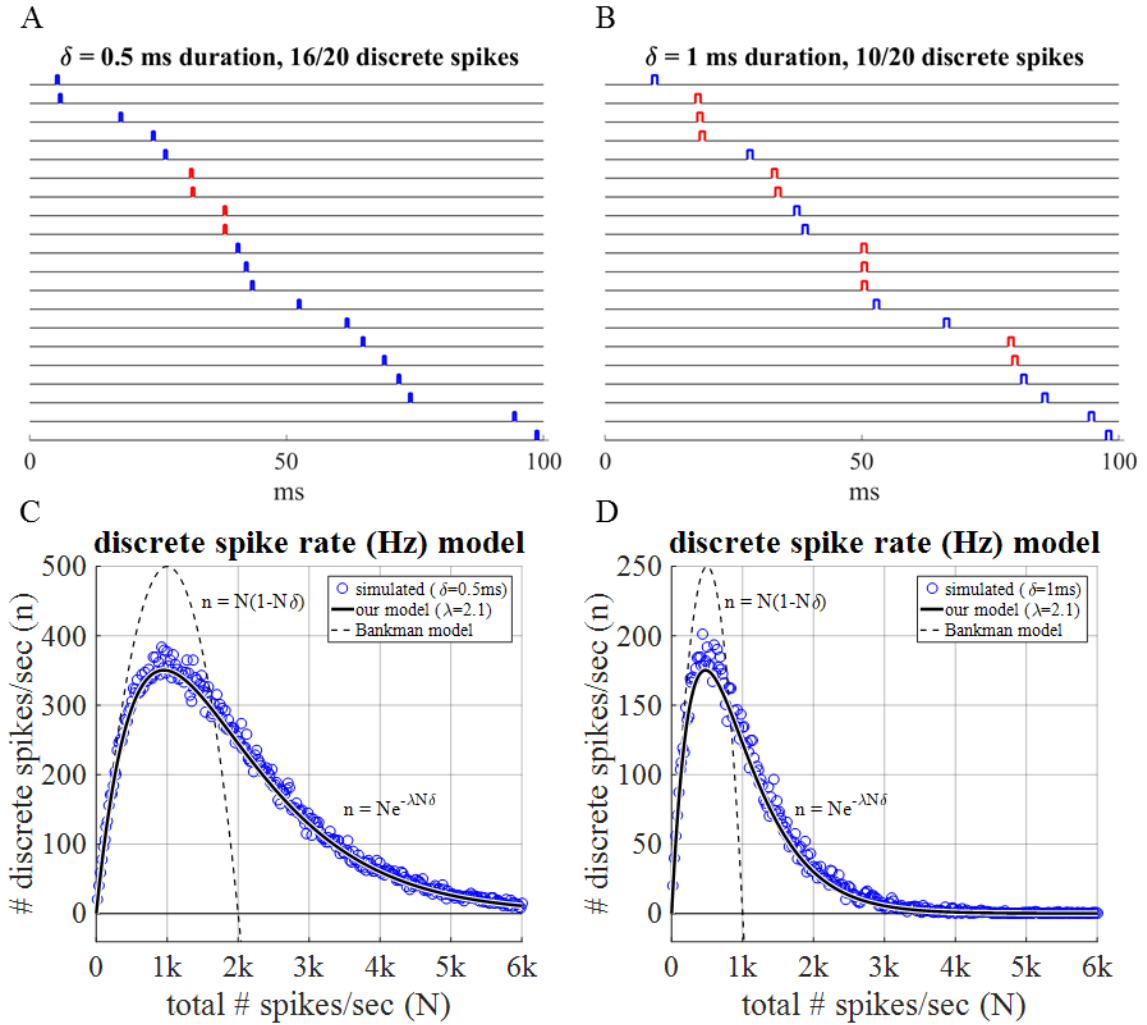
Figure 5.2 Discrete spike rate model. Simulations show asynchronous spiking activity of 20 axons having mean spike durations of A) 0.5 ms and B) 1 ms. Discrete (non-overlapping) and overlapping spikes shown in blue and red, respectively. Neurons have a mean firing rate of 10 Hz, firing once during the 100 ms time window shown. These types of simulations were run using varying numbers of axons and firing rates to generate the data points (blue circles) in C) and D) modeled using the equation shown in the plots (black lines). The dashed line shows the frequency of discrete spikes predicted by the Bankman model.

A parametric model of the form

(34) $$n = Ne^{-\lambda N\delta}$$

with $\lambda = 2.1$ was found to fit the data over a wide range of spike durations and this model was used to estimate discrete spike events at mid-channel and offset electrode locations.

5.2.3 Simulated CAPs

Compound action potentials (CAPs) were simulated by summing the SUAPs obtained for axons conducting signals at different speeds using a theoretical framework previously described (see Chapter 4). For simulating whole nerve CAPs, the distribution of fibers conducting at different specific speeds was reconstructed from Waddell et al (Waddell et al., 1989) for the dorsal L5 root in rats. Early simulations assumed all axons fired at the same instant. Realistically, however, action potentials are initiated at slightly different times. Therefore, a "jitter" was incorporated into all simulations that required axons to fire within 50 µS of the stimulation pulse used to elicit CAPs.

5.2.4 Recorded CAPs

The *in vitro* experimental methods described in Chapter 4 for producing single-unit activity in teased rootlets was used to generate compound action potentials. This was achieved by increasing stimulus currents above those required to elicit single-units until further increases produced no noticeably changes in signals recorded at each electrode, which represented the maximal CAP response. Typical stimulus currents required to maximally excite rootlets and generate CAPs were frequently between 1.5-4 µA. Currents less than 1.5 or greater than 4 were occasionally required to generate the maximal CAP response.

5.3 Results

5.3.1 Shape factors to enhance detection of SUAPs

5.3.1.1 Signal discrimination without using shape factors

On the basis of amplitude alone, offset electrodes can be used to separate efferent from afferent signals. Figure 5.3 directly compares negative peak amplitudes recorded for right-(blue) and left-bound (red) APs. Signals for right-bound APs are usually more prominent at the 6 mm offset electrode while those traveling to the left have larger signals at the 2 mm offset position. This trend is more pronounced if right-bound signals are compared to left-bound signals that are artificially constructed by reversing right-bound ones – i.e. responses at electrodes 1 and 2 become those at electrodes 4 and 5 and vice versa - and are designated by "rev" in the titles for D-F. In these cases, signal peaks at the optimal offset locations are separable on the basis of amplitude alone. For example, a threshold of -40 µV would enable right bound APs to be detected only at the 6 mm offset location and left-bounds to only be detected at the 2 mm offset location. Mid-channel locations record nearly equivalent peak amplitudes and cannot be used to distinguish right- from left-bound APs.
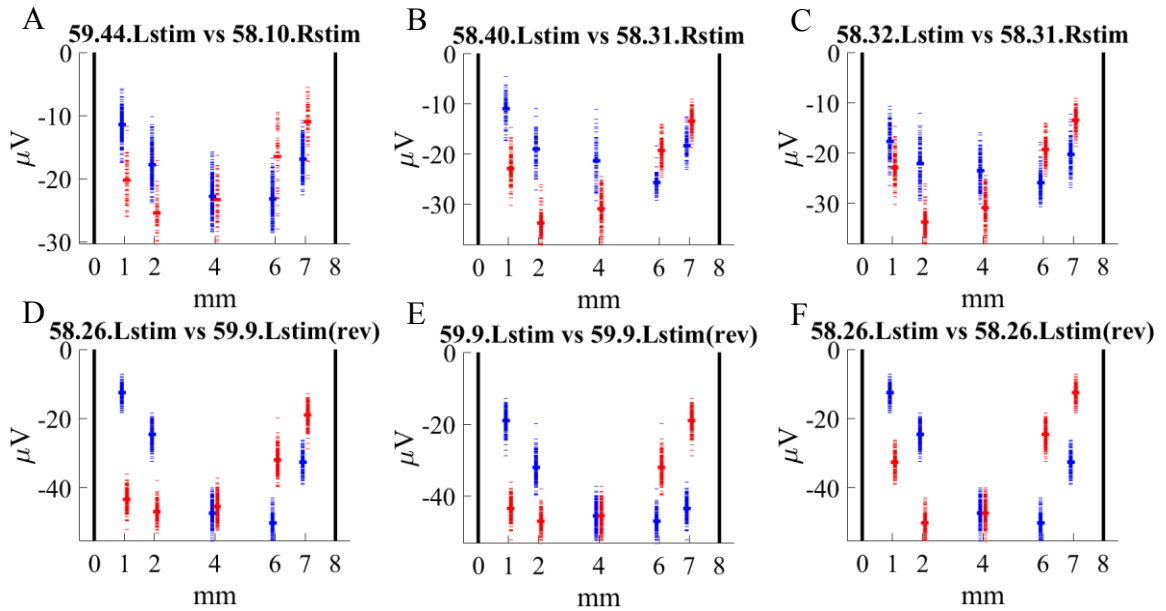
Figure 5.3 Offset electrodes preferentially record signals traveling in a given direction. Negative peak amplitudes for single-units recorded in different trials described in Chapter 4 are shown with solid bars designating the mean negative peak amplitude at each electrode. In (A)-(C), peak amplitudes for 3 different right-bound AP trials (Rat 59/Rec 44, Rat 58/Rec 40 and Rat 58/Rec 32), shown in blue, are compared to 2 different left-bound AP trials (Rat 58/Rec 10 and Rat 58/Rec 31), shown in red. In (D-F), recordings for left-bound APs were artificially constructed by reversing those for right-bound ones – i.e. signals recorded at electrodes 1 and 2 become those at electrodes 4 and 5 and vice versa. These are designated by the suffix "rev" appended to the trial name in the titles. In (D), right-bound signals for Rat 58/Rec 26 are compared to left-bound-signals constructed by reversing right-bound APs for Rat 59/Rec 9. In (E) and (F), right-bound signals for Rat 58/Rec 9 and Rat 58/Rec 26 are compared to their own reversed signals.

5.3.1.2 Signal discrimination using shape factors

Figure 5.4 illustrates theoretically that right- and left-bound action potentials are predicted to produce signals that have consistently different shapes over a wide range of conduction velocities. For an offset electrode located 6 mm from the left edge of an 8 mm long channel, APs traveling between 5-30 m/s in the "preferred" right-bound direction have larger negative peaks (h) compared to APs traveling in the "non-preferred" left-bound direction. These differences are preserved even when negative peak amplitudes are

normalized by peak-to-peak amplitudes (H), which remain nearly the same for APs traveling in opposite directions, to produce the height factor (upper right plot in Figure 5.4).
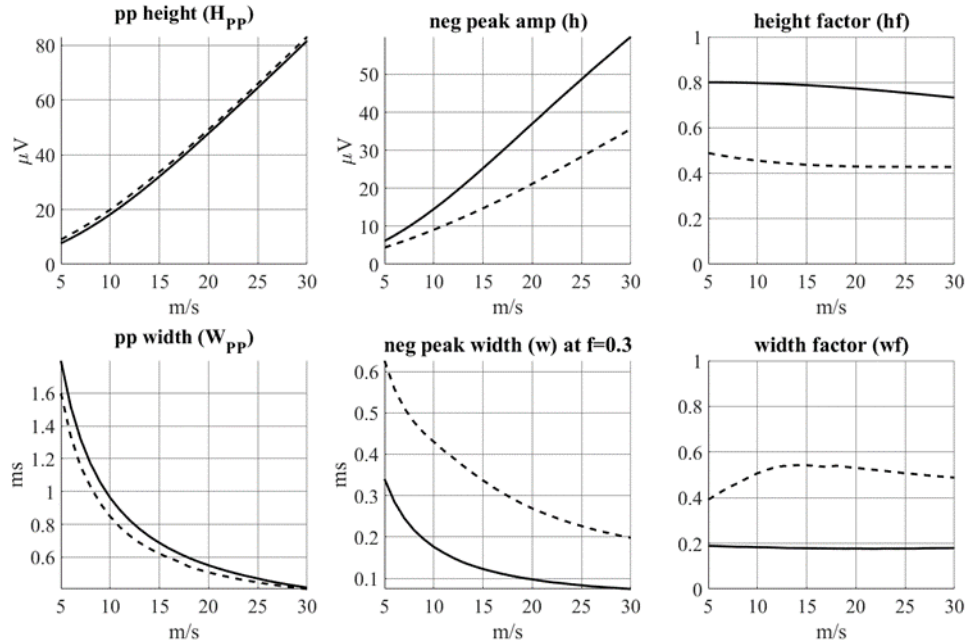
Figure 5.4 Height and width factors characterize shape differences at offset electrodes. Shape factors (hf and wf) for APs traveling to the right (solid) are markedly different from those traveling to the left (dashed) over a wide range of conduction velocities. Negative peak widths were obtained using f = 0.3 (see Figure 5.2).

Negative peak durations, or widths (w), are predicted to be consistently narrower for APs traveling in the preferred right-bound direction compared to those traveling to the left. Normalizing them by the width between positive peaks (W) produces width factors (wf) that, like height factors, are noticeably different between APs traveling in the preferred and non-preferred directions (lower right plot in Figure 5.4).

Because they represent normalized metrics that remain reasonably constant for APs traveling at different speeds, height and width factors can be used to differentially enhance

recordings of APs traveling in the preferred direction over a wide range of conduction velocities. This is shown in Figure 5.5, where simulated recordings of APs traveling in opposite directions at different speeds are scaled by their respective height and width factors. Compared to unmodified signals (1st column, far left), multiplying by the height factor (2nd column) or dividing by the width factor (3rd column) enhances the amplitude of the signal recorded for preferred right-bound APs compared to those traveling in the non-preferred left-bound direction. Height and width factors can also be combined into hybrid metrics that may be more robust and less susceptible to variations in either factor alone. Perhaps the simplest hybrid metric is height factor to width factor ratio (hf/wf). Scaling signals by one multiple of the hf/wf ratio produces signal differences that are even more pronounced than when signals are scaled by either factor alone (4th column).
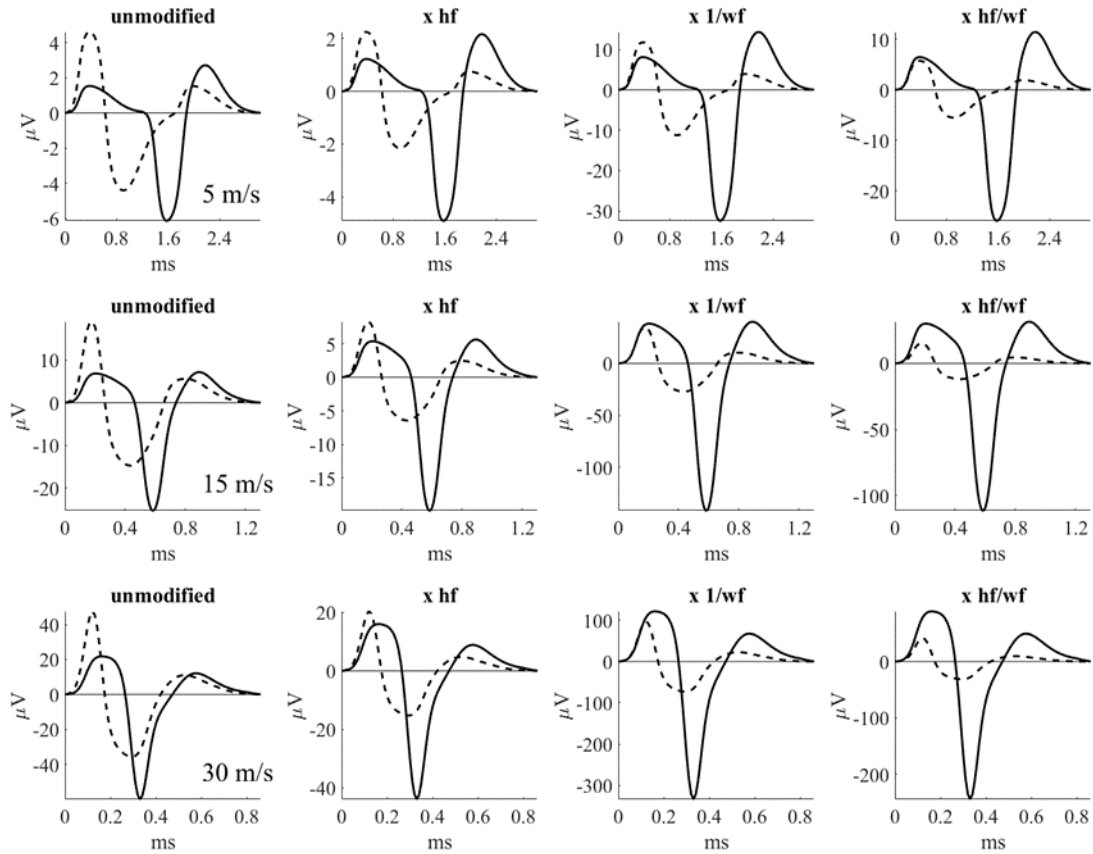
Figure 5.5 Shape factors enhance the ability to discriminate between simulated APs traveling in opposite directions. Differences between right- (solid) and left-bound (dashed) APs traveling at 5, 15 and 30 m/s are enhanced when signals recorded at a 6 mm offset electrode are either multiplied by their respective height factors (hf) or divided by their width factors (wf). These factors can be squared or combined in a variety of ways to further accentuate differences. For example, multiplying by their ratio (hf/wf) greatly attenuates the signal recorded for left-bound APs compared to those associated with APs traveling in the preferred direction to the right.

Similarly, differential signal enhancement is achieved when one iteration of the hf/wf ratio is used to scale neural signals recorded at offset electrodes. Figure 5.6 compares the signals recorded for preferred right-bound APs at electrodes 4 and 5, located 6 and 7 mm from the left edge of an 8 mm long channel, respectively, to those recorded for equivalent non-preferred left-bound APs. In this example, left bound signals are represented by the recordings on electrodes 1 and 2, located 1 and 2 mm from the left edge of the channel,

respectively. Unmodified signals in (A) show amplitude differences that are clearly visible in the raw recordings and consistent for every recorded spike as indicated by the ratio of their amplitudes never being less than 1 (red horizontal lines in the ratio plots). Signals for APs traveling in the preferred direction (purple and green) are significantly enhanced over those associated with APs traveling at identical speeds in the opposite direction (red and blue), when they are scaled by their respective hf/wf shape factors. At electrode 4, the shape factor universally enhanced every right-bound spike over left-bound ones, with the ratio of their negative peak amplitudes being increased from approximately 2 (A, upper right plot) to between 5-10 (B, upper right plot). At electrode 5, the shape factor universally enhanced every right-bound spike over left-bound ones to an even a greater extent, with the ratio of negative peak amplitudes being increased from, again, approximately 2 (A, lower right plot) to between 10-30 (B, lower right plot).
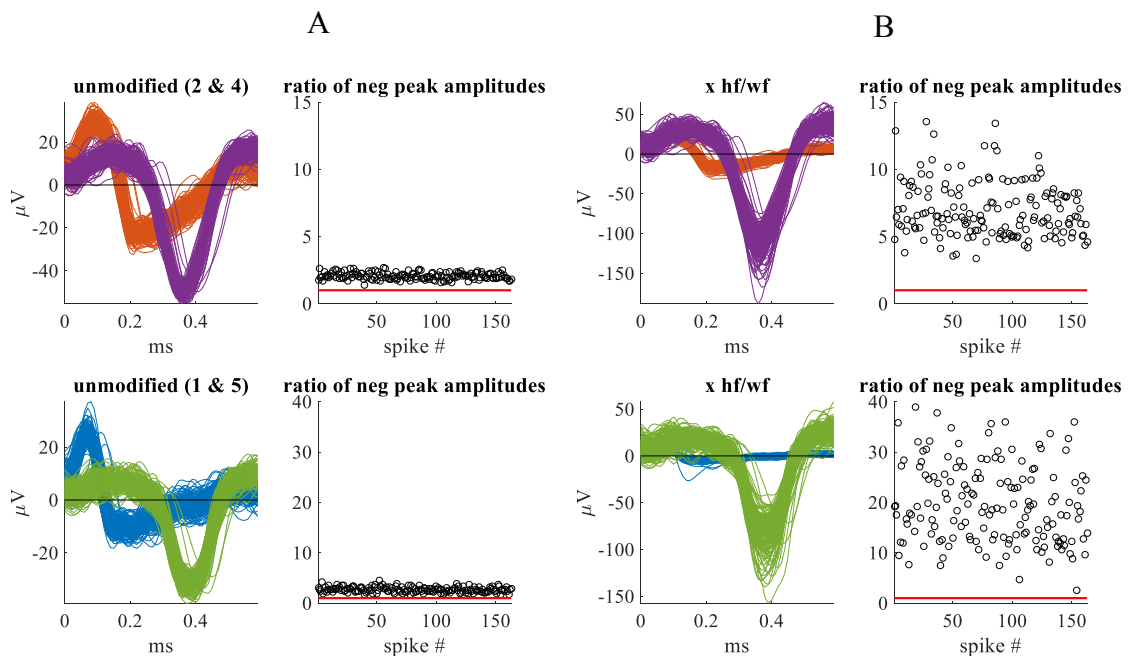
Figure 5.6 Shape factors enhance the ability to discriminate between recorded APs traveling in opposite directions. Recordings shown are only for right-bound APs.

Signals at offset electrodes 1 (blue) and 2 (red), located near the left end of the channel, represent what electrodes 4 and 5, located near the right end of the channel, would have been expected to record for similar APs traveling to the left. A) Optimal offset electrodes, 4 and 5 on the right, record right-bound APs at approximately twice the amplitude of what they would have recorded for left-bound APs. B) When recordings are scaled by the height-to-width factor ratio (hf/wf), the signals for right-bound APs dominate. At electrode 4 (purple), signals for right-bound APs are between 5-10 times as large as those for left-bound APs. At electrode 5 (green), signal enhancement after scaling by the shape factor are even more pronounced, with signals for right-bound APs being between 10-30 times greater than left-bound ones.

5.3.2 Discrete spike detection in the ENG

5.3.2.1 Comparing the nature of overlapping spikes at mid-channel to those at offset

electrodes

The degree of overlap that can be tolerated before spikes become unrecognizable as

separate entities depends on the extent to which their positive and negative peaks interact

and interfere. Figure 5.7 simulates overlapping spike events and illustrates the kinds of

signals expected when spikes recorded for APs traveling in the same or opposite directions

overlap at mid-channel and offset electrodes.   For visualization purpose, overlap scenarios

are explored in (a)-(g) as a red spike is moved to the right, towards a fixed blue spike with

their algebraic sum, indicated in gray, representing the recorded signal.

Mid-channel spikes are identical regardless of AP direction and have prominent positive

and negative phases that significantly interfere, both constructively and destructively

(Figure 5.7 A). When their positive phases overlap constructively as in (b) and (f), their

negative phases remain distinct from each other and the spikes can still be recognized as

separate entities. When the positive phase of one spike overlaps the negative phase of

another as in (c) and (e) or when both negative phases overlap as in (d), the ability to

recognize spikes as distinct entities is compromised. Figure 5.7 B shows signals at an offset electrode for two action potentials traveling in the preferred direction. These are characterized by a single prominent negative phase flanked by two much smaller positive phases. Unlike mid-channel spikes, spikes are still recognizable as distinct entities even when the positive phase of one spike maximally overlaps the negative phase of another as in (c) and (e). Only when their negative phases overlap are spikes unrecognizable as distinct from one another as shown in (d).

Figure 5.7 C shows the overlap between signals at offset electrodes for APs traveling in the preferred (blue) and non-preferred (red) direction. The only scenario where the ability to detect the blue spike is compromised is in (e), where red's first very prominent positive phase cancels out blue's negative phase due to their similar amplitudes and duration.
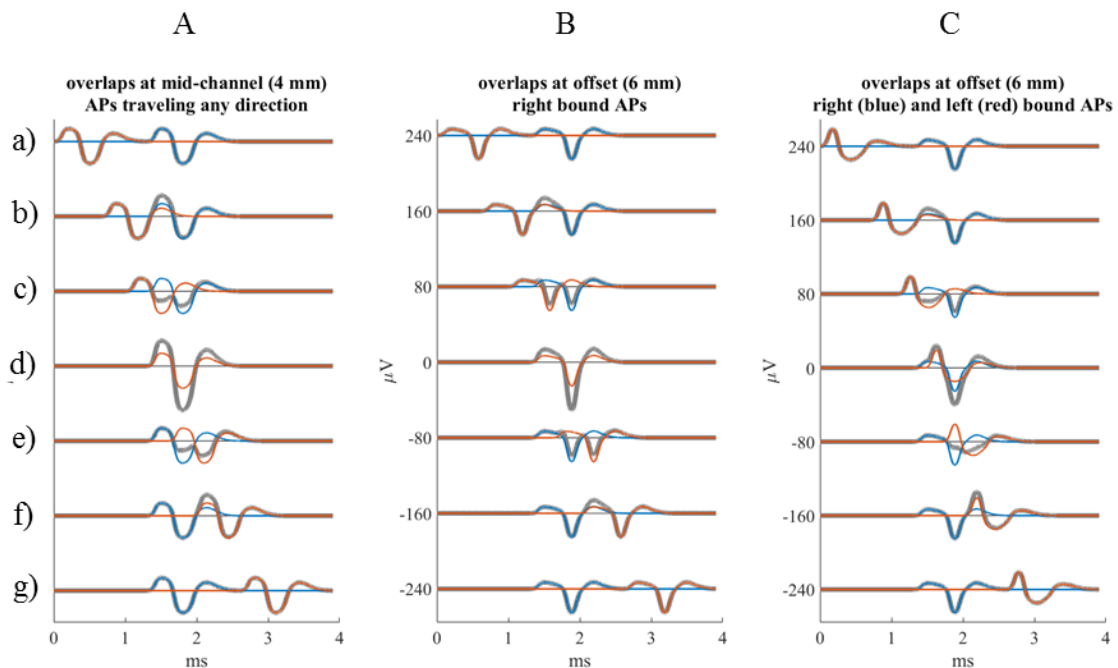
Figure 5.7 Simulated overlapping spike events at mid-channel and an offset electrode. Signals recorded A) at mid-channel for 15 m/s APs traveling left or right and those

traveling B) to the right or C) right (blue) and left (red) recorded at an offset electrode situated 6 mm from the left side of and 8 mm channel. (a)-(g) show the additive signal generated (thick gray line) when different combinations of the positive and negative phases of the blue and red signals superimpose constructively and destructively. Scenarios depicted are as follows: (a) red to the left of blue (no overlap), (b) constructive overlap between red's second and blue's first positive phase, (c) maximal destructive interference of red's second positive phase with blue's negative phase, (d) maximal constructive overlap, (e) maximal destructive interference of red's first positive phase with blue's negative phase, (f) maximal constructive overlap of red's first and blue's second positive phase, (g) red to the right of blue (no overlap).

For mid-channel recordings, only overlap between positive phases, representing about 1/3 of the total spike duration, can be tolerated. Thus, mid-channel spikes must be separated in time by no less than 2/3 their total duration for spikes to be detectable. Offset electrode recordings tolerate much more overlap without compromising the ability to discriminate between different spikes and spikes only have to be separated by about 1/3 their total duration to remain detectable as discrete events. Figure 5.8 shows the minimum temporal distances that spikes at mid-channel and offset electrodes must be seperated by in order for them to be resolvable as a function of AP speed. The durations permissible at offset electrodes are about 1/3 those at mid-channel.
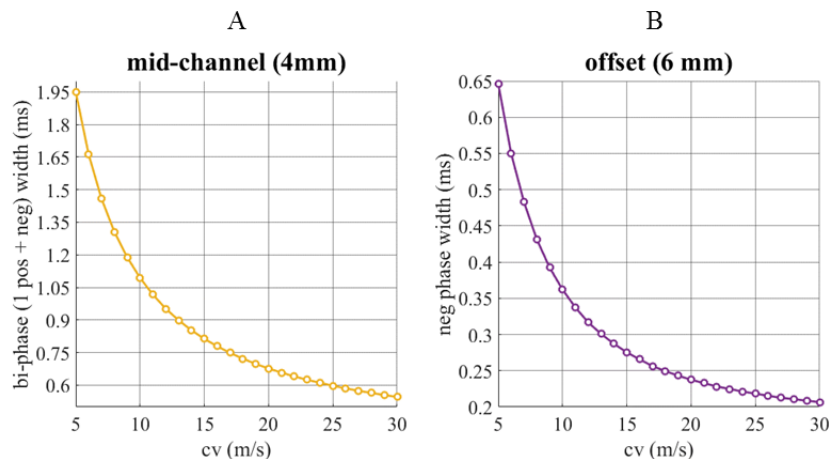
Figure 5.8 Durations of resolvable spikes at mid-channel and an offset electrode over a range of conduction velocities. Duration of the A) bi-phasic portion of the signal recorded at mid-channel verses the B) negative phase recorded at the 6 mm offset location.

5.3.2.2 Improved spike detection at offset electrodes

The discrete spike rate model described in Figure 5.2 was run using the permissible spike

durations provided in Figure 5.8 to simulate discrete spike frequencies at mid-channel and

an offset electrode (at 6 mm) for three speeds: 10, 15 and 25 m/s. The results are shown in

Figure 5.9. Mid-channel and offset electrodes perform equally well when total spike

frequencies are low, about less than 200 spikes per second. When spike rates exceed about

200 Hz, the offset electrode is significantly more capable of resolving individual spikes

compared to mid-channel recordings. For example, a nerve bundle containing 50 axons

firing at a mean rate of 50Hz represents a scenario involving 2000 spikes per second. As

Figure 5.9 B illustrates, for action potentials traveling at 15 m/s, the offset electrode would

be able to resolve about 9 times the number of spikes able to be detected at mid-channel

(630 compared to 70 discrete spikes per second). While the ratio is higher for slower action

potentials (10 m/s) and less for faster ones (25 m/s), the ability to detect discrete spike

events at offset electrodes is much higher than for mid-channel recordings.
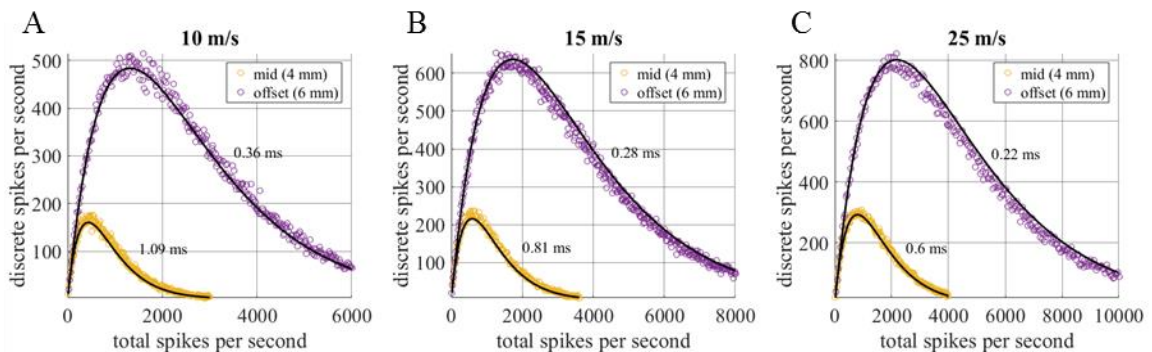
Figure 5.9 Frequency of resolvable spikes at mid-channel compared to an offset location. For APs traveling at A) 10, B) 15 and C) 25 m/s, the number of spikes able to be resolved at the offset electrode (purple circles) are substantially larger than at mid-channel (yellow circles). Spike durations are shown next to each data set and solid lines indicate model fits.

Assuming a density of 1 axon per 70 μm^2 for axons that have successfully regenerated through a microchannel array (FitzGerald et al., 2012), Figure 5.10 simulates the fraction of resolvable spikes at mid-channel and offset locations for microchannels having diameters of 100, 200 and 200 μm. Axonal firing rates were simulated to be 20 Hz and AP conduction velocities ranged between 5-30 m/s.
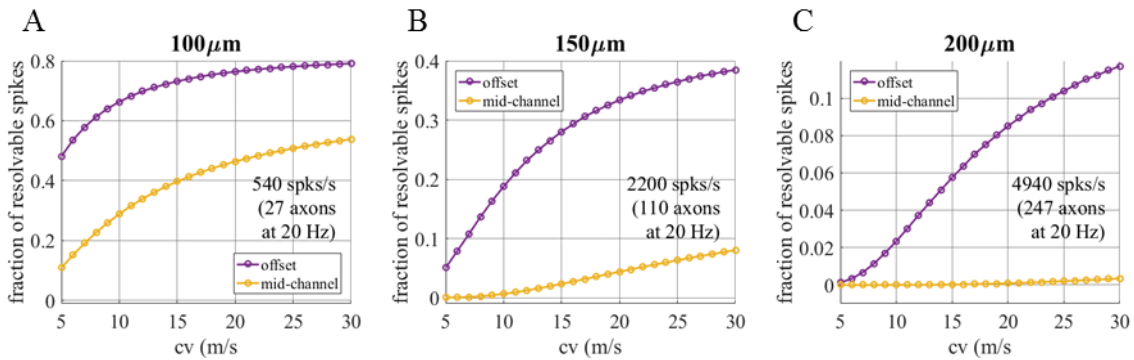
Figure 5.10 Fraction of resolvable spikes at mid-channel and an offset electrode for different sized channels. Channel inner diameters are A) 100, B) 150 and C) 200 µm. Mean axonal firing rates were simulated at 20 Hz.

For the range of channel sizes shown, offset electrodes are able to resolve a greater proportion of spikes compared to mid-channel recordings. Slower spikes have longer durations and are therefore less easily separable. Nevertheless, these slow signals would be detected in 100 μm diameter channels about 50% of the time at the offset electrode compared to only about 12% of the time at mid-channel (A). Mid-channel recordings are incapable of resolving these slow APs in channels 150 μm in diameter whereas offset electrode recordings would still be able to detect them a little over 5% of the time. For APs having speeds between 10-30 m/s, offset electrodes would detect discrete spikes between 20-40% of the time compared to mid-channel recordings where discrete spikes would be detectable at most 10% of the time. In 200 μm diameter channels, mid-channel

recordings cannot be used to detect individual spikes whereas at offset electrodes, action potentials having speeds in the range of 10-30 m/s range would be detected 2-12% of the time (C).

5.3.3 CAP simulations

5.3.3.1 Whole nerve CAPs: mid-channel vs. offset recordings

Whole nerve compound action potentials were constructed using the fiber histogram shown in Figure 5.11, reproduced from Waddell (Waddell et al., 1989). The majority of axons conduct in the 12-24 m/s velocity range, with those conducting at 15 m/s being the most numerous. A small cohort conduct at speeds less than 12 m/s. In this range, axons conducting at 5, 9 and 11 m/s are not well represented and their contribution to the CAP was anticipated to be relatively small and contributions from axons conducting at 6, 7, 8, 10 and 12 m/s were expected to dominate the response for the cohort of slower-conducting fibers.
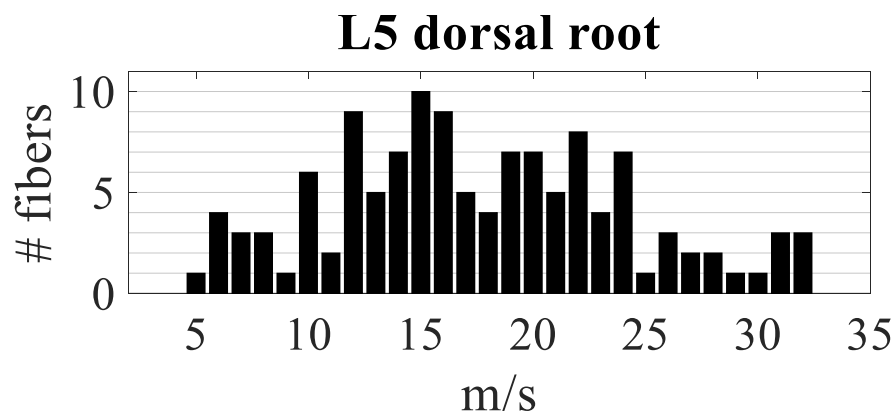
Figure 5.11 Fiber histogram of rat L5 dorsal root. Total number of fibers is 123. Data was reproduced from Waddell et. al. for rat dorsal roots.

Figure 5.11 compares simulated CAPs at mid-channel to those recorded by an offset electrode located 7 mm from the left end of the channel. In general, mid-channel CAPs are larger, especially when action potentials are initiated a distance of only 5 mm from the left edge of the channel. When the stimulus-to-channel distance is increased to 25 mm, CAP amplitudes are reduced and there is greater dispersion of APs traveling at different speeds. At mid-channel, located 29 mm from the stimulus site, peaks corresponding to fibers conducting at 6, 10 and 15 m/s can be identified as they correspond to the SUAP responses shown in gray. While peaks associated with fibers conducting at speeds between 6-10 m/s and 10-15 m/s are clearly visible in the SUAP traces, they are absent in the mid-channel CAP. At the offset electrode, located 32 mm from the stimulus site, an additional 4 peaks corresponding to fibers conducting at 5, 7, 8, and 12 m/s can be identified. The peaks associated with the fibers conducting at 9 and 11 m/s are absent in the offset CAP.
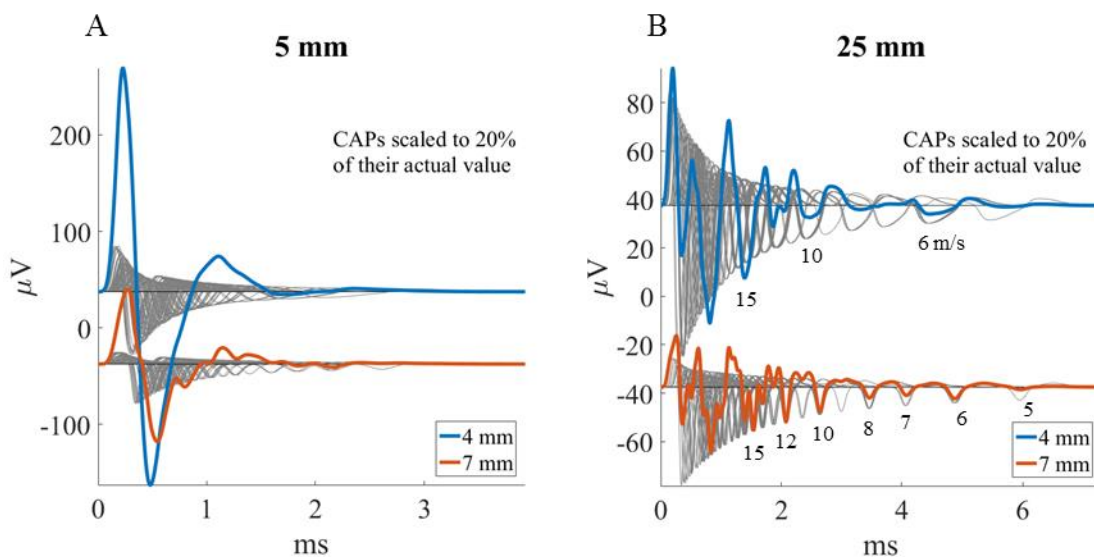
Figure 5.12 Simulated CAPs at different distances from site of stimulus. Stimulus sites are A) 5 mm and B) 25 mm from the channel entrance. Distinct peaks in B) are labeled with the conduction velocity of the fibers that produced them. Action potentials were

122

simulated as traveling to the right and CAPs were scaled by 20% to allow them to be visualized in relation to the signals from individual fibers (gray).

5.3.3.2 Teased rootlet CAPs: evidence of axonal damage

Figure 5.13 compares recorded and simulated CAPs in an intact and damaged rootlet model. The recorded CAPs were obtained from a rat L6 dorsal root using the methods described previously in Chapter 4. The rootlet was stimulated on the right side, nearest the 7 mm electrode, so signals propagate from bottom to top (A), electrode 5 (green) first and 1 (blue) last. The distribution of fibers used to simulate CAP responses are shown in (C) as this combination was found by trial and error to closely match the recorded signals (B). However, while we were able to match the shape and amplitudes of the electrodes first encountered by action potentials, the signals at mid-channel (yellow) and the offset electrodes at 2 (red) and 1 mm (blue) were larger than actually observed. Also, slight but noticeable negative deflections in the responses at 1 and 2 mm at t=1ms were absent in the simulated CAP shown in (D) and could not be reproduced. The best CAP match, shown in (B), was obtained when some of the fibers, namely those conducting at 17-20 m/s, were modeled as torn fragments that extend only partially through the channel (C). Using this damaged rootlet model, signal amplitudes and deflections in the recorded CAP were able to be simulated (B).
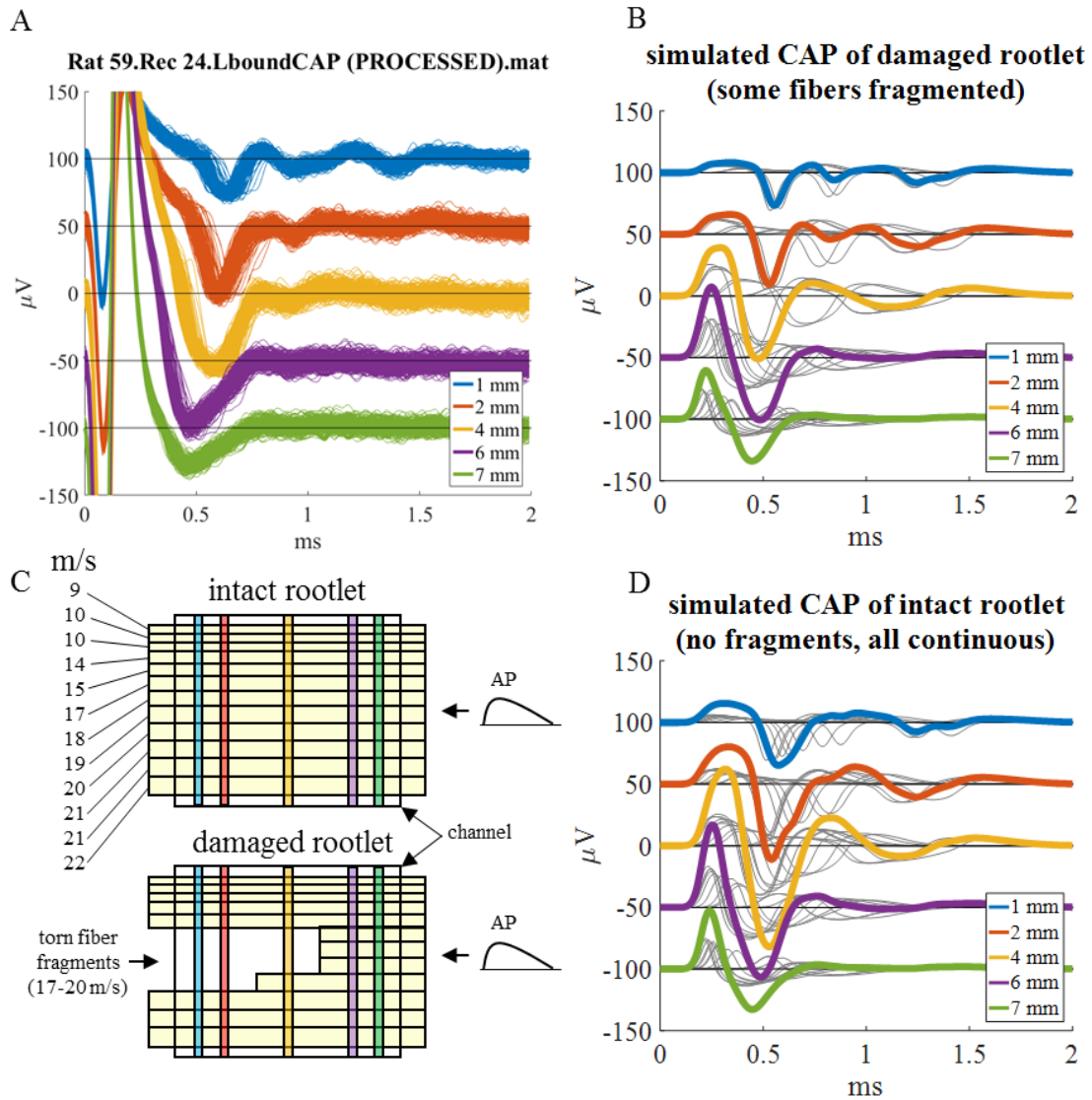
Figure 5.13 Recorded CAPs compared to those simulated using a damaged and intact rootlet model. Simulated CAPs scaled by 40%.

5.4 Discussion

5.4.1 Shape factors to enhance detection of SUAPs

The ability to detect activity in individual axons is a defining characteristic of microchannel devices for neural recording. This capability is extended when offset electrodes are employed since these record different signals for APs traveling in opposite direction. The

work presented here demonstrates that amplitude differences can be used as a first step in discriminating afferent from efferent neural activity by setting a threshold for detecting spikes, since action potentials traveling in preferred directions will have the largest amplitudes. However, as illustrated in Figure 5.3, background noise and differences in AP speeds can blur the amplitude distinctions and result in misclassification of action potential directionality.

Amplitude is only one quality that can be used to distinguish between signals associated with APs traveling in opposite directions, since there are significant differences in the shape of recorded signals that can be used to enhance signal discrimination. We develop two shape factors for scaling neural recordings at offset electrodes and show how these can be used to improve detection of action potentials traveling in a preferred direction. We also introduce the idea of combining shape factors to further accentuate differences. The ratio of the height to width factor, or hf/wf, was shown to result in significant enhancement of the signal of interest relative to those one wishes to ignore in both simulated and recorded signals. While only one iteration was used to scale signals using shape factors, in principle, there is no limit to how many times a given factor or hybrid or any permutation of these is used to scale signals. Technically, the scaling process could be repeated indefinitely to the point where only signals associated with APs traveling in the preferred direction would be detectable.

This could have implications for spike detection and classification schemes. Since the signal of interest would be detected more often after modification by shape factors, the load on spike classification algorithms running in real time is reduced, which could improve

their real-time performance. Also, a better signal-to-noise ratio (SNR) correlates to better success rates across the board for any spike classification scheme. When attempting to discriminate between APs traveling in opposite directions, the non-preferred direction represents a type of "noise" signal. Since shape factors differentially attenuate signals associated with APs traveling in the non-preferred direction, they would enhance the performance of any spike classification algorithm. This would include those that employ template matching (Lewicki, 1998) and matched filters (Roberts and Hartline, 1975) where success rates, the % of spikes classified correctly, highly correlate to SNR (Bankman et al., 1991, Gozani and Miller, 1994, Gribi et al., 2018).

5.4.2 Discrete spike detection in the ENG

In the peripheral nervous system, firing rate encodes for intensity. For example, firing rates increase in cutaneous afferents that convey pressure-related sensations when applied skin forces are large, and vice versa. In the motor domain, a motoneuron's firing rate determines the amount of force generated by its target muscle fibers, with low and high rates corresponding to small and large muscle forces. Accurate determination of firing rate hinges on the capacity to detect single unit spikes associated with one axon separately from other spikes, since overlapping spikes will either cancel each other out, and go undetected, or merge and be counted as a single spike. Either way, firing rates are underestimated or become impossible to assess when overlap rates approach and exceed neuronal firing rates. Over the years, spike classification algorithms have been developed to decompose overlapping spikes into their constituent components (Chandra and Optican, 1997, Franke et al., 2010, Roberts and Hartline, 1975, Gazzoni et al., 2004). However, even the most

trivial scenarios involving overlap between only two spikes produce complex time-varying signals that pose a significant challenge to classification and decomposition schemes (Lewicki, 1998). Furthermore, no algorithm can resurrect spikes that have canceled each other out.

Therefore, accurate assessment of neural activity is best achieved when overlap rates are small. The signals at offset electrodes for APs traveling in the preferred direction are characterized by a single prominent negative peak that has a much shorter duration than those recorded at mid-channel, where positive and negative phases are equally prominent. For offset electrode recordings, this prominent positive peak associated with APs traveling in the non-preferred direction only cancels the negative peak associated with those traveling in the preferred direction when these peaks overlap. Thus, spikes at offset electrodes are likely to be detected as long as they are spaced in time by at least one negative peak width apart. At mid-channel, however, recorded spikes must be spaced much further apart since there is much more opportunity for positive and negative phases of overlapping spikes to destructively interfere and cancel each other out. Since no spike detection algorithm can resurrect or recreate spikes that cancelled out and were, therefore, not detected, offset recordings would be expected to be superior to those at mid-channel for characterizing axonal firing rates.

5.4.3 CAP simulations

Compound action potentials represent a special unnatural class of ENG. They are synthetically produced by stimulating a nerve with currents sufficient to activate all fibers, both efferent and afferent, simultaneously. While CAPs do not occur physiologically, they

127

are a useful tool for studying nerves. They have been used to characterize the distribution of fiber sizes in many nerves (Gasser and Erlanger, 1927) and to document regeneration after nerve transection (Davis et al., 1978).

Here we show that CAPs constructed from mid-channel recordings differ from those at offset locations in significant ways. CAPs represent overlapping spikes. Since offset electrode waveforms have narrower negative peaks than those at mid-channel, which are broader, they overlap less frequently. Thus, there is a greater distribution of peaks in the CAPs recorded at offset electrodes compared to those recorded at mid-channel, where prominent positive phases in the SUAPs can cancel out adjacent negative peaks associated with fibers conducting at similar speeds. Thus, negative peaks associated with SUAPs traveling at different speeds are more frequent and distinct at offset electrodes than at mid-channel and their CAPs provide better opportunities than mid-channel CAPs for characterizing fiber size distributions in nerves.

5.4.4 Summary

In Chapter 4, a theoretical framework was developed and experimentally shown to be highly predictive of the neural signals one would expect to record in microchannels at offset electrodes. The analysis centered on a single feature of the recorded signal, namely, the negative peak amplitudes at offset electrodes and suggests they could be used to differentiate between SUAPs traveling in opposite directions. This chapter introduced shape factors as a quantitative approach for exploiting inherent shape differences in offset recordings to further enhance detection of SUAPs traveling in a preferred direction. Unlike negative peak amplitudes, shape factors are normalized indexes that remain reasonably

invariant over a wide range of conduction velocities and, therefore, provide a promising approach for differentiating between slow and fast SUAPs traveling in opposite directions.

This chapter also explored the capacity for offset electrodes to provide recording advantages in complex neural recording scenarios, such as the ENG and CAP, where detection of discrete SUAPs is not always guaranteed. Owing to their narrow and pronounced negative spike signatures, for any given ENG scenario, offset electrodes are predicted to record a much higher percentage of discrete spike events than are mid-channel electrodes. One important implication is, compared to mid-channel configurations, offset electrodes could be employed in larger diameter channels containing many more axons without compromising their detection rates. This represents a significant improvement over mid-channel recording configurations, especially when coupled with the offset's inherent ability to provide information about the signal's directionality. For CAP recordings, the offset advantage lies in an enhanced ability to visualize a greater number of peaks in the CAP associated with different fiber types than can be visualized in the larger CAP recorded at mid-channel. Overall, the offset electrode recordings can be used to differentiate between SUAPs traveling in opposite directions and are theoretically capable of detecting a greater proportion of discrete SUAPs than their mid-channel counterparts in more complex neural recording scenarios.

CHAPTER 6

CONCLUSIONS

6.1 Context

Microchannels are unique in their ability to chronically record signals in individual axons. They were originally conceived and later successfully implemented as the basic building block for regenerative electrode (RE) arrays designed to record bi-directional neural activity in regenerated axons. Therefore, it would seem improbable to employ electrode configurations that would prevent microchannel technologies from being able to determine the directionality of recorded signals. Not only would this compromise their intended use, it would also represent a tremendous loss of useful neural information, since action potential directionality orchestrates behavior and function at the granular level. Nevertheless, all RE arrays developed to date employ mid-channel recording sites incapable of being able to discriminate afferent from efferent neural activity.

Given the significant cost to microchannel capabilities, it is surprising to learn that the rationale for the use of mid-channel electrodes is rarely discussed by those who research and develop microchannel technologies. One learns from the literature that the mid-channel electrode is integral to the pseudo tripole configuration for preventing unwanted noise artifacts, such as EMG signals, from overwhelming and obscuring recorded neural activity. While noise rejection is an important consideration, other methods to achieve this without necessitating a central recording site in microchannels could have been explored. Over a decade ago, it was noted that non-central recording sites might be able to record larger signals than those at mid-channel. However, no mechanism for this effect was

proposed that could guide development along these lines. Perhaps this partly explains why efforts to explore alternative electrode configurations have not been undertaken.

In summary, microchannel development has stagnated around a universally-accepted mid-channel electrode configuration steeped in tradition that prevents their full potential as highly selective neural recording devices from being realized. The offset electrode approach challenges these conventions, frees microchannel design from the limitations associated with the pseudo tripole and presents a viable alternative pathway for neural recording in general.

6.2 Significance

This work introduces offset electrodes as a new paradigm for recording signals in peripheral nerves. We show that a single offset recording site can be used to determine the directionality of recorded signals. Until now, this has required a minimum of two recording sites positioned at different locations on the nerve.

A theoretical basis to explain the origin for signal enhancement at offset electrodes is presented and used to design microchannels containing offset electrodes optimally positioned to maximize difference for signals traveling in opposite directions (Chapter 3). We incorporate the theory into a comprehensive mathematical framework for predicting neural and noise signals in microchannels and demonstrate its capacity to accurately predict recorded signals (Chapter 4).

To our knowledge, the linearity of external noise artifacts inside microchannels has not been experimentally validated. We demonstrate the linearity of external noise artifacts and

show it agrees with the theoretical predictions. This linearity is exploited to develop viable references for canceling out external noise artifacts at offset as well as at mid-channel locations (Chapter 4). We propose two approaches, "weighted" and "parallel" references, and demonstrate their potential to serve as viable candidate reference terminals for effectively canceling noise artifacts at offset recording sites, as well as at mid-channel. Background noise levels are quantified and shown to be mainly of a thermal nature as suggested by their being consistent with a Johnson noise model.

Finally, we introduce novel methods to characterize shape differences in offset electrode recordings and demonstrate their ability to enhance differences between signals recorded for action potentials traveling in preferred and non-preferred directions (Chapter 5). These shape differences are also shown to improve the detection of discrete spike events in more complex neural signals involving overlapping spikes. The implications of shape differences on the compound action potentials are explored.

6.3 Limitations

While this work demonstrates the superiority of offset recording sites over traditional mid-channel locations, the findings are based on an *in vitro* experimental paradigm where neural and noise signals are explored in a controlled environment. The extent to which the results translate to real-life recording scenarios in behaving animals remains to be determined. For example, the development of future regeneration electrode arrays is maintained throughout this work as a desirable target application for offset electrodes. We make this claim based on neural recordings performed using a microchannel having a length of 8 mm. The longest chronic regeneration electrode arrays developed to date have used

channels only 4 mm in length (Musick et al., 2015), with 5 mm being the longest channel length where evidence of successful axonal regeneration through an REA has been experimentally demonstrated (Lacour et al., 2009). While offset electrodes would still be expected to provide a basis for SUAP discrimination in 4-5 mm long channels, the range of AP speeds over which these shorter channel lengths would be expected to optimally perform would be slower than those we recorded using an 8 mm long channel. Also, channels having smaller cross sections than the 200 μm ID channels used here might need to be considered in order for these slower APs to be reliably detected above background noise levels.

In preliminary experiments, we demonstrated a limited capacity to record SUAPs *in vivo* in anesthetized rats using 300 μm ID x 10 mm long microchannels. However, background noise levels were considerably higher than we observed in our *in vitro* preparation and occasionally heart-beat and electrical artifacts associated with respiration could not successfully be eliminated from the recorded signals. The extent to which weighted or parallel references could be used to cancel out these real-world noise artifacts remains to be determined. Neither reference configuration had been developed at the time the *in vivo* trails were conducted. The performance of the weighted reference approach could still be evaluated using these preliminary data since it involves mathematically constructed signals using a linear interpolation of the signals recorded at the outermost pair of offset electrodes, which exists for these data sets. Performance of the parallel reference configuration is not possible since it would have required a device having an aligned set of reference electrodes in a parallel empty channel separate from the one containing the neural tissue.

The performance of the parallel reference configuration during actual neural recording experiments was not done and represents a limitation that remains to be addressed. Here, the parallel reference was demonstrated using aligned references in two empty parallel channels, neither of which contained a nerve. In reality, one of the channels would be filled with neural tissue which would be expected to alter the conductivity profile in that channel compared to the empty one. The extent to which external noise signals recorded in a nerve-filled channel are similar to or different from those recorded in an empty parallel channel remains to be explored.

6.4 Future directions

The offset electrode paradigm is practical, flexible and adaptable and can be readily incorporated into existing technologies as well as providing motivation for the development of new ones. For example, our "weighted reference" approach described in Chapter 4 uses a similar electrode arrangement as the one used by the traditional pseudo tripole. Any of the current technologies where pseudo tripole configurations are employed could easily be reconfigured with offset electrodes having equivalent noise rejection capabilities. Future generations of RE arrays containing offset electrodes in different locations in each channel would enable them to realize their full potential as highly selective chronic neural recording devices able to distinguish efferent from afferent signals. The "parallel reference" described in Chapter 4 would provide an ideal configuration for rejecting external noise artifacts in RE arrays containing offset electrodes.

6.5 Final remarks

Overall, this work challenges accepted practices that have and continue to limit microchannel capabilities and provides alternative pathways for enhancing their performance. Our hope is for others to use this as a foundation to improve existing microchannel technologies and motivate the development of future devices with enhanced recording capabilities.

REFERENCES

BANKMAN, I. N., JOHNSON, K. O. & SCHNEIDER, W. Optimal recognition of neural waveforms. Proceedings of the 13th Annual International Conference of the IEEE Engineering in Medicine and Biology Society, 1991. Publ by IEEE, 409-410.

BOYD, I. & KALU, K. 1979. Scaling factor relating conduction velocity and diameter for myelinated afferent nerve fibres in the cat hind limb. *The Journal of physiology,* 289**,** 277-297.

BRADLEY, R. M., SMOKE, R. H., AKIN, T. & NAJAFI, K. 1992. Functional regeneration of glossopharyngeal nerve through micromachined sieve electrode arrays. *Brain research,* 594**,** 84-90.

CHANDRA, R. & OPTICAN, L. M. 1997. Detection, classification, and superposition resolution of action potentials in multiunit single-channel recordings by an on-line real-time neural network. *IEEE Transactions on Biomedical Engineering,* 44**,** 403-412.

CHEW, D. J., ZHU, L., DELIVOPOULOS, E., MINEV, I. R., MUSICK, K. M., MOSSE, C. A., CRAGGS, M., DONALDSON, N., LACOUR, S. P., MCMAHON, S. B. & FAWCETT, J. W. 2013. A microchannel neuroprosthesis for bladder control after spinal cord injury in rat. *Sci Transl Med,* 5**,** 210ra155.

DAVIS, L., GORDON, T., HOFFER, J.-A., JHAMANDAS, J. & STEIN, R. B. 1978. Compound action potentials recorded from mammalian peripheral nerves following ligation or resuturing. *The Journal of physiology,* 285**,** 543-559.

DELIVOPOULOS, E., CHEW, D. J., MINEV, I. R., FAWCETT, J. W. & LACOUR, S. P. 2012. Concurrent recordings of bladder afferents from multiple nerves using a microfabricated PDMS microchannel electrode array. *Lab on a chip,* 12**,** 2540-2551.

DWORAK, B. J. & WHEELER, B. C. 2009. Novel MEA platform with PDMS microtunnels enables the detection of action potential propagation from isolated axons in culture. *Lab on a Chip,* 9**,** 404-410.

EDELL, D. J. 1986. A peripheral nerve information transducer for amputees: long-term multichannel recordings from rabbit peripheral nerves. *IEEE Transactions on Biomedical Engineering***,** 203-214.

FITZGERALD, J. J., LACOUR, S. P., MCMAHON, S. B. & FAWCETT, J. W. 2008. Microchannels as axonal amplifiers. *Ieee Transactions on Biomedical Engineering,* 55**,** 1136-1146.

FITZGERALD, J. J., LACOUR, S. P., MCMAHON, S. B. & FAWCETT, J. W. 2009. Microchannel electrodes for recording and stimulation: in vitro evaluation. *IEEE Transactions on Biomedical Engineering,* 56**,** 1524-1534.

FITZGERALD, J. J., LAGO, N., BENMERAH, S., SERRA, J., WATLING, C. P., CAMERON, R. E., TARTE, E., LACOUR, S. P., MCMAHON, S. B. &

FAWCETT, J. W. 2012. A regenerative microchannel neural interface for recording from and stimulating peripheral axons in vivo. *J Neural Eng,* 9**,** 016010.

FRANKE, F., NATORA, M., BOUCSEIN, C., MUNK, M. H. J. & OBERMAYER, K. 2010. An online spike detection and spike classification algorithm capable of instantaneous resolution of overlapping spikes. *J Comput Neurosci,* 29**,** 127-148.

GASSER, H. S. & ERLANGER, J. 1927. The role played by the sizes of the constituent fibers of a nerve trunk in determining the form of its action potential wave. *American Journal of Physiology-Legacy Content,* 80**,** 522-547.

GAZZONI, M., FARINA, D. & MERLETTI, R. 2004. A new method for the extraction and classification of single motor unit action potentials from surface EMG signals. *Journal of Neuroscience Methods,* 136**,** 165-177.

GOZANI, S. N. & MILLER, J. P. 1994. Optimal discrimination and classification of neuronal action potential waveforms from multiunit, multichannel recordings using software-based linear filters. *IEEE Transactions on Biomedical Engineering,* 41**,** 358-372.

GRIBI, S., DE DUNILAC, S. D. B., GHEZZI, D. & LACOUR, S. P. 2018. A microfabricated nerve-on-a-chip platform for rapid assessment of neural conduction in explanted peripheral nerve fibers. *Nature Communications,* 9**,** 4403.

HAUGLAND, M. K. & SINKJAER, T. 1995. Cutaneous whole nerve recordings used for correction of footdrop in hemiplegic man. *IEEE Transactions on rehabilitation Engineering,* 3**,** 307-317.

HEETDERKS, W. & WILLIAMS, W. 1975. Partition of gross peripheral nerve activity into single unit responses by correlation techniques. *Science,* 188**,** 373-375.

HODGKIN, A. L. & RUSHTON, W. A. H. 1946. The electrical constants of a crustacean nerve fibre. *Proceedings of the Royal Society of London. Series B-Biological Sciences,* 133**,** 444-479.

HOFFER, J. & LOEB, G. 1980. Implantable electrical and mechanical interfaces with nerve and muscle. *Annals of biomedical engineering,* 8**,** 351-360.

HOFFER, J. A., STEIN, R. B., HAUGLAND, M. K., SINKJAER, T., DURFEE, W. K., SCHWARTZ, A. B., LOEB, G. E. & KANTOR, C. 1996. Neural signals for command control and feedback in functional neuromuscular stimulation: a review. *J Rehabil Res Dev,* 33**,** 145-157.

HORCH, K., MEEK, S., TAYLOR, T. G. & HUTCHINSON, D. T. 2011. Object discrimination with an artificial hand using electrical stimulation of peripheral tactile and proprioceptive pathways with intrafascicular electrodes. *IEEE Transactions on Neural Systems and Rehabilitation Engineering,* 19**,** 483-489.

HURSH, J. 1939. Conduction velocity and diameter of nerve fibers. *American Journal of Physiology-Legacy Content,* 127**,** 131-139.

KOVACS, G. T., STORMENT, C. W. & ROSEN, J. M. 1992. Regeneration microelectrode array for peripheral nerve recording and stimulation. *IEEE Transactions on Biomedical Engineering,* 39**,** 893-902.

LACOUR, S. P., FITZGERALD, J. J., LAGO, N., TARTE, E., MCMAHON, S. & FAWCETT, J. 2009. Long micro-channel electrode arrays: a novel type of regenerative peripheral nerve interface. *IEEE transactions on neural systems and rehabilitation engineering,* 17**,** 454-460.

LAGO, N., CEBALLOS, D., RODRíGUEZ, F. J., STIEGLITZ, T. & NAVARRO, X. 2005. Long term assessment of axonal regeneration through polyimide regenerative electrodes to interface the peripheral nerve. *Biomaterials,* 26**,** 2021-2031.

LAGO, N., UDINA, E., RAMACHANDRAN, A. & NAVARRO, X. 2007. Neurobiological assessment of regenerative electrodes for bidirectional interfacing injured peripheral nerves. *IEEE transactions on biomedical engineering,* 54**,** 1129-1137.

LASH, J. P. & BYERS, C. 1980. *Helen and teacher: the story of Helen Keller and Anne Sullivan Macy*, Delacorte Press New York.

LEWICKI, M. S. 1998. A review of methods for spike sorting: the detection and classification of neural action potentials. *Network: Computation in Neural Systems,* 9**,** R53-R78.

LOEB, G., MARKS, W. & BEATTY, P. 1977. Analysis and microelectronic design of tubular electrode arrays intended for chronic, multiple singleunit recording from captured nerve fibres. *Medical and Biological Engineering and Computing,* 15**,** 195-201.

MANNARD, A., STEIN, R. B. & CHARLES, D. 1974. Regeneration electrode units: implants for recording from single peripheral nerve fibers in freely moving animals. *Science,* 183**,** 547-549.

MARKS, W. B. & LOEB, G. E. 1976. Action currents, internodal potentials, and extracellular records of myelinated mammalian nerve fibers derived from node potentials. *Biophys J,* 16**,** 655-68.

MEIER, J. H., RUTTEN, W. L. & BOOM, H. B. 1998a. Extracellular potentials from active myelinated fibers inside insulated and noninsulated peripheral nerve. *IEEE transactions on biomedical engineering,* 45**,** 1146-1153.

MEIER, J. H., RUTTEN, W. L. & BOOM, H. B. 1998b. Extracellular potentials from active myelinated fibers inside insulated and noninsulated peripheral nerve. *IEEE Trans Biomed Eng,* 45**,** 1146-53.

MICERA, S., CITI, L., RIGOSA, J., CARPANETO, J., RASPOPOVIC, S., DI PINO, G., ROSSINI, L., YOSHIDA, K., DENARO, L. & DARIO, P. 2010. Decoding information from neural signals recorded using intraneural electrodes: toward the development of a neurocontrolled hand prosthesis. *Proceedings of the IEEE,* 98**,** 407-417.

MINEV, I. R., CHEW, D. J., DELIVOPOULOS, E., FAWCETT, J. W. & LACOUR, S. P. 2012. High sensitivity recording of afferent nerve activity using ultra-compliant microchannel electrodes: an acute in vivo validation. *Journal of Neural Engineering,* 9**,** 026005.

MUSICK, K. M., RIGOSA, J., NARASIMHAN, S., WURTH, S., CAPOGROSSO, M., CHEW, D. J., FAWCETT, J. W., MICERA, S. & LACOUR, S. P. 2015. Chronic multichannel neural recordings from soft regenerative microchannel electrodes during gait. *Scientific reports,* 5**,** 14363.

NAVARRO, X., KRUEGER, T. B., LAGO, N., MICERA, S., STIEGLITZ, T. & DARIO, P. 2005. A critical review of interfaces with the peripheral nervous system for the control of neuroprostheses and hybrid bionic systems. *Journal of the Peripheral Nervous System,* 10**,** 229-258.

PAINTAL, A. 1967. A comparison of the nerve impulses of mammalian non-medullated nerve fibres with those of the smallest diameter medullated fibres. *The Journal of physiology,* 193**,** 523-533.

PAINTAL, A. S. 1966. The influence of diameter of medullated nerve fibres of cats on the rising and falling phases of the spike and its recovery. *J Physiol,* 184**,** 791-811.

PLONSEY, R. & BARR, R. C. 2007. *Bioelectricity: a quantitative approach*, Springer Science & Business Media.

POPOVIC, D. B., STEIN, R. B., JOVANOVIC, K. L., DAI, R., KOSTOV, A. & ARMSTRONG, W. W. 1993. Sensory nerve recording for closed-loop control to restore motor functions. *IEEE Trans Biomed Eng,* 40**,** 1024-31.

RAMACHANDRAN, A., SCHUETTLER, M., LAGO, N., DOERGE, T., KOCH, K. P., NAVARRO, X., HOFFMANN, K.-P. & STIEGLITZ, T. 2006. Design, in vitro and in vivo assessment of a multi-channel sieve electrode with integrated multiplexer. *Journal of neural engineering,* 3**,** 114.

RITCHIE, J. M. 1982. On the relation between fibre diameter and conduction velocity in myelinated nerve fibres. *Proceedings of the Royal Society of London. Series B. Biological Sciences,* 217**,** 29-35.

ROBERTS, W. M. & HARTLINE, D. K. 1975. Separation of multi-unit nerve impulse trains by a multi-channel linear filter algorithm. *Brain research,* 94**,** 141-149.

ROSEN, J. M., GROSSER, M. & HENTZ, V. R. 1990. Preliminary experiments in nerve regeneration through laser-drilled holes in silicon chips. *Restorative neurology and neuroscience,* 2**,** 89-102.

SABETIAN, P., POPOVIC, M. R. & YOO, P. B. 2017. Optimizing the design of bipolar nerve cuff electrodes for improved recording of peripheral nerve activity. *Journal of neural engineering,* 14**,** 036015.

SCHUETTLER, M., DONALDSON, N., SEETOHUL, V. & TAYLOR, J. 2013. Fibre-selective recording from the peripheral nerves of frogs using a multi-electrode cuff. *Journal of neural engineering,* 10**,** 036016.

SINKJAER, T. 2000. Integrating sensory nerve signals into neural prosthesis devices. *Neuromodulation,* 3**,** 35-41.

SRINIVASAN, A., TAHILRAMANI, M., BENTLEY, J. T., GORE, R. K., MILLARD, D. C., MUKHATYAR, V. J., JOSEPH, A., HAQUE, A. S., STANLEY, G. B. & ENGLISH, A. W. 2015. Microchannel-based regenerative scaffold for chronic peripheral nerve interfacing in amputees. *Biomaterials,* 41**,** 151-165.

STEIN, R., GORDON, T., HOFFER, J., DAVIS, L. & CHARLES, D. 1980a. Long-term recordings from cat peripheral nerves during degeneration and regeneration: implications for human nerve repair and prosthetics. *Nerve Repair: Its Clinical and Experimental Basis***,** 166-176.

STEIN, R. B., CHARLES, D., DAVIS, L., JHAMANDAS, J., MANNARD, A. & NICHOLS, T. R. 1975. Principles underlying new methods for chronic neural recording. *Can J Neurol Sci,* 2**,** 235-44.

STEIN, R. B., CHARLES, D., HOFFER, J., ARSENAULT, J., DAVIS, L., MOORMAN, S. & MOSS, B. 1980b. New approaches for the control of powered prostheses particularly by high-level amputees. *Bull Prosthet Res,* 10**,** 51-62.

STEIN, R. B., NICHOLS, T. R., JHAMANDAS, J., DAVIS, L. & CHARLES, D. 1977. Stable long-term recordings from cat peripheral nerves. *Brain Res,* 128**,** 21-38.

STEIN, R. B. & PEARSON, K. G. 1971. Predicted amplitude and form of action potentials recorded from unmyelinated nerve fibres. *J Theor Biol,* 32**,** 539-58.

STRUIJK, J. J. 1997. The extracellular potential of a myelinated nerve fiber in an unbounded medium and in nerve cuff models. *Biophys J,* 72**,** 2457-69.

STRUIJK, J. J., THOMSEN, M., LARSEN, J. O. & SINKJAER, T. 1999. Cuff electrodes for long-term recording of natural sensory information. *IEEE Eng Med Biol Mag,* 18**,** 91-8.

SUNDERLAND, S. & BRADLEY, K. 1961. Stress-strain phenomena in human spinal nerve roots. *Brain,* 84**,** 120-124.

TAN, D. W., SCHIEFER, M. A., KEITH, M. W., ANDERSON, J. R., TYLER, J. & TYLER, D. J. 2014. A neural interface provides long-term stable natural touch perception. *Science translational medicine,* 6**,** 257ra138-257ra138.

TAYLOR, J., DONALDSON, N. & WINTER, J. 2004. Multiple-electrode nerve cuffs for low-velocity and velocity-selective neural recording. *Medical and Biological Engineering and Computing,* 42**,** 634-643.

THOMSEN, M., STRUIJK, J. & SINKJÆR, T. Artifact reduction with monopolar nerve cuff recording electrodes. Proceedings of 18th Annual International Conference of the IEEE Engineering in Medicine and Biology Society, 1996. IEEE, 367-368.

WADDELL, P., LAWSON, S. & MCCARTHY, P. 1989. Conduction velocity changes along the processes of rat primary sensory neurons. *Neuroscience,* 30**,** 577-584.

YOSHIDA, K., KURSTJENS, G. & HENNINGS, K. 2009. Experimental validation of the nerve conduction velocity selective recording technique using a multi-contact cuff electrode. *Medical engineering & physics,* 31**,** 1261-1270.

VITA

IIAN BLACK

Born, Sarasota, Florida

1989-1999	Builder R.G. Black Construction El Cerrito, CA
1991-1996	B.S. Bioengineering University of California at Berkeley Berkeley, CA
1999-2000	Technical writer PlanetRx.com South San Francisco, CA
2001-2002	Math Teacher John Swett High School Crocket, CA
2002-2004	M.S. Bioengineering (summa cum laude) The Catholic University of America Washington, DC
2003-2004	Teaching Assistant The Catholic University of America Washington, DC
2004-2010	Design Engineer Aretech, LLC Washington, DC
2006-2010	Project Coordinator Assistive Technology Research Center (ATRC) Washington, DC
2010-2013	Senior Research Scientist Center for Applied Biomechanics Research and Rehabilitation Washington, DC
2013-2019	Doctoral Candidate Florida International University Miami, FL

2015-2017   Teaching Assistant
Florida International University
Miami, FL

PUBLICATIONS AND PRESENTATIONS

Black i, Nichols D, Pelliccio M, Hidler JM, (2007) Quantification of reflex activity in stroke survivors during an imposed multi-joint leg extension movement, *Experimental Brain Research*, 183(2):271-81.

Nef T, Brennan D, Black i, Hidler JM, Patient-tracking for an over-ground gait training system, *IEEE 11th International Conference on Rehabilitation Robotics (ICORR)*, Kyoto, Japan, June 23-26, 2009.

Brokaw EB, Black i, Holley RJ, Lum PS, Hand Spring Operated Movement Enhancer (HandSOME): a portable hand exoskeleton for stroke rehabilitation, *IEEE Transactions on Neural Systems and Rehabilitation Engineerin*g, 2011 Aug; 19(4): 391-9.

Hidler J, Brennan D, Black i, Nichols D, Brady K, Nef T, ZeroG: overground gait and balance training system, *Journal of Rehabilitation Research and Development*, 2011, 48(4): 287-98.

Black i, Abbas J, Jung R. Predicted Effect of Electrode Position on the Amplitude of Recorded Neural Signals Using Cuff-like Technologies. *NANS2-Neural Interfaces Joint Meeting*, Baltimore, MD, Jun 25-29, 2016, Poster presentation #73.

Black i, Abbas J, Thota A, Jung R. Development of a rootlet interface to localize cutaneous stimuli applied to specific regions of the rat hindlimb. *University of Miami Neural Engineering Research Symposium*, Miami, FL, Oct 13th, 2016, Poster presentation #14.

Black i, Jung R. Recording from individual axons in teased spinal cord rootlets. *University of Miami Neural Engineering Research Symposium*, Miami, FL, April 2nd, 2017, Poster presentation #11. (1st place at the BME Graduate Student Research Day at FIU)

Caduff D, Black i, Jung R. Detecting the Presence of Sensory Stimuli in Neural Recordings, *Conference for Undergraduate Research at Florida International University (CURFIU)*, Miami, FL, March 27th, 2018, Poster presentation.

Black i, Abbas JJ, Jung R, (2017). Off-center electrodes provide signal enhancement and improved selectivity of cuff-like technologies for neural recording, *Journal of Neural Engineering, JNE-102089* (pending re-submission)

Black i, Jung R. (2019). Flanged self-closing microchannel array. *United States patent US 10,186,207*